ARTICLES
https://doi.org/10.1038/s41556-022-00844-9

nature cell biology

Rear traction forces drive adherent tissue migration in vivo

Naoya Yamaguchi[1], Ziyi Zhang[2], Teseo Schneider[2,3], Biran Wang[4], Daniele Panozzo[2]✉ and Holger Knaut[1]✉

During animal embryogenesis, homeostasis and disease, tissues push and pull on their surroundings to move forward. Although the force-generating machinery is known, it is unknown how tissues exert physical stresses on their substrate to generate motion in vivo. Here, we identify the force transmission machinery, the substrate and the stresses that a tissue, the zebrafish posterior lateral line primordium, generates during its migration. We find that the primordium couples actin flow through integrins to the basement membrane for forward movement. Talin- and integrin-mediated coupling is required for efficient migration, and its loss is partially compensated for by increased actin flow. Using Embryogram, an approach to measure stresses in vivo, we show that the rear of the primordium exerts higher stresses than the front, which suggests that this tissue pushes itself forward with its back. This unexpected strategy probably also underlies the motion of other tissues in animals.

During development, homeostasis and disease, cells and tissues move to form organs, to seal wounds and to hunt pathogens[1]. To move, cells generate force and interact with their surroundings to pull and push themselves forward. Force transmission from the actomyosin network to the surroundings has been molecularly characterized and precisely measured in cultured cells[2,3]. Cells use integrin-based adhesion complexes to couple the actomyosin network inside the cells to the substrates outside the cells and pull on their surroundings with forces of around 3–30 pN across molecules[4]. Since many processes are altered when cells are removed from their physiological environment and placed in culture, it is largely unclear whether cells in living animals interact with their surrounding in the same manner and pull on their substrate with similar forces. To address these questions, we use the zebrafish posterior lateral line primordium as a model. The primordium is a tissue of about 140 cells that expresses the chemokine receptor Cxcr4b. It migrates directly under the skin from behind the ear to the tip of the tail and follows a gradient of the chemokine Cxcl12a along the body of the embryo[5].

Results

The primordium migrates on a basement membrane. To learn about the substrate that the primordium uses to push and pull itself forward, we used transmission electron microscopy (TEM) to inspect transverse sections of embryos (30 h post fertilization (h.p.f.)) at different locations along the migratory route of the primordium. Consistent with previous studies[6,7], we found that the two-layered skin is separated from the underlying muscle by a 200-nm thick basement membrane (BM) in front of the migrating primordium (Extended Data Fig. 1a,e). At the position of the primordium, the migrating tissue separates the skin and the BM, such that the basal side of the primordium is juxtaposed to the BM while there is no BM detectable on its apical side (Fig. 1a and Extended Data Fig. 1b–e). We confirmed these observations by inspecting the localization of the core BM component laminin-γ1 tagged with superfolder green fluorescent protein (LamC1–sfGFP) (Extended Data Fig. 1f,g). During its migration, the primordium wedges itself between the skin and the muscle, and pushes the LamC1–sfGFP-labelled BM towards its basal side with little to no LamC1–sfGFP detectable between the primordium and the skin (Extended Data Fig. 1j). This separates the BM from the skin (Fig. 1b). Consistent with this, we found that the basal side of the skin labelled with fluorescently tagged E-cadherin abuts the apical side of the primordium (Fig. 1c). Thus, the primordium migrates on top of the BM and underneath the skin (Fig. 1d).

The primordium requires the BM for migration. If the skin and the BM serve as substrates for the primordium, they should also be required for the migration of the primordium. Indeed, surgical removal of the skin blocks primordium migration[8]. To assess the role of the skin in primordium migration in a less invasive manner, we depleted α-catenin tagged with Citrine (Ctnna1–Citrine) in the primordium using the degron system zGrad[9] expressed from the *cxcr4b* promoter in the migrating primordium (Extended Data Fig. 2a–d). Ctnna1 links cadherin to the actin cytoskeleton[10] and its depletion should abrogate cadherin-mediated cell–cell adhesion between the skin and the primordium. As previously reported[11], depletion of Ctnna1–Citrine in the primordium affects sensory organ deposition and directionality of the cells in the primordium (Fig. 2a,b and Supplementary Video 1). However, we found that this does not affect the speed of the cells (Fig. 2c).

To assess the role of the BM in primordium migration, we analysed the migration of the primordium in *lamC1* mutant embryos. In such embryos, the BM is disrupted or missing[7], and inspection of the collagen IV network and the BM confirmed this observation (Fig. 2d,e). Since the lack of LamC1 also impairs the formation of the Cxcl12a-secreting stripe of cells that guides the primordium (Extended Data Fig. 2e), we assessed the ability of the primordium to migrate in *lamC1* mutant embryos by generating an ectopic Cxcl12a source in the trunk muscles. The initial location of the primordium is not affected in *lamC1* mutant embryos (Extended Data Fig. 2f,g). For this analysis, we also removed endogenous Cxcl12a to avoid competition between endogenous and ectopic chemokine

[1]Skirball Institute of Biomolecular Medicine, New York University Grossman School of Medicine, New York, NY, USA. [2]Courant Institute of Mathematical Sciences, New York University, New York, NY, USA. [3]Computer Science, University of Victoria, Victoria, British Columbia, Canada. [4]Molecular Cytology Core Facility, Memorial Sloan Kettering Cancer Center, New York, NY, USA. ✉e-mail: panozzo@nyu.edu; holger.knaut@med.nyu.edu

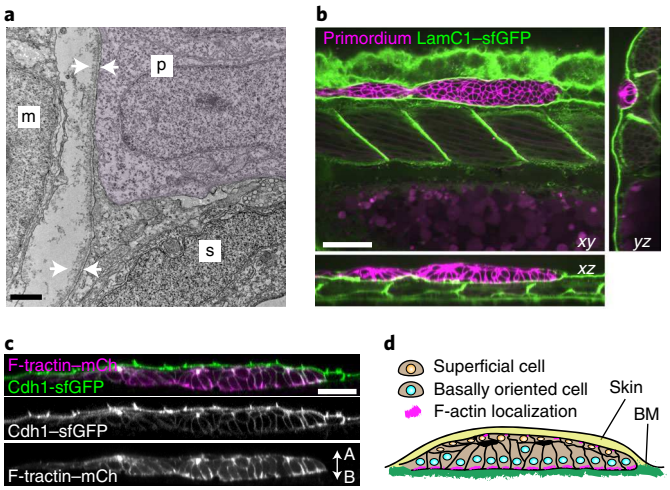

Fig. 1 | The primordium migrates on top of the BM and directly under the skin. a, TEM images of the skin (s), the primordium (p, purple hue), the muscle (m) and the BM (white arrows). $n = 1$ embryo. **b**, Optical sections through a primordium in a 31 h.p.f. embryo expressing LamC1–sfGFP. **c**, Optical section through a primordium labelled with F-tractin–mCherry (mCh) in a live 32 h.p.f. embryo expressing Cdh1–sfGFP. $n = 7$ embryos. A, apical; B, basal. **d**, Schematic illustration of the environment around the primordium. Scale bars, 1 µm (**a**), 25 µm (**c**) or 50 µm (**b**).

sources (Fig. 2f). While local secretion of Cxcl12a from the muscle of *cxcl12a* mutant control embryos attracted the primordium, Cxcl12a failed to restore directed migration towards the chemokine sources in *lamC1; cxcl12a* double-mutant embryos (Fig. 2g,h). In *cxcl12a* mutant control embryos with ectopic Cxcl12a in the muscle, the primordia did not travel the same distance as in wild-type embryos with or without ectopic clones (Extended Data Fig. 2h). The reason for this is that we could not generate clones in the muscle all along the migratory route of the primordium. Importantly, ectopic Cxcl12a triggered the internalization of its receptor Cxcr4b in primordia of *lamC1; cxcl12a* double-mutant embryos and in *cxcl12a* mutant control embryos, which indicates that the diffusion and presentation of Cxcl12a is not impaired in the absence of LamC1 and the BM (Fig. 2i–k and Extended Data Fig. 2i). Thus, an intact BM is required for directed primordium migration, which indicates that the primordium relies mostly on the BM rather than the skin as a substrate for its migration—a notion that is corroborated by the increased levels of filamentous actin (F-actin) on the basal side of the cells (Fig. 1c).

The primordium cells form nascent adhesion-like clusters. To push, pull and exert stresses on the BM, the primordium needs to adhere to the BM. Molecularly, cells can adhere to the BM through focal adhesions. Two core components of these large protein complexes are integrins and talins[12]. Integrins bind to specific BM components on the outside the cell and—through talins and other adaptors—to the actin network inside the cell. To test whether the primordium uses focal adhesions to interact with the BM, we first identified the β-integrins and talins that the primordium expresses. Of the 12 β-integrins and 3 talins in zebrafish, *integrin-β_{1b}* (*itgb1b*) and *talin1* (*tln1*) were expressed throughout the primordium (Extended Data Fig. 3a,d). We therefore tagged *itgb1b* and *tln1* with sfGFP and YPet at the endogenous locus and on a bacterial artificial chromosome (BAC) transgene, respectively (Extended Data Fig. 3b,e). Itgb1b–sfGFP and Tln1–YPet recapitulated the endogenous expression pattern (Extended Data Fig. 3c,f) and restored viability when placed in the respective mutant background (viable *itgb1b-sfGFP$^{-/-}$* and *tln1:tln1-YPet; tln1$^{-/-}$* adults, $n = 20$ and 5, respectively). While Itgb1b–sfGFP and Tln1–YPet were enriched at the myotendinous junctions of the muscle, Itgb1b–sfGFP localized uniformly on the membranes of the primordium cells (Fig. 3a and Supplementary Video 2), and Tln1–YPet was mostly localized in the cytoplasm of the cells of the primordium (Fig. 3b and Supplementary Video 2). Since Itgb1b–sfGFP and Tln1–YPet are also expressed by the surrounding skin and muscle, this expression could mask protein clustering on the membranes of the primordium cells. We therefore used blastomere transplantation to generate embryos in which only a few cells in the primordium express Itgb1b–sfGFP or Tln1–YPet together with membrane-tethered mCherry (mem-mCherry) (Fig. 3c). This analysis revealed that Itgb1b–sfGFP and Tln1–YPet formed short-lived clusters with a lifetime of less than 2 min on the basal sides of the cells in the primordium, often within the basal protrusions (Extended Data Fig. 4b,c). We also detected short-lived Itgb1b–sfGFP clusters on the apical side of the superficial cells (Extended Data Fig. 4a)—a layer of thin primordium cells that face the skin[8,13]. These clusters are probably induced by fibronectin or proteoglycans—labelled by chondroitin sulfate—that are expressed around the primordium (Extended Data Fig. 1k,l). Since talin links integrin to F-actin[12], we asked whether clustered Itgb1b and Tln1 colocalized with F-actin. Chimeric analysis showed that this is the case; Itgb1b–sfGFP and Tln1–YPet clusters colocalized with F-tractin-labelled F-actin on the basal sides of primordium cells (Fig. 3d–f and Supplementary Video 3). Control experiments showed that Itgb1b–sfGFP and, to a lesser degree, Tln1–YPet also colocalized with mem-mCherry, as expected for a transmembrane protein and a cytosolic protein, respectively (Extended Data Fig. 4d,e). Thus, the primordium cells form small, transient integrin–talin–F-actin clusters on their basal sides.

We corroborated the transient nature of the integrin clusters by measuring the mobility of integrin in the membrane through fluorescent recovery after photobleaching (FRAP). Ligated integrin couples to the actin network and diffuses more slowly in the membrane than unligated integrin[14,15]. The mobility of integrin is therefore a measure of the degree by which ligated integrins interact with actin. Consistent with integrin function in muscle, the mobility of Itgb1b–sfGFP at the myotendinous junction was increased when ROCK-mediated actin network contractions were blocked (Extended Data Fig. 4f–h). In comparison to the myotendinous junction, the mobility of Itgb1b–sfGFP was higher in the cells of the primordium (Extended Data Fig. 4i–k), which supports the idea that integrin interacts with the actin network only transiently in this migrating tissue. In contrast to migrating cells in vitro[16,17], these observations suggest that the primordium cells do not form long-lived focal adhesions but rather transient integrin clusters. When placed on a laminin-coated surface, primordium cells formed large integrin and talin clusters along F-actin cables, as observed in cultured cells[16,17] (Extended Data Fig. 4l–n), which indicates that primordium cells can form focal adhesions and stress fibres ex vivo but do not do so in vivo.

Integrin and talin are required for efficient migration. Next, we asked whether integrin and talin function are required for primordium migration. Since *itgb1b* and *tln1*—and possibly *itgb1a*, *tln2a* and *tln2b*—are expressed in the primordium, we generated mutants in these five genes (Extended Data Figs. 5a and 6a). Phenotypic analysis showed that the primordium was less elongated and migrated more slowly in *itgb1b* mutant embryos than in wild-type controls (Fig. 4a–d, Extended Data Fig. 5b–f and Supplementary Video 4). Since *itgb1a$^{-/+}$*; *itgb1b$^{-/-}$* and *itgb1a$^{-/-}$*; *itgb1b$^{-/-}$* embryos exhibited severe morphogenesis defects (Extended Data Fig. 5b), we could not assess primordium migration in these genetic scenarios. Instead, we assessed whether Itgb1b is required within the tissue for migration by depleting Itgb1b–sfGFP in the primordium

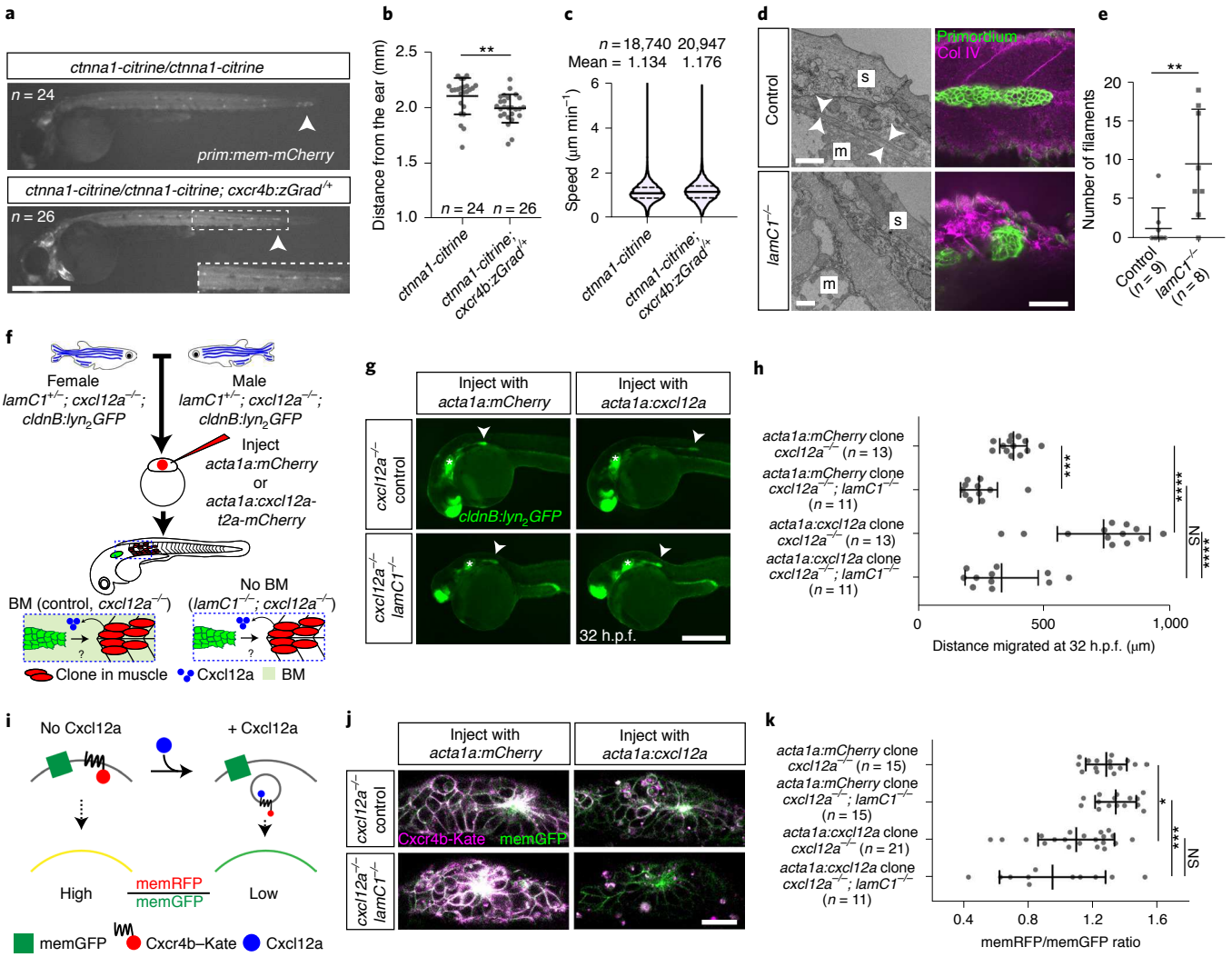

Fig. 2 | Primordium migration requires an intact BM. a, Control and Ctnna1-depleted primordia (arrowheads) in 48 h.p.f. embryos. Close-up of the region is indicated by a dashed square. **b**, Quantification of the migration distance for primordia shown in **a**. $^{**}P = 0.0013$ (two-tailed Mann–Whitney test). **c**, Speed of Ctnna1-depleted primordium cells. The solid line indicates the median, whereas the dashed line indicates the quartile. *n* = cell speeds from more than 7 primordia with each more than 100 cells. **d**, Left: TEM images of the ultrastructure of the BM between the skin and the muscle in control (*n* = 2) and *lamC1*$^{-/-}$ embryos (*n* = 1). White arrowheads indicate the BM. Right: antibody staining against collagen IV (Col IV) in control and *lamC1*$^{-/-}$ embryos. **e**, Quantification of collagen IV filaments in control and *lamC1*−/− embryos. $^{**}P = 0.0056$ (two-tailed Mann–Whitney test). **f**, Schematic of the strategy used to express Cxcl12a in a few muscle cells in *lamC1*$^{-/-}$ embryos and siblings. **g**, Images of the migrating primordium in *cxcl12a*$^{-/-}$ and *cxcl12a*$^{-/-}$; *lamC1*$^{-/-}$ 32 h.p.f. embryos with clones in the trunk muscle that express mCherry (not shown) or Cxcl12a together with mCherry (not shown). Asterisks indicate the ear and arrowheads the primordium. **h**, Quantification of the distance migrated by the primordium in the indicated experimental conditions at 32 h.p.f. $^{***}P = 0.0002$, $^{****}P < 0.0001$, NS, not significant, $P = 0.0879$ (two-tailed Mann–Whitney test). **i**, Illustration of the principle of the Cxcl12a sensor. **j**, Images of the Cxcl12a sensor in primordia of *cxcl12a*$^{-/-}$ and *cxcl12a*$^{-/-}$; *lamC1*$^{-/-}$ live embryos with clones in the muscle of the trunk that express mCherry or Cxcl12a. **k**, Quantification of the Cxcr4b-Kate-to-memGFP ratio in the primordia of embryos shown in **j**. $^{*}P = 0.038$, $^{***}P = 0.0001$, NS, $P = 0.1349$ (one way ANOVA followed by Holm–Sidak's multiple comparison test). Note, controls are *lamc1*+/+ and *lamc1*−/+ embryos. For **a**, **b**, **e**, **h** and **k**, *n* indicates the number of embryos. For **b**, **e**, **h** and **k**, individual data points, mean and s.d. are indicated. Scale bars, 2 μm (**d**, left), 20 μm (**j**), 50 μm (**d**, right) or 0.5 mm (**a**,**g**).

of *itgb1a*$^{-/-}$; *itgb1b-sfGFP*$^{/-}$ embryos using zGrad (Fig. 4e and Extended Data Figs. 2a and 5g,h). In such embryos, primordium migration was slowed to almost the same degree as in *itgb1b* mutant embryos (Fig. 4f,g), which indicates that Itgb1b is required within the primordium for efficient migration with a minor contribution from Itgb1a.

In *talin* single-, double- and triple-mutant embryos, the primordium migrated normally and morphogenesis was mostly unaffected (Extended Data Fig. 6b,c). A possible explanation for the mild defects in *tln1*$^{-/-}$; *tln2a*$^{-/-}$; *tln2b*$^{-/-}$ embryos could be the maternal contribution (M) of *talin* mRNA and talin protein to the embryo. To address this possibility, we generated zygotic (Z) *Z tln1*$^{-/-}$; *Z tln2a*$^{-/-}$; *Z tln2b*$^{-/-}$ embryos that also lacked the maternal contribution (M) of *M tln1* and *M tln2b* (Extended Data Fig. 6d). However, such embryos had somitogenesis defects and disrupted *cxcl12a* expression along the migratory route of the primordium (Extended Data Fig. 6e–g), which impeded the analysis of the role of talin in primordium migration. Next, we depleted Tln1–YPet in the primordium by expressing zGrad from the *cxcr4b* promoter in *MZ tln1*$^{-/-}$; *Z tln2a*$^{-/+}$ or *Z tln2a*$^{+/+}$; *MZ tln2b*$^{-/-}$ embryos, whose only source of Tln1–YPet was maternally deposited mRNA and protein (Fig. 4h). zGrad efficiently degraded Tln1–YPet (Extended Data Fig. 6h,i). This analysis showed

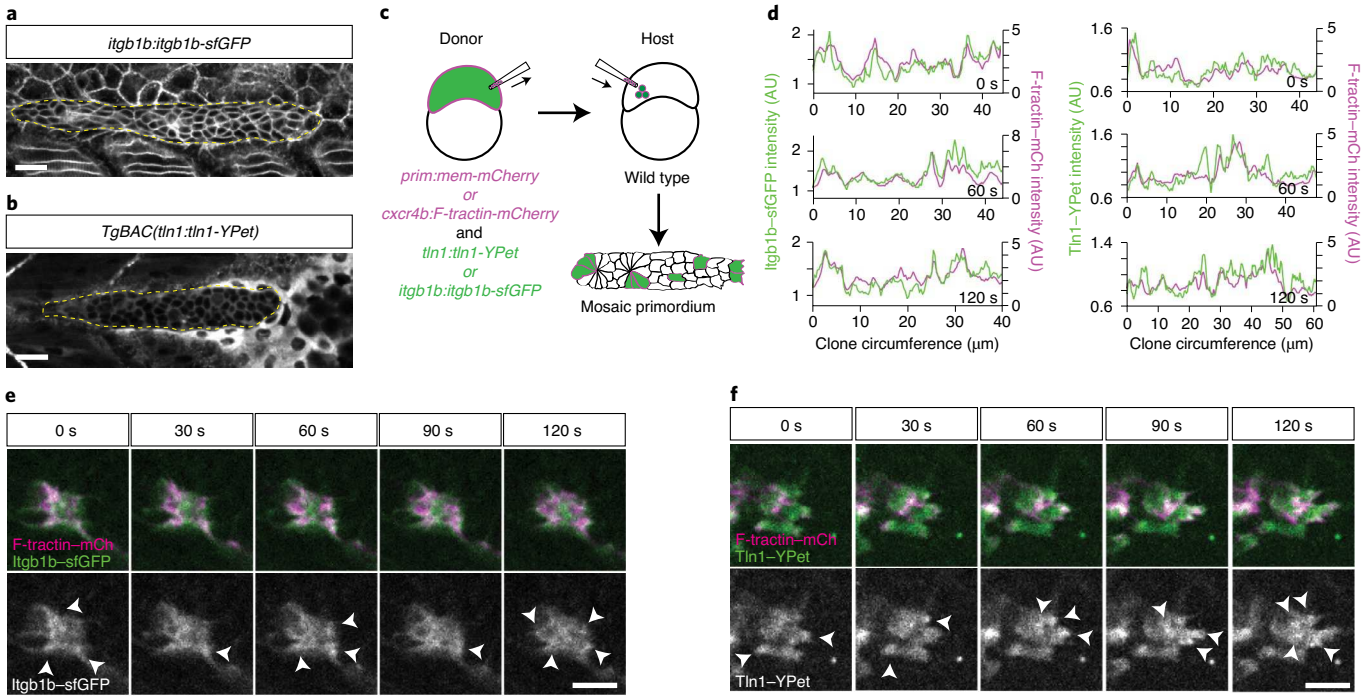

Fig. 3 | Integrin-β_1 and talin form small short-lived clusters at the basal sides of the primordium cells. a, Expression of Itgb1b–sfGFP from the endogenous locus in a 33 h.p.f. embryo. The image is a single slice from a *z*-stack. The primordium is outlined by a dotted yellow line. **b**, Expression of Tln1–YPet from the *tln1:tln1-YPet* BAC transgene in a 33 h.p.f. embryo. The image is a single slice from a *z*-stack. The primordium is outlined by a dotted yellow line. **c**, Schematic of blastomere transplantation experiments. **d**, Intensity profiles of Itgb1b–sfGFP (left) and Tln1–YPet (right) with F-tractin–mCherry along the perimeter on the basal sides of the clones shown in **e** and **f** over time. AU, arbitrary units. **e**, Images of Itgb1b–sfGFP and F-tractin–mCherry localization at the basal side of a clone in the primordium over time. Images are single slices from a time-lapse movie (Supplementary Video 3). Arrowheads indicate Itgb1b–sfGFP/F-tractin–mCherry clusters. **f**, Images of Tln1–YPet and F-tractin–mCherry localization at the basal side of a clone in the primordium over time. Images are single slices from a time-lapse movie (Supplementary Video 3). Arrowheads indicate Tln1–YPet/F-tractin–mCherry clusters. Scale bars, 10 μm (**e**,**f**) or 20 μm (**a**,**b**).

that depleting most of the talin activity in the primordium slowed the migration of the primordium (Fig. 4i,j and Supplementary Video 5), as reported for *tln1* morphants[13]. We confirmed this observation by placing cells with strongly reduced talin activity in the migrating primordia by blastomere transplantation (Extended Data Fig. 6j). Compared with controls, such primordia also migrated slower (Extended Data Fig. 6k–m and Supplementary Video 5).

Talin and other cytosolic partners of integrin bind to the NPxY motifs in the cytoplasmic tail of integrin[12]. We therefore deleted the two NPxY motifs in Itgb1b and tagged Itgb1b$^{\Delta NPxY}$ with sfGFP at its endogenous locus (Fig. 4k and Extended Data Fig. 7a). Compared with Itgb1b–sfGFP, Itgb1b$^{\Delta NPxY}$–sfGFP localized less to the apical and basal sides of the cells in the primordium and its levels were reduced by 16% (Fig. 4l,m). This was also observed for the myotendinous junctions (Extended Data Fig. 7b,c). Consistent with its more uniform distribution, Itgb1b$^{\Delta NPxY}$–sfGFP was more mobile than Itgb1b–sfGFP in the membrane (Extended Data Fig. 7d–f). Similar to the global and tissue-specific loss of Itgb1b,

Fig. 4 | Integrin-β_1, talin and their interaction are required for efficient primordium migration. a, Maximum-projected *z*-stacks of migrating primordia in wild-type and *itgb1b*$^{-/-}$ embryos temporally colour-coded as indicated. **b**, Cumulative primordium migration distance in control and *itgb1b*$^{-/-}$ embryos. Mean and s.d. values are indicated. $^{**}P = 0.0053$ (two-tailed *t*-test at the end point). **c**, Maximum-projected *z*-stacks of primordia in wild-type and *itgb1b*$^{-/-}$ embryos. **d**, Primordium circularity in control and *itgb1b*$^{-/-}$ embryos. Mean and s.d. values are indicated. $^{*}P = 0.035$ (two-tailed *t*-test at the end point). **e**, Schematic of the crossing scheme used to generate embryos with primordium-specific depletion of Itgb1b–sfGFP. **f**, Images of primordium migration in 48 h.p.f. embryos of the indicated genotypes. Primordium-specific Itgb1 depletion refers to the genotype shown in **e**. Arrows indicate primordia, arrowheads indicate the *cxcr4b:zGrad* transgene marker. **g**, Primordium migration distance of embryos shown in **f**. Individual data points, means and SD are indicated. $^{****}P < 0.0001$ (one-way analysis of variance (ANOVA) followed by Tukey's multiple comparison test). **h**, Crossing scheme to generate embryos with reduced Talin activity in the primordium. **i**, Maximum-projected *z*-stacks of migrating primordia in embryos of the indicated genotypes colour-coded for time as indicated. **j**, Cumulative primordium migration distance in *cxcr4b:zGrad* and *(MZ)tln1*$^{-/-}$*; (Z)tln2a*$^{+/-}$ or $^{+/+}$*; (MZ)tln2b*$^{-/-}$*; cxcr4b:zGrad* embryos. The mean and s.d. values are indicated. $^{****}P < 0.0001$ (two-tailed *t*-test at the end point). **k**, Amino-acid alignment of indicated integrin-β_1 cytoplasmic domains, with the two NPxY motifs indicated in red. **l**, Itgb1b–sfGFP and Itgb1b$^{\Delta NPxY}$–sfGFP localization in the primordium. Images are single transverse sections from *z*-stacks. sfGFP intensity (arbitrary units) in lower panels. **m**, Quantification of the Itgb1b–sfGFP and Itgb1b$^{\Delta NPxY}$–sfGFP distribution on the membrane of primordium cells along the apico-basal axis normalized to the fluorescence intensity of mem-mCherry. $^{*}P = 0.012$ at 1.3 μm (two-tailed Welch's *t*-test). Individual data points (pale dots), mean (dots) and s.d. values are indicated. **n**, Primordium position in *itgb1b:itgb1b-sfGFP*$^{-/-}$ and the *itgb1b:itgb1b*$^{\Delta NPxY}$*-sfGFP*$^{-/-}$ 48 h.p.f. embryos. Arrows indicate primordia. **o**, Quantification of the primordium migration distance. Individual data points, mean and s.d. values are indicated. $^{****}P < 0.0001$ (two-tailed Mann–Whitney test). For **b**, **d**, **g**, **j**, **m** and **o**, *n* indicates the number of embryos. Scale bars, 25 μm (**c**,**l**), 100 μm (**a**,**i**), 500 μm (**f**) or 0.5 mm (**n**).

Itgb1b$^{\Delta NPxY}$–sfGFP also failed to support efficient primordium migration (Fig. 4n,o). This indicates that the integrin–talin complex is important for the primordium to move along its migratory route at normal speed.

Integrin-β_1 slows actin flow in the primordium. In migrating cells, the integrin–talin complex can couple F-actin flow inside the cell to the BM outside the cell and transduce force[18]. To test whether the cells in the primordium use such a clutch-like mechanism, we measured the speed of F-actin flow on the apical and basal sides of cells in the primordium of wild-type and *itgb1b* mutant embryos by labelling F-actin with F-tractin–mNeonGreen (F-tractin–mNG) in a few cells of the primordium (Fig. 5a). This analysis showed that F-actin was concentrated in the front of wild-type cells, in the basal cells of the primordium at the basal sides of the cells (Fig. 5b) and in the apically located superficial cells of the primordium on the apical side of the cells (Extended Data Fig. 7g). The F-actin flow was halted or slowed towards the rear of the cells, with a mean speed of 1.5 µm min^{-1} in the basal cells of the primordium (Fig. 5b,c and Supplementary Video 6), whereas F-actin flowed faster in the superficial cells with a mean speed 7.4 µm min^{-1} (Fig. 5d and Supplementary Video 6). Removal of Itgb1b function did not significantly affect the pattern or speed of actin flow in the superficial cells (Fig. 5d, Extended Data Fig. 7g and Supplementary Video 6). In contrast, F-actin flow increased to 6.6 µm min^{-1} in *itgb1b* mutant basal cells of the primordium, and F-actin formed radial cables

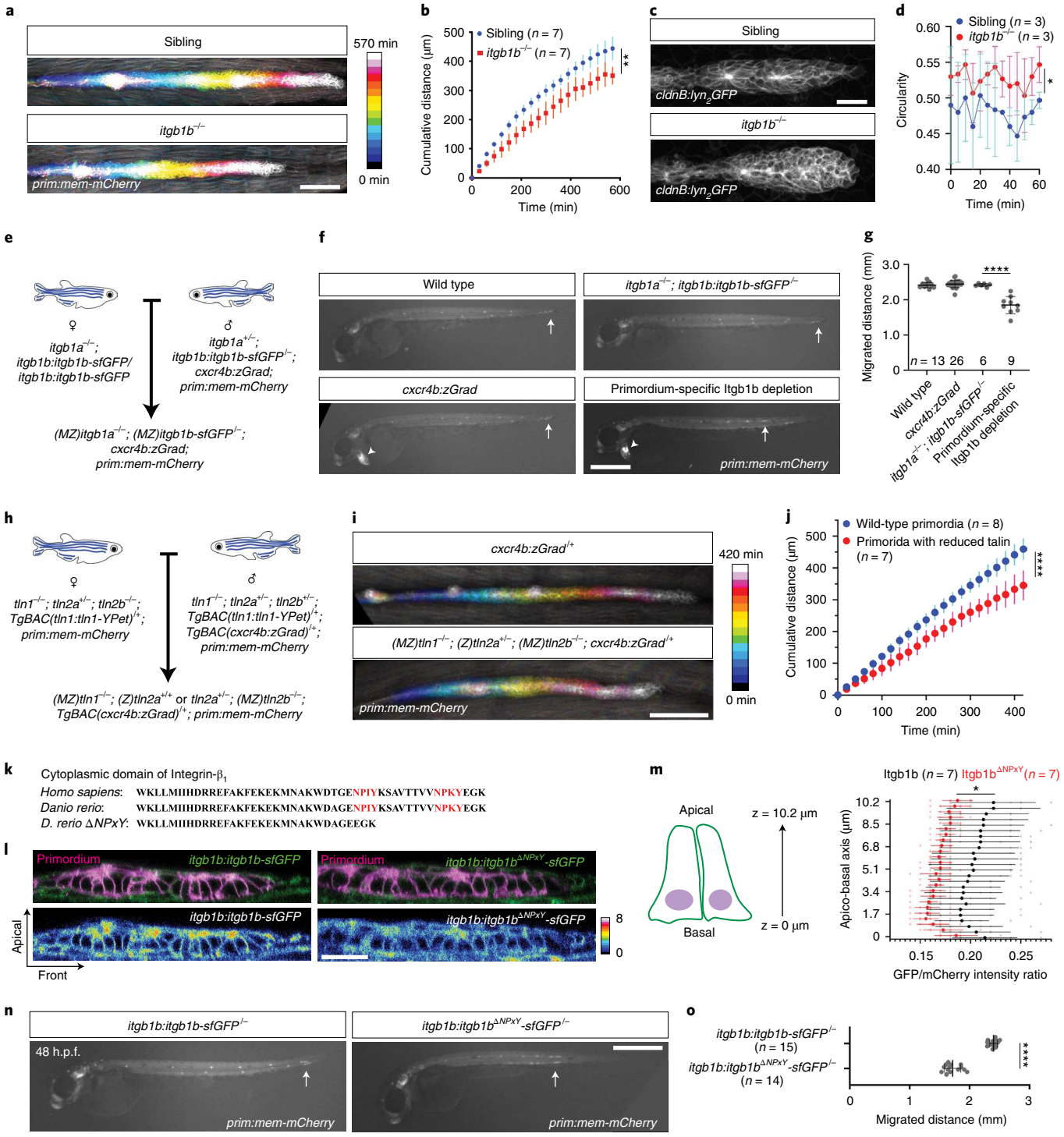

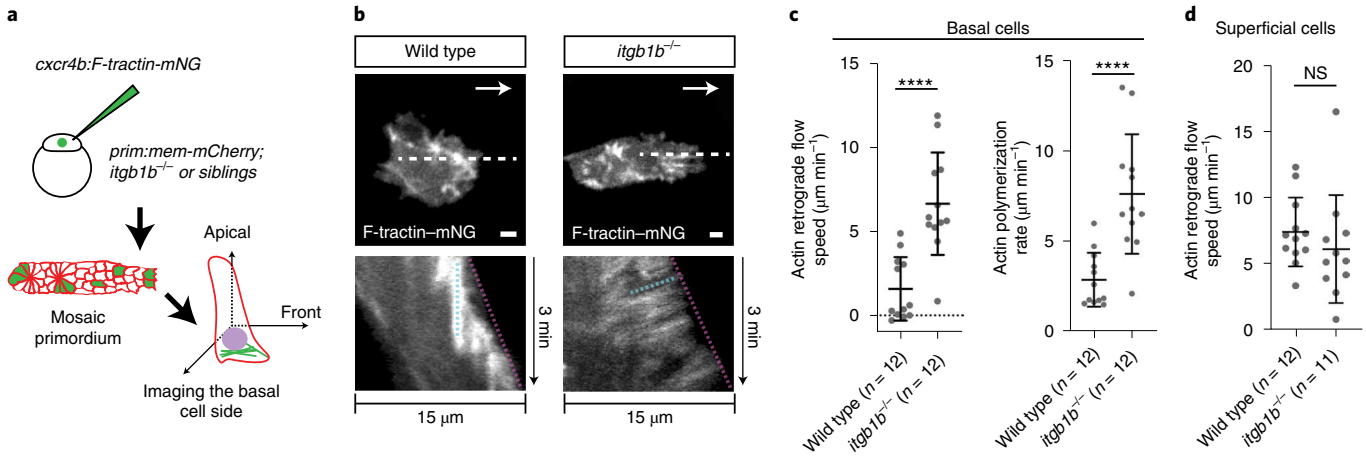

Fig. 5 | Integrin-β_1 couples cell–substrate adhesion to actin flow in the primordium. a, Schematic of the experimental design used to assess actin flow. **b**, Images of F-tractin–mNG localization at the basal sides of wild-type and *itgb1b*$^{-/-}$ primordium cells (top). White arrows indicate the direction of migration. Scale bar, 2 μm. Images are single optical sections from Supplementary Video 6. Kymographs of Supplementary Video 6 along the dotted line are indicated in the top images (bottom). The dotted cyan and magenta lines indicate the rates of actin flow and protrusion, respectively. **c**, Quantification of the rates of actin flow (left) and actin polymerization (right) in the primordium basal cells. Individual data points (dots), mean (horizontal lines) and s.d. (vertical lines) values are indicated. ****$P < 0.0001$ (two-tailed Mann–Whitney test). **d**, Quantification of the rate of actin flow in superficial primordium cells. NS, $P = 0.3708$ (two-tailed *t*-test). Individual data points (dots), mean (horizontal lines) and s.d. (vertical lines) values are indicated. For **c** and **d**, *n* indicates the number of cells pooled from more than five primordia in each condition.

that have also been observed in talin-depleted cells in culture[19] (Fig. 5b,c and Supplementary Video 6). In basal primordium cells, the actin polymerization rate—the sum of the actin flow rate and the rate of membrane protrusion—also increased from 2.8 μm min^{-1} in wild-type control cells to 7.6 μm min^{-1} in *itgb1b* mutant cells (Fig. 5c and Extended Data Fig. 7h,i). Thus, integrins couple force for primordium motility on the basal but not the apical sides of cells in the primordium, and loss of force coupling through integrin results in an increase in the actin polymerization rate on the basal sides of the primordium cells.

The primordium exerts the highest stresses in its rear. If the primordium uses integrin and talin to pull on the BM and push itself forward, the primordium should exert stresses (force per area) on the BM and deform the BM. Such traction stresses have been measured for migrating cells in culture by imaging the displacement of fluorescent beads embedded in elastic surfaces or matrices and the bending of flexible cantilevers—collectively referred to as traction force microscopy[20–28]. To extend traction force microscopy to living embryos, we created optical landmarks on the BM and assessed how these landmarks are displaced as the primordium moves across them (Fig. 6a). Using a laser, we locally bleached LamC1–sfGFP in an approximately cylindrical volume in the BM (Extended Data Fig. 8a,b and Supplementary Video 7). Minimal LamC1–sfGFP diffused back into the bleached cylinder (Extended Data Fig. 8c,d), and bleached cylinders remained clearly demarcated for 2 h after photobleaching (Supplementary Video 8), whereas untagged, extracellular mCherry rapidly filled bleached cylinders after bleaching (Extended Data Fig. 8c). This indicated that bleaching LamC1–sfGFP is a suitable approach to place local marks on the BM and monitor the deformation of the BM over time. We therefore bleached a hexagonal pattern of marks onto the LamC1–sfGFP-labelled BM in front of the migrating primordium and recorded the position of the marks as the primordium migrated across this pattern (Extended Data Fig. 8a and Supplementary Video 8). To reconstruct the stresses from the displacement of the marks on the BM by the migrating primordium, we developed the analysis pipeline Embryogram[29] (Extended Data Fig. 8e,f; https://zenodo.org/record/5762146#.Ya5X0y-B1QJ), which is inspired by the Cellogram algorithm[30]. Embryogram identifies the bleached cylinders in the first frame of the time lapse. This assigns a point in space to each mark in the first frame. The points are connected using a variant of the iterative closest point algorithm to obtain a triangular mesh. This mesh is then deformed to follow the marks on the BM in the subsequent frames of the time lapse, which leads to a time sequence of triangular meshes that captures the deformation of the BM (Extended Data Fig. 8f). The time-varying mesh is used to compute displacements between the marks. To convert the displacements into stresses, we filled an axis-aligned box that contains the sample with a volumetric tetrahedral mesh. This mesh contains the surface mesh that approximates the BM in the first frame of the time lapse. The stresses are then computed by solving an elastic deformation of the volumetric mesh (for details, see Supplementary Note 1). For this conversion, we determined the stiffness, or Young's modulus, of the BM. We removed the skin above the BM and measured the BM stiffness by atomic force microscopy (AFM) (Extended Data Fig. 8g). In agreement with previous in vivo studies that assessed stiffness at the micron scale[31,32], this analysis yielded a Young's modulus for the BM of 566 ± 355 Pa (mean ± s.d.), which was reduced to 321 ± 158 Pa (mean ± s.d.) after collagenase treatment (Fig. 6b,c and Extended Data Fig. 8h–k), a value that probably reflects the stiffness of the underlying muscle (Extended Data Fig. 8i,m). Importantly, spontaneous twitches of skin cells contract the underlying BM. This causes the BM to buckle and wrinkle akin to the distortions of the substrate observed around cultured cells[33] and in animals[34]. The wrinkles formed and disappeared in less than 2 min, and tracking the optical marks indicated that the wrinkles do not cause lasting deformation of the BM (Extended Data Fig. 9a–e and Supplementary Video 9). Similarly, repeated probing of the BM at the same location in deskinned embryos by AFM did not alter the stiffness measurements (Extended Data Fig. 8l). These observations suggest that the BM undergoes non-plastic deformations and can be approximated by a linear stress–strain relationship.

Using the Embryogram pipeline together with the stiffness measurements, we found that the front cells of the primordium pull slightly on the BM in random directions. In contrast, the cells in the middle and rear cells of the primordium pull on the BM more strongly and more directional, displacing the BM side-

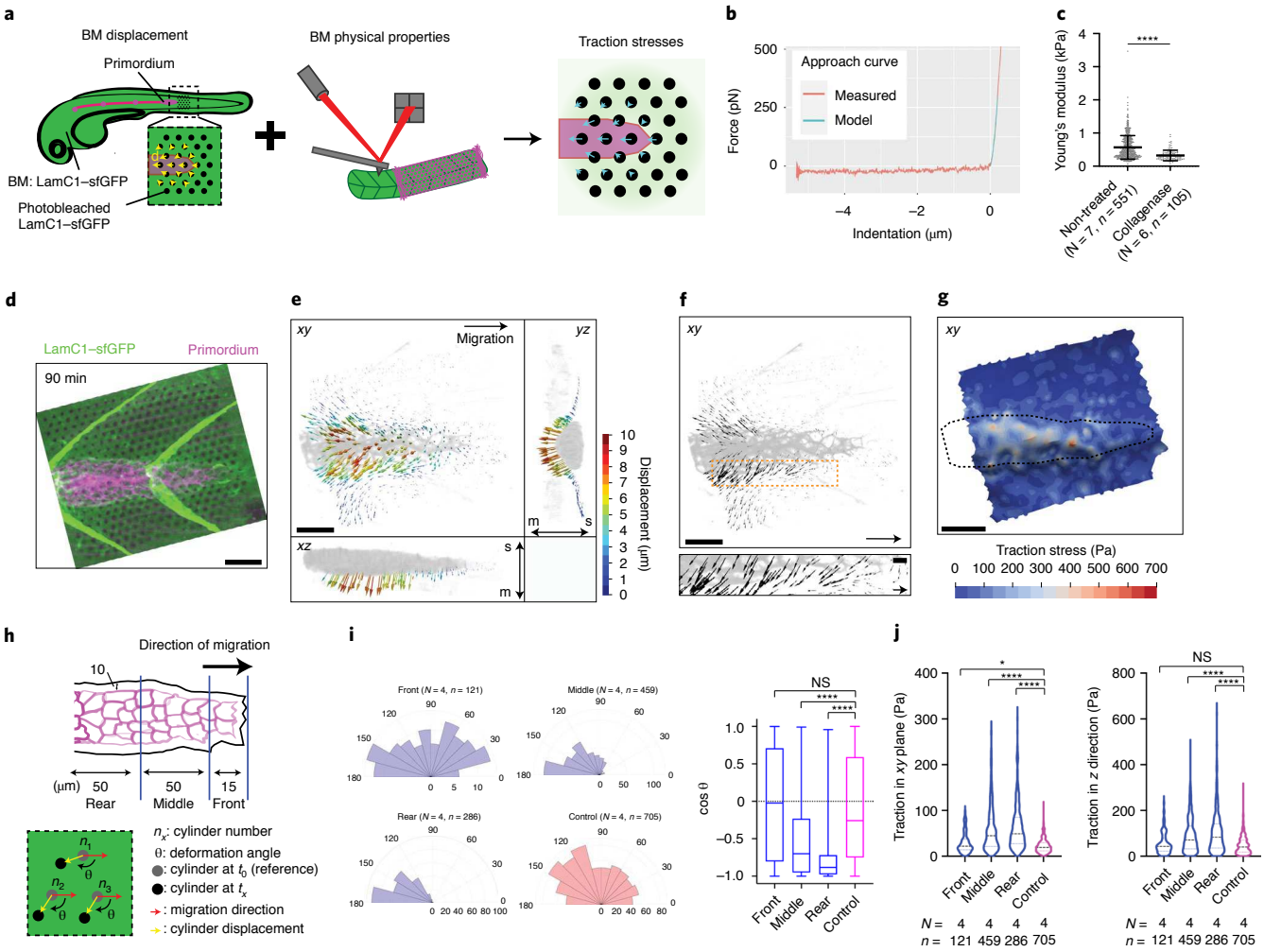

Fig. 6 | Traction stress measurements indicate that the primordium exerts the highest stresses in its rear. a, Schematic of the strategy used to measure traction stresses in vivo. **b**, Representative force curve of BM stiffness measurement by AFM. Fit of the first 200 nm after the contact point at 0 μm to the Hertz model is indicated in cyan. Only the approach part of the force curve is shown. **c**, Quantification of the BM stiffness with and without (Non-treat) collagenase treatment. *N* indicates the number of embryos, *n* indicates the number of recorded approach curves. Individual data points, mean and s.d. values are indicated. ****$P < 0.0001$ (two-tailed Mann–Whitney test). **d**, Maximum-projected *z*-stack (Supplementary Video 8). Scale bar, 25 μm. **e**, BM displacement by the primordium (grey) shown as a vector field along the *x*, *y* and *z* axes (Supplementary Video 10). The displacement vector magnitude is indicated as a colour map. The *xy* view is shown from the basal side of the primordium. Scale bar, 25 μm. m, muscle; s, skin. **f**, Top: BM displacement in the *xy* plane by the primordium (grey) shown as a vector field (Supplementary Video 10). The displacement field in the *xy* plane is shown from the basal side of the primordium. Scale bars, 25 μm (bar) or 50 μm (arrow). Bottom: magnification of the outlined region in the top panel. Scale bars, 25 μm (bar) or 10 μm (arrow). **g**, Traction stress magnitudes on the BM indicated as a colour map (Supplementary Video 10). Scale bar, 25 μm. **h**, Schematic of the approach used to quantify the traction stresses and BM displacement vector direction. **i**, BM displacement vector angles with respect to the migration direction (0°). Mean, 25th–75th percentiles (box), and minimum and maximum (whiskers) values are indicated. *N* indicates the number of embryos, *n* indicates the number of bleached cylinders. ****$P < 0.0001$ and NS, $P = 0.6291$. **j**, Pooled traction stresses exerted by the primordium on the BM. The magnitude in *xy* plane (left) and along the *z* axis (right) with median (dashed line) and quartile (dotted line) are shown. *$P = 0.0302$, ****$P < 0.0001$, NS, $P = 0.2273$ (two-tailed Mann–Whitney test). *N* indicates the number of embryos, *n* indicates the number of bleached cylinders analysed. For **c**, **i** and **j**, *n* was used for statistical tests.

ways, backwards and downwards (Fig. 6d–f and Supplementary Video 10). The traction stresses (the forces against the plane of the BM) reflected this displacement pattern. In the front, the mean traction stresses averaged 28 ± 22 Pa, and increased to 58 ± 49 Pa and 64 ± 51 Pa (mean ± s.d.) in the middle and rear of the primordium, respectively, with higher traction stresses exerted preferentially along the sides of the primordium and peaking at 600 Pa (Fig. 6g–j and Supplementary Video 10). Similarly, the primordium generated high, mostly rearward-pointing stresses (stresses extracted in the direction of migration) along the sides and towards its rear (Extended Data Fig. 9h), where it also exerted the highest shear stresses on the BM (Extended Data Fig. 9i). Although the primordium moves at relatively constant speed[35], it does not exert constant stresses on its substrate (Supplementary Video 10), which suggests that its forward motion is the result of the average of the fluctuating stresses across the tissue. At the position where the primordium has passed, the BM returned to its original shape and the marks on the BM snapped back to their original position, which indicates that the BM is not irreversibly deformed by the primordium (Extended Data Fig. 9f,g and Supplementary Video 10). Also, we did not observe such BM displacements and stresses in controls in which we blocked primordium migration through

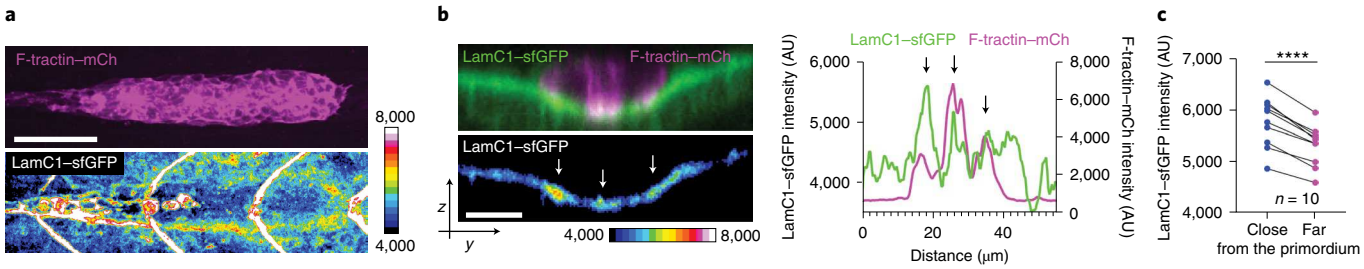

Fig. 7 | The BM wrinkles around the primordium. a, F-tractin–mCherry distribution in the primordium (top) and LamC1–sfGFP around the primordium (bottom) in a 32 h.p.f. embryo. LamC1–GFP fluorescence intensity is pseudo-coloured as a heatmap and shown in arbitrary units. The image is a maximum-projected *z*-stack. **b**, Left, top: a transverse section through the F-tractin–mCherry-expressing primordium and the underlying LamC1–sfGFP-labelled BM. Left, bottom: a corresponding image showing the LamC1–sfGFP fluorescence intensity as a heatmap in arbitrary units. Arrows indicate apposed clusters of F-tractin–mCherry and LamC1–sfGFP. Images are single sections along the *yz* plane of a *z*-stack. Right: fluorescence intensity profiles of F-tractin–mCherry and LamC1–sfGFP of image shown in left along the *y* axis. Arrows indicate the position of the apposed clusters of F-tractin–mCherry and LamC1–sfGFP indicated by arrows in the left panels. **c**, Quantification of the LamC1–sfGFP intensity within 3-μm-wide bands around the perimeter of the primordium (left) and at a distance of 6 μm from the perimeter of the primordium (right). $^{****}P < 0.0001$ (two-tailed paired *t*-test). *n* indicates the number of embryos. Scale bars, 10 μm (**b**) or 50 μm (**a**).

the ubiquitous overexpression of Cxcl12a, which is the attractive guidance cue of the primordium (Fig. 6j, Extended Data Fig. 9j–o and Supplementary Video 10). The observed stress distribution was also reflected in the wrinkling of the BM along the sides of the primordium, with LamC1–sfGFP forming local clusters (Fig. 7a). These LamC1–sfGFP clusters were juxtaposed to F-actin clusters in the primordium (Fig. 7b) and were specifically enriched around the primordium (Fig. 7c), which suggests that actin network contraction in the primordium locally pull on the BM and cause it to wrinkle. Together, these observations indicate that the front cells exert low traction stresses while the rear cells exert high traction stresses. On a tissue level, the primordium moves in a continuous breaststroke-like manner, with its front pushing the BM in random directions while its middle and rear strongly push the BM sideways and backwards. This stress pattern is consistent with theoretical predictions for adherent cell migration[36].

Actomyosin activity is highest in the rear of the primordium. The primordium generates higher stresses in the rear than in the front. This could be because there are more cells in the rear or because the cells in the rear pull stronger on the BM than in the front. Stronger pulling in the rear could be reflected in increased actomyosin activity, slower actin flow rates, increased integrin levels, more engaged integrin, more stable integrin clusters and a greater stress dependence on integrins in the rear than in the front of the primordium. To test these possibilities, we first assessed the activity of actomyosin across the primordium. Since actomyosin activity correlates with the localization of the actin motor non-muscle myosin II into dots, we generated a myosin II reporter line for the primordium (Myl12.1–mScarlet). Consistent with previous studies that used other contexts[37], Myl12.1–mScarlet localized to dots in the cells of the primordium. These dots did not form a cable-like structure around the back of the primordium as in other contexts[37] but were mostly localized to the basal sides of the cells and to the lateral sides in the middle to rear of the primordium (Fig. 8a), and enriched in its rear (Fig. 8b). This suggests that the cells in the rear and the sides of the primordium exert more force than the cells in the front. Actin flow across the primordium was the same (Fig. 8c,d). Itgb1b levels across the primordium were similar (Fig. 8e), and integrin engagement—as judged by the increased clustering of Itgb1b–sfGFP compared with Itgb1b$^{\Delta NPxY}$–sfGFP compared with Itgb1b–tdTomato in embryos in which we modified the two endogenous *itgb1b* alleles—also showed no difference between the front and back of the primordium (Fig. 8f). Itgb1b–sfGFP clustering at the myotendinous junction was increased by fourfold compared with the talin-binding deficient control Itgb1b$^{\Delta NPxY}$–sfGFP (Extended Data Fig. 10a,b). This is consistent with the idea that increased clustering of Itgb1b–sfGFP compared with Itgb1b$^{\Delta NPxY}$–sfGFP reflects integrin engagement. In contrast, the levels of phosphorylated paxillin (p-paxillin)—a putative marker for integrin adhesion turnover[38]—but not total paxillin

Fig. 8 | The primordium generates larger forces in the rear. a, Top: Myl12.1–mScarlet distribution in the primordium. Middle: Myl12.1–mScarlet in the entire primordium. Bottom: Myl12.1–mScarlet on the basal side of the primordium pseudo-coloured. Dotted line indicates the outline of the primordium. **b**, Quantification of the basal Myl12.1–mScarlet intensity at indicated positions in the primordium. Data points, the mean and s.d. values are indicated (one-way ANOVA followed by Tukey's multiple comparison test). **c**, Top: images of F-tractin–mNG at the basal sides of primordium cells. Arrows indicate the direction of migration. Bottom: Kymographs along the dotted line indicated in the top images. **d**, Actin flow rates in basal primordium cells. *n* indicates the number of cells pooled from more than five primordia. Data points, the mean and s.d. values are indicated (two-tailed Mann–Whitney test). **e**, Distribution (top) and quantification (bottom) of Itgb1b–sfGFP on the cell membranes of the primordium. Itgb1b–sfGFP intensity is pseudo-coloured. Mean and s.d. are indicated. **f**, Left: fluorescence intensity ratio images of Itgb1b–tdTomato to Itgb1b–sfGFP (top) and Itgb1b$^{\Delta NPxY}$–sfGFP (bottom) on the membrane of primordium cells. The dotted lines indicate the outline of the primordium. Right: quantification of red/green (R/G) fluorescence intensity ratios. Ratios are shown in pseudo-colour. Mean and s.d. are indicated. **g**, BM displacement around the primordium (grey) in *itgb1b*$^{-/-}$ embryos shown as a vector field along the *x*, *y* and *z* axes (Supplementary Video 10). The vector magnitude is indicated as a colour map. The *xy* view is from the basal side of the primordium. **h**, Traction stresses on the BM indicated as a colour map (Supplementary Video 10). **i**, Pooled traction stresses exerted by the primordium on the BM in *itgb1b*$^{-/-}$ embryos. Median (thick line) and quartile (thin line) are shown. The wild-type control is the same as shown in Fig. 6j (two-tailed Mann–Whitney test). *N* indicates the number of embryos, *n* indicates the number of bleached cylinders. *n* was used for statistics. **j**, Left: staining against paxillin (top) and p-paxillin (bottom) protein in primordia shown as a heatmap. Right: quantification of the fluorescence intensity on the primordium membrane for paxillin (top) and p-paxillin (bottom). Mean and s.d. are indicated. **k**, Model for primordium motility. For **b, e**, **f** and **j**, *n* indicates the number of embryos. Scale bars, 2 μm (**c**), 20 μm (**a**,**e**,**f**,**j**) or 25 μm (**g**,**h**). Coloured bars in **a**,**e**,**f** indicate fluorescence intensities in arbitrary units.

were lower in the rear than the front of the primordium (Fig. 8j), which suggests that the rear of the primordium forms longer-lived integrin-mediated adhesions. Consistent with this idea, the traction stresses in the plane of migration (*xy* plane)—but not the traction stresses against the BM (*z* axis)—decreased more in the rear than in the front of primordia in embryos lacking Itgb1b compared with wild-type embryos but did not become equal in magnitude (Fig. 8g–i and Supplementary Video 10). Thus, Itgb1b couples more force to the BM in the rear of the primordium than in its front and is dispensable for force transmission against BM, but does not account for all the difference in stresses between the front and the rear of the primordium. Together, these observations suggest that the cells in the rear of the primordium generate more force than the cell in its front, which—probably together with the higher cell number in the rear—accounts for the high stresses exerted by the rear of the primordium on the BM.

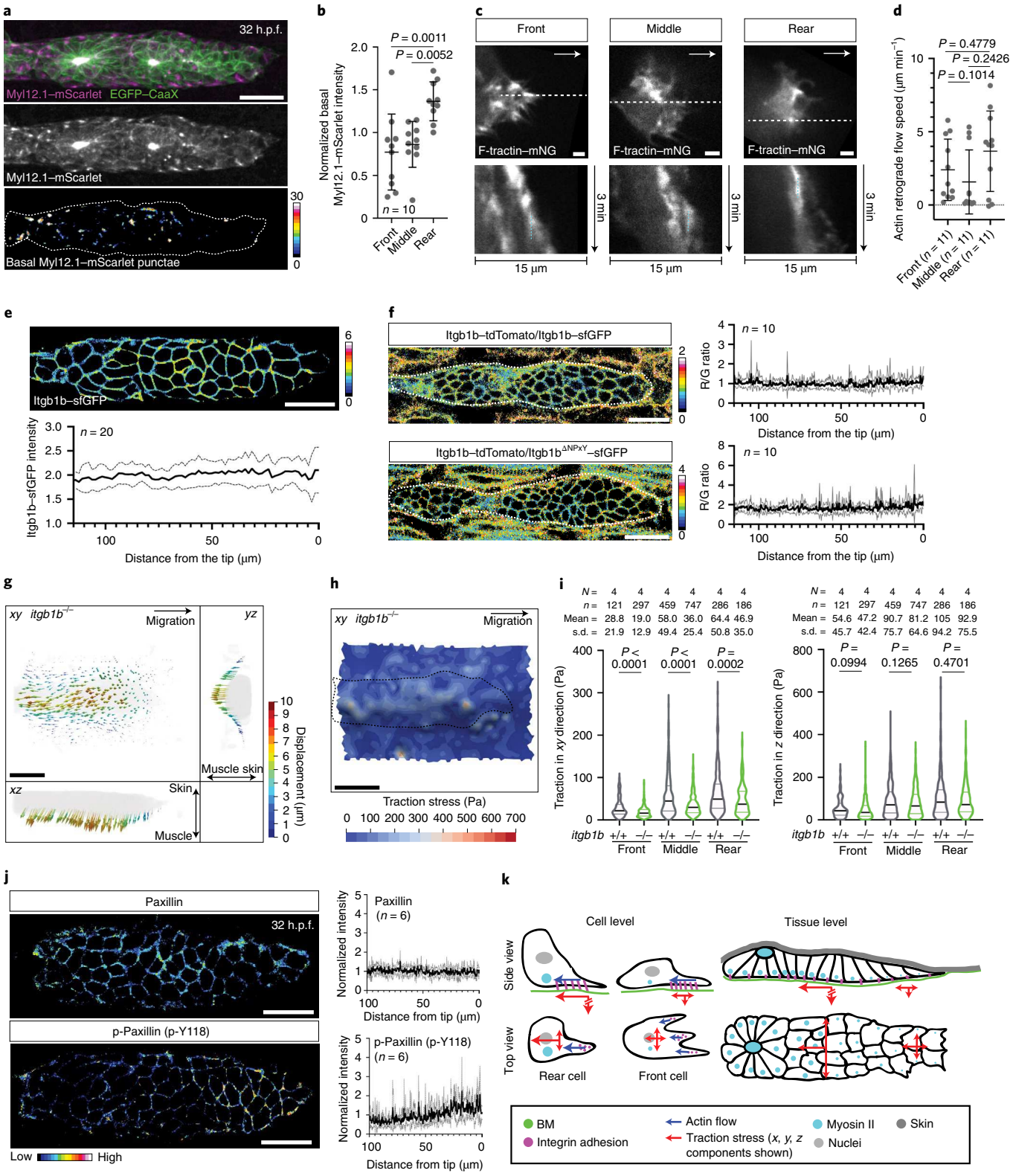

Another migrating tissue that is guided by Cxcl12 and propelled forward by its rear is the cranial neural crest in *Xenopus*[39]. The front cells of the cranial neural crest are attracted by Cxcl12 and the rear cells form a supracellular cable around the back of the tissue. This cable contracts periodically and pushes rear cells forward while front cells become displaced to the side and then to the back (Extended Data Fig. 10e). In contrast, the primordium is attracted by a self-generated Cxcl12a gradient that extends almost across the entire tissue[40,41] (Extended Data Fig. 10c,d), does not form a supracellular actomyosin cable across adherens junctions around its back (Fig. 8a, and Extended Data Fig. 10h,i), does not periodically contract its rear (Extended Data Fig. 10f), and its cells do not intercalate but remain next to their neighbours during migration[11] (Extended Data Fig. 10g and Supplementary Video 1). Thus, although both tissues generate the highest forces in their rear, the underlying guidance and propulsion mechanisms are different and might represent two solutions to the same problem (Extended Data Fig. 10e): how to propel a tissue through an animal.

Discussion

Together, this work elucidates how a tissue moves through a live animal. It provides three major insights. First, primordium cells link the force-generating actomyosin network to the BM through integrin clusters on their basal sides. These integrin clusters are less than 2 µm in size and form and disassemble in less than 2 min. This is in contrast to the larger and longer-lived focal adhesions that migrating cells in culture use to pull themselves forward[16,17] and is more reminiscent of nascent adhesions that form at the edge of protrusions and underneath spreading cells in culture[38,42–44]. This suggests that tissues in animals rely on transient rather than prolonged cell–substrate interactions for movement. Second, the primordium cells pull and deform the BM on their outside with maximal stresses around 600 Pa. This is comparable to the average stress that migrating cells in culture exert on their substrates[20–28], which suggests that stresses in this range are inherent to adherent migration in simplified and physiological scenarios. Consistent with this notion, retrograde actin flow is slowed or stalled in primordium cells, which suggests that most of the flow is converted into forward movement. Intriguingly, disrupting the coupling of actin flow across integrin results in increased flow. Such a compensatory response has also been observed in cultured dendritic cells and macrophages[45]. These cells also increase actin polymerization in response to decreased force coupling to the substrate to maintain forward movement—probably by coupling through other integrins and nonspecific adhesion. Third, the primordium moves similar to a continuous breaststroke by pushing the BM downward, sideways and backwards. Counterintuitively, the rear cells of the primordium generate higher traction stresses than the front cells, probably because the rear cells need to overcome greater resistance in their environment than the front cells. One possible reason for the greater resistance is the front cells, which the rear cells might need to push to move forward. Consistent with this idea, the front cells pull and push the BM in random directions (Fig. 6i), which suggests that they contribute little to directed force generation in the tissue. Also, when severed from the rear cells, the front cells cease to move forward[46]. It therefore seems that the rear pushes the front to propel the primordium forward, a scenario that is akin to a rear-engine-like design (Fig. 8k). Intriguingly, the two collectively migrating heart cells in *Ciona* and crawling *Dictyostelium* slugs, banana slugs and garden snails also push stronger with their rears than their fronts on their surroundings[47–49] which indicates that this propulsion design is conserved across different length scales to drive tissue and animal movement.

Online content

Any methods, additional references, Nature Research reporting summaries, source data, extended data, supplementary information, acknowledgements, peer review information; details of author contributions and competing interests; and statements of data and code availability are available at https://doi.org/10.1038/s41556-022-00844-9.

Received: 10 May 2021; Accepted: 6 January 2022;
Published online: 14 February 2022

References

1. Friedl, P. & Gilmour, D. Collective cell migration in morphogenesis, regeneration and cancer. *Nat. Rev. Mol. Cell Biol.* **10**, 445–457 (2009).
2. Alert, R. & Trepat, X. Physical models of collective cell migration. *Annu. Rev. Condens. Matter Phys.* **11**, 77–101 (2020).
3. Yamada, K. M. & Sixt, M. Mechanisms of 3D cell migration. *Nat. Rev. Mol. Cell Biol.* **20**, 738–752 (2019).
4. Ringer, P., Colo, G., Fassler, R. & Grashoff, C. Sensing the mechano-chemical properties of the extracellular matrix. *Matrix Biol.* **64**, 6–16 (2017).
5. Dalle Nogare, D. & Chitnis, A. B. A framework for understanding morphogenesis and migration of the zebrafish posterior lateral line primordium. *Mech. Dev.* **148**, 69–78 (2017).
6. Metcalfe, W. K. Sensory neuron growth cones comigrate with posterior lateral line primordial cells in zebrafish. *J. Comp. Neurol.* **238**, 218–224 (1985).
7. Parsons, M. J. et al. Zebrafish mutants identify an essential role for laminins in notochord formation. *Development* **129**, 3137–3146 (2002).
8. Dalle Nogare, D. E., Natesh, N., Vishwasrao, H. D., Shroff, H. & Chitnis, A. B. Zebrafish posterior lateral line primordium migration requires interactions between a superficial sheath of motile cells and the skin. *eLife* https://doi.org/10.7554/eLife.58251 (2020).
9. Yamaguchi, N., Colak-Champollion, T. & Knaut, H. zGrad is a nanobody-based degron system that inactivates proteins in zebrafish. *eLife* https://doi.org/10.7554/eLife.43125 (2019).
10. Leckband, D. E. & de Rooij, J. Cadherin adhesion and mechanotransduction. *Annu. Rev. Cell Dev. Biol.* **30**, 291–315 (2014).
11. Colak-Champollion, T. et al. Cadherin-mediated cell coupling coordinates chemokine sensing across collectively migrating cells. *Curr. Biol.* **29**, 2570–2579.e7 (2019).
12. Sun, Z., Costell, M. & Fassler, R. Integrin activation by talin, kindlin and mechanical forces. *Nat. Cell Biol.* **21**, 25–31 (2019).
13. Olson, H. M. & Nechiporuk, A. V. Lamellipodia-like protrusions and focal adhesions contribute to collective cell migration in zebrafish. *Dev. Biol.* **469**, 125–134 (2021).
14. Shibata, A. C. et al. Archipelago architecture of the focal adhesion: membrane molecules freely enter and exit from the focal adhesion zone. *Cytoskeleton (Hoboken)* **69**, 380–392 (2012).
15. Rossier, O. et al. Integrins β_1 and β_3 exhibit distinct dynamic nanoscale organizations inside focal adhesions. *Nat. Cell Biol.* **14**, 1057–1067 (2012).
16. Parsons, J. T., Horwitz, A. R. & Schwartz, M. A. Cell adhesion: integrating cytoskeletal dynamics and cellular tension. *Nat. Rev. Mol. Cell Biol.* **11**, 633–643 (2010).
17. De Pascalis, C. & Etienne-Manneville, S. Single and collective cell migration: the mechanics of adhesions. *Mol. Biol. Cell* **28**, 1833–1846 (2017).
18. Case, L. B. & Waterman, C. M. Integration of actin dynamics and cell adhesion by a three-dimensional, mechanosensitive molecular clutch. *Nat. Cell Biol.* **17**, 955–963 (2015).
19. Zhang, X. et al. Talin depletion reveals independence of initial cell spreading from integrin activation and traction. *Nat. Cell Biol.* **10**, 1062–1068 (2008).
20. Balaban, N. Q. et al. Force and focal adhesion assembly: a close relationship studied using elastic micropatterned substrates. *Nat. Cell Biol.* **3**, 466–472 (2001).
21. Tan, J. L. et al. Cells lying on a bed of microneedles: an approach to isolate mechanical force. *Proc. Natl Acad. Sci. USA* **100**, 1484–1489 (2003).
22. Butler, J. P., Tolic-Norrelykke, I. M., Fabry, B. & Fredberg, J. J. Traction fields, moments, and strain energy that cells exert on their surroundings. *Am. J. Physiol. Cell Physiol.* **282**, C595–C605 (2002).
23. Legant, W. R. et al. Multidimensional traction force microscopy reveals out-of-plane rotational moments about focal adhesions. *Proc. Natl Acad. Sci. USA* **110**, 881–886 (2013).
24. Maskarinec, S. A., Franck, C., Tirrell, D. A. & Ravichandran, G. Quantifying cellular traction forces in three dimensions. *Proc. Natl Acad. Sci. USA* **106**, 22108–22113 (2009).
25. Trichet, L. et al. Evidence of a large-scale mechanosensing mechanism for cellular adaptation to substrate stiffness. *Proc. Natl Acad. Sci. USA* **109**, 6933–6938 (2012).
26. Legant, W. R. et al. Measurement of mechanical tractions exerted by cells in three-dimensional matrices. *Nat. Methods* **7**, 969–971 (2010).
27. Serra-Picamal, X. et al. Mechanical waves during tissue expansion. *Nat. Phys.* **8**, 628–634 (2012).

28. Brugues, A. et al. Forces driving epithelial wound healing. *Nat. Phys.* **10**, 684–691 (2014).
29. Yamaguchi, N. et al. A rear-engine drives adherent tissue migration in vivo. *Zenodo* https://doi.org/10.5281/zenodo.5762146 (2021).
30. Lendenmann, T. et al. Cellogram: on-the-fly traction force microscopy. *Nano Lett.* **19**, 6742–6750 (2019).
31. Pearson, J. R. et al. ECM-regulator *timp* is required for stem cell niche organization and cyst production in the *Drosophila* ovary. *PLoS Genet.* **12**, e1005763 (2016).
32. Kim, S. N. et al. ECM stiffness regulates glial migration in *Drosophila* and mammalian glioma models. *Development* **141**, 3233–3242 (2014).
33. Harris, A. K., Wild, P. & Stopak, D. Silicone rubber substrata: a new wrinkle in the study of cell locomotion. *Science* **208**, 177–179 (1980).
34. Hagedorn, E. J. et al. The netrin receptor DCC focuses invadopodia-driven basement membrane transmigration in vivo. *J. Cell Biol.* **201**, 903–913 (2013).
35. Haas, P. & Gilmour, D. Chemokine signaling mediates self-organizing tissue migration in the zebrafish lateral line. *Dev. Cell* **10**, 673–680 (2006).
36. Bergert, M. et al. Force transmission during adhesion-independent migration. *Nat. Cell Biol.* **17**, 524–529 (2015).
37. Clarke, D. N. & Martin, A. C. Actin-based force generation and cell adhesion in tissue morphogenesis. *Curr. Biol.* **31**, R667–R680 (2021).
38. Zaidel-Bar, R., Milo, R., Kam, Z. & Geiger, B. A paxillin tyrosine phosphorylation switch regulates the assembly and form of cell-matrix adhesions. *J. Cell Sci.* **120**, 137–148 (2007).
39. Shellard, A., Szabo, A., Trepat, X. & Mayor, R. Supracellular contraction at the rear of neural crest cell groups drives collective chemotaxis. *Science* **362**, 339–343 (2018).
40. Dona, E. et al. Directional tissue migration through a self-generated chemokine gradient. *Nature* **503**, 285–289 (2013).
41. Venkiteswaran, G. et al. Generation and dynamics of an endogenous, self-generated signaling gradient across a migrating tissue. *Cell* **155**, 674–687 (2013).
42. Choi, C. K. et al. Actin and α-actinin orchestrate the assembly and maturation of nascent adhesions in a myosin II motor-independent manner. *Nat. Cell Biol.* **10**, 1039–1050 (2008).
43. Changede, R., Xu, X., Margadant, F. & Sheetz, M. P. Nascent integrin adhesions form on all matrix rigidities after integrin activation. *Dev. Cell* **35**, 614–621 (2015).
44. Nayal, A. et al. Paxillin phosphorylation at Ser273 localizes a GIT1–PIX–PAK complex and regulates adhesion and protrusion dynamics. *J. Cell Biol.* **173**, 587–589 (2006).
45. Renkawitz, J. et al. Adaptive force transmission in amoeboid cell migration. *Nat. Cell Biol.* **11**, 1438–1443 (2009).
46. Dalle Nogare, D. et al. Leading and trailing cells cooperate in collective migration of the zebrafish posterior lateral line primordium. *Development* **141**, 3188–3196 (2014).
47. Lai, J. H., del Alamo, J. C., Rodriguez-Rodriguez, J. & Lasheras, J. C. The mechanics of the adhesive locomotion of terrestrial gastropods. *J. Exp. Biol.* **213**, 3920–3933 (2010).
48. Rieu, J. P., Barentin, C., Maeda, Y. & Sawada, Y. Direct mechanical force measurements during the migration of *Dictyostelium* slugs using flexible substrata. *Biophys. J.* **89**, 3563–3576 (2005).
49. Bernadskaya, Y. Y., Yue, H., Copos, C., Christiaen, L. & Mogilner, A. Supracellular organization confers directionality and mechanical potency to migrating pairs of cardiopharyngeal progenitor cells. *Elife* **10**, e70977 (2021).

Methods

Zebrafish husbandry. This study was performed in accordance with the recommendations in the Guide for the Care and Use of Laboratory Animals of the National Institutes of Health. All of the animals were handled according to approved institutional animal care and use committee protocols (IA16-00788_AMEND202100320) of the NYU Grossman School of Medicine.

Zebrafish strains. Embryos were staged as previously described[50]. The *cxcl12a*^{at30516} allele has been previously described[51]. The *lamC1*^{sa9866} allele was obtained from the Zebrafish International Resource Center (https://zebrafish.org) and contains a nonsense mutation that results in a premature stop codon[52]. Homozygous *lamC1*^{sa9866} mutants were identified by their shortened body axis[7] or by PCR-based genotyping. Primers used for genotyping of *lamC1*^{sa9866} mutant fish are listed in Supplementary Table 1. The PCR product was digested with the restriction enzyme BsaI (New England Biolabs, R0535L) to yield a 168-bp fragment for the wild-type allele and a 120 bp fragment and a 48 bp fragment for the mutant allele. The *Tg(prim:mem-mCherry)* (ref. [53]), *Tg(cldnB:lyn$_2$GFP)* (ref. [35]), *hsp70:cxcl12a* (ref. [54]). *TgBAC(cdh1:cdh1-TagRFP)* (ref. [9]), *TgBAC(cxcr4b:cxcr4b-Kate2-IRES-EGFP-CaaX)p7* (ref.[41]) and *TgBAC(cxcr4b:zGrad)* (ref. [9]), *TgBAC(cdh1:cdh1-sfGFP exon16)* (ref. [11]), *TgBAC(cdh2:cdh2-mCherry exon16)* (ref. [11]), *Gt(ctnna1-citrine)Ct3a* (refs. [55,56]), *TgBAC(cxcr4b:h2a-mCherry)* (ref. [53]), *TgBAC(cxcr4b:cxcr4b-EGFP-IRES-Kate2-CaaX)p7* (ref. [41]), *cdh1:cdh1-tdTomato* (ref. [57]), *itgb1b:itgb1b-tdTomato* (ref. [58]) lines have been previously described.

Generation of mutant alleles. To generate *tln1*, *tln2a*, *tln2b*, *itgb1a* and *itgb1b* mutants, we followed previously described CRISPR–Cas9-based gene-editing protocols[59]. mRNA for Cas9 was synthesized by in vitro transcription with a mMESSAGE mMACHINE T7 Transcription kit (Thermo Fisher Scientific, AM1344) using the linearized plasmid *pST1374-NLS-flag-linker-Cas9* (Addgene, 44758)[60] as a template. Three to four guide RNAs (gRNAs) were designed to target the coding sequence around the start codons in the cases where the genes were fully annotated in the Ensembl genome browser (GRCz10, www.ensembl.org). Otherwise, we designed gRNAs targeting the available coding sequence in the Ensembl genome browser (GRCz10). gRNA sequences were identified using the CRISPR guide design offered by Benchling (https://www.benchling.com/crispr/). The templates for gRNAs were synthesized by PCR. In brief, a target-sequence-specific primer was designed that contained the T7 promoter sequence, the target sequence without the PAM site and an overhang for primer annealing. A primer that coded for the chimeric gRNA backbone was designed. All primers were purchased from Integrated DNA Technologies (https://www.idtdna.com). The target-sequence-specific primer and the chimeric gRNA backbone primer were annealed, filled-in by Taq polymerase and amplified by PCR. The PCR products were column-purified using a QIAquick PCR Purification kit (Qiagen, 28106) and subjected to in vitro transcription using a MEGAscript T7 Transcription kit (Thermo Fisher Scientific, AM1334) to obtain the gRNAs. Three to four gRNAs (final concentration of each gRNA was 200 ng µl^{-1}) were mixed with Cas9 mRNA (300 ng µl^{-1}), and 1 nl was injected into 1-cell-stage embryos. The injected embryos were raised to adulthood and out-crossed to wild-type adults. Embryos from these crosses were genotyped for potential mutations induced by gene editing to identify adults with germline mutations. Embryos from adults carrying germline mutations were raised and genotyped as adults by PCR and sequencing. Primers used are listed in Supplementary Table 1.

Generation and genotyping of the tln1^{d4} *mutant.* The gRNAs used to target *tln1* are listed in Supplementary Table 1. The isolated mutant fish harbour a 4-bp deletion in *tln1* exon 2 that results in a frame shift that introduces a premature stop codon. *tln1*^{d4} mutant embryos recapitulate the previously described *tln1* phenotype, such as partially penetrant cardiac oedema and embryonic lethality[61]. Note that *tln1*^{d4} mutant fish can be kept as homozygous adults in the presence of the BAC transgene *TgBAC(tln1:tln1-YPet)*, which rescues the lack of *tln1* activity. The *tln1*^{d4} allele was genotyped by amplifying the locus through PCR and digestion of the amplicon with the restriction enzyme Sau3AI (New England Biolabs, R0169L). The digest yields a 122-bp fragment and a 53-bp fragment for the *tln1* wild-type allele and a 171-bp fragment for the *tln1*^{d4} allele. The primers used for genotyping by PCR are listed in Supplementary Table 1.

Note that the copy number of the *tln1* wild-type and the *tln1*^{d4} alleles with *TgBAC(tln1:tln1-YPet)* can be determined by the intensity of the bands of the digested amplicons on a 3% agarose gel with the above genotyping protocol.

Generation and genotyping of the tln2a^{i23} *mutant.* The gRNAs used to target *tln2a* are listed in Supplementary Table 1. The isolated *tln2a* mutant line comprises a 23-bp insertion (1-bp deletion plus 24-bp insertion) in *tln2a* exon 3 that results in a frame shift that causes a premature stop codon. We were not able to obtain *tln2a*^{i23} homozygous adult fish in Mendelian ratios, which suggests that *tln2a*^{i23} homozygous mutant fish die at some point between 5 d.p.f. and 60 d.p.f. However, we occasionally recovered *tln2a*^{i23} homozygous adult fish. The *tln2a*^{i23} allele was genotyped by PCR followed by SrfI restriction digest (New England Biolabs, R0629L). The primers used for genotyping by PCR are listed in Supplementary Table 1. Note that the forward primer introduces a SrfI target site in the mutant allele only. Thus, SrfI restriction digest of the PCR amplicons results in a 192-bp fragment for the *tln2a* wild-type allele and a 37-bp fragment and a 155-bp fragment for *tln2a*^{i23} mutant allele.

Generation and genotyping of the tln2b^{d10} *mutant.* The gRNAs used to target *tln2b* are listed in Supplementary Table 1. The isolated mutant harbours a 10-bp deletion that results in a frame shift that causes a premature stop codon. The predicted Tln2b^{d10} mutant protein comprises only the first 658 amino acids of the total 2,580 amino acids. Note that *tln2b*^{d10} mutants can be kept as homozygous adult fish. The *tln2b*^{d10} allele was genotyped by PCR. The primers used for genotyping by PCR are listed in Supplementary Table 1.

Generation and genotyping of the itgb1a^{d34} *mutant.* The gRNAs used to target *itgb1a* are listed in Supplementary Table 1. The isolated mutant contains a 34-bp deletion in *itgb1a* exon 3 that results in a frame shift that causes a premature stop codon. *itgb1a*^{d34} mutants can be kept as homozygous adult fish. The *itgb1a*^{d34} allele was genotyped by PCR. The primers used for genotyping by PCR are listed in Supplementary Table 1.

Generation and genotyping of the itgb1b^{i70} *mutant.* The gRNAs used to target *itgb1b* are listed in Supplementary Table 1. The isolated mutant contains a 70-bp insertion that results in a frame shift that introduces two successive premature stop codons. The predicted mutant protein comprises only the first 320 amino acids of the total 806 amino acids. *itgb1b*^{i70} homozygous mutant embryos display a shorter body axis (Extended Data Fig. 5b–d) and die as embryos, which is consistent with previous reports[62]. The *itgb1b*^{i70} allele was genotyped by PCR. The primers used for genotyping by PCR are listed in Supplementary Table 1.

Generation of transgenic lines. To generate BAC-mediated transgenes, we modified the BAC clone of interest with galK-mediated BAC recombineering as previously described[63,64]. In brief, we first modified the BAC clone of interest to include a transgensis marker and the *tol2* sequences in the BAC backbone. Next, we modified the protein-coding sequence of interest on the BAC to add a fluorescent protein or to express the coding sequence under the regulation of a specific promoter. The final BAC was characterized by EcoRI digestion and PCR followed by sequencing around the modified sequences. The final BAC was purified with a Nucleobond BAC 100 kit (Takara Bio, 740579) and co-injected with 1 nl of 40 ng µl^{-1} *tol2* mRNA into 1-cell-stage embryos. The stable transgenic line was established by out-crossing the adult fish injected with the BAC transgene and raising transgenic embryos.

TgBAC(lamC1:lamC1-sfGFP). For the *lamC1:lamC1-sfGFP* transgene, we used the BAC clone CHORI-211-194I4, which was obtained from BACPAC Resources, Children's Hospital Oakland Research Institute, CA, USA. This BAC spans 192,491 bp of genomic DNA and contains the *lamC1* locus with about 50 kbp of the genomic sequence upstream of *lamC1* exon 1 and about 35 kbp of the genomic sequence downstream of *lamC1* exon 28. The transgenesis marker is *cryaa:Cerulean*. This transgene expresses full-length laminin-γ1 fused to sfGFP from the *lamC1* promoter. The full name of this transgenic line is *TgBAC(lamC1:lamC1-sfGFP)p1*. Note that this transgene recapitulates the previously reported expression pattern of *lamC1* mRNA expression[65], partially rescues *lamC1* homozygous mutant embryos (Extended Data Fig. 1h) and does not affect primordium migration (Extended Data Fig. 1i).

TgBAC(tln1:tln1-YPet). For the *tln1:tln1-YPet* transgene, we used the BAC clone DKEY-42J10, which was obtained from ImaGenes. The BAC clone spans 194,108 bp of genomic DNA. This includes 40 kb of the genomic sequence upstream of the beginning of *tln1* exon 1, *tln1* exons 1 to 44, but lacks *tln1* exons 45 to 56. To include the complete coding sequence of *tln1* on the BAC, we inserted the sequence of the missing *tln1* exons (exons 45 to 56) directly downstream of exon 44. This design was guided by the annotated *tln1* transcript *tln1-202* (ENSDART00000166799.2, Ensembl). We inserted the coding sequence for *YPet* between the head and the rod domains of *tln1* (ref. [66]), which is located in *tln1* exon 13. As a transgenesis marker, we inserted *cryaa:dsRed* in the BAC backbone. A cassette comprising *tln1* exons 45–56 and the kanamycin-resistant gene *KanR* was inserted. The amino acid sequence around the YPet insertion is Gly-Ser-Val-X-Ala-Leu-Pro, where YPet and restriction enzyme sequences were inserted in frame at position X. The full name of this transgenic line is *TgBAC(tln1:tln1-YPet)p2*. Note that the expression pattern of this transgene recapitulates the in situ hybridization pattern against *tln1* mRNA (Extended Data Fig. 3d,f). This transgene rescued the lethality of *tln1* homozygous mutant embryos.

TgBAC(cxcr4b:F-tractin-mCherry). For the *cxcr4b:F-tractin-mCherry* transgene, we used the BAC clone DKEY-169F10, which was obtained from ImaGenes. The BAC clone DKEY-169F10 contains a 60 kb genomic DNA fragment that spans the entire *cxcr4b* locus. As a transgenesis marker, we used *myl7:mScarlet*. The sequence of *F-tractin* (rat inositol 1,4,5-triphosphate 3-kinase A (ITPKA) amino acids 10–52)[67] together with a linker sequence (GLALPVAT) was used. The full name of this transgenic line is *TgBAC(cxcr4b:F-tractin-mCherry)p3*.

TgBAC(cxcr4b:F-tractin-mNeonGreen). The BAC construct *cxcr4b:F-tractin-mNeonGreen* was generated as described above for the *cxcr4b:F-tractin-mCherry* line except that the BAC was modified to contain the *mNeonGreen* (mNG) instead of the *mCherry* coding sequence. The *mNG* coding sequence was PCR amplified from Addgene plasmid 98886 (ref. [68]).

TgBAC(cxcr4b:myl12.1-mScarlet). For the *cxcr4b:myl12.1-mScarlet* transgene, we used the DKEY-169F10 BAC clone described above. The transgenesis marker is *myl7:mScarlet*. The *myl12.1* coding sequence was amplified from zebrafish cDNA by PCR. This transgene expresses the first five amino acids from *cxcr4b* exon 1 fused to Myl12.1–mScarlet from the *cxcr4b* promoter. The full name of this transgenic line is *TgBAC(cxcr4b:myl12.1-mScarlet)p2*.

TgBAC(cxcr4b:EGFP-CaaX). For construction of *cxcr4b:EGFP-CaaX* BAC clone, we used the BAC clone DKEY-169F10 with the transgenesis marker *myl7:mScarlet* described above. This transgene expresses the first five amino acids from *cxcr4b* exon 1 fused to EGFP–CaaX from the *cxcr4b* promoter. The full name of this transgenic line is *TgBAC(cxcr4b:EGFP-CaaX)p1*.

Generation of knock-in strains. *itgb1b:itgb1b-sfGFP.* The *itgb1b:itgb1b-sfGFP* knock-in line was generated as previously described[58]. As a targeting cassette, we used the described targeting plasmid for *itgb1b:itgb1b-tdTomato* (ref. [58]) but swapped the *tdTomato* coding sequence with *sfGFP* coding sequence. Note that the expression pattern of *itgb1b:itgb1b-sfGFP* recapitulates the pattern seen by in situ hybridization against *itgb1b* mRNA (Extended Data Fig. 3a,c). *itgb1b:itgb1b-sfGFP* homozygous and *itgb1b:itgb1b-sfGFP/itgb1b*^{i70} trans-heterozygous fish are adult viable.

itgb1b:itgb1b$^{\Delta NPxY}$*-sfGFP.* The *itgb1b:itgb1b*$^{\Delta NPxY}$*-sfGFP* knock-in line was generated as described above for the *itgb1b:itgb1b-sfGFP* line except that the sequence coding for the first to the second NPxY motif (NPIYKSAVTTVVNPKY, amino acids 777–792) was deleted in the plasmid that contained the targeting cassette. We identified one *itgb1b:itgb1b*$^{\Delta NPxY}$*-sfGFP* line and confirmed the correct knock-in event by sequencing PCR amplicons spanning the genomic insertion site.

Generation of plasmid constructs. Plasmids were generated by Gibson cloning[69]. To construct *pDEST-tol2-acta1a-cxcl12a-t2a-mCherry* and *pDEST-tol2-acta1a-mCherry* plasmids, the following plasmids were used as PCR templates: the plasmid backbone including the *tol2* sites, the *acta1a* promoter and the *cxcl12a* coding sequence were amplified from *pDestTol2pA2* (ref. [70]), *pDEST-tol2-acta1a-GFP* (ref. [71]) and *pCS2-cxcl12a* (ref. [72]), respectively. To construct *pCS2(+)-YPet-ZF1*, *pCS2(+)-mNeonGreen-ZF1* and *pCS2(+)-mCherry-ZF1*, the following plasmids were used as templates: the plasmid backbone, the *YPet*, the *mNeonGreen* and *mCherry* sequences were amplified from *pCS2(+)-sfGFP-ZF1* (ref. [9]) or *pCS2(+)*, *pUC19-tln1-5arm-YPet-3arm*, the Addgene plasmid 98886 (ref. [68]) and *pDEST-tol2-hsp70l-secP-mCherry-SV40pA* (ref. [53]), respectively. To construct *pDEST-tol2-hsp70l-zGrad-t2a-mNeonGreen*, the following plasmids were used as PCR templates: the plasmid backbone including *tol2* sites, the *hsp70l* promoter and the *zGrad* coding sequence were amplified from *pDEST-tol2-hsp70l-zGrad* (ref. [9]) and the *t2a-mNeonGreen* sequence was amplified from the Addgene plasmid 98886 (ref. [68]) with PCR primers that also included the *t2a* sequence. The *pCS2(+)-lyn$_2$mCherry* plasmid was generated based on the *pCS2(+)-lyn$_2$ EGFP* plasmid (gift from R. W. Köster)[73].

In vitro mRNA transcription and mRNA injection. Linear templates for in vitro mRNA transcription were generated by restriction digest of plasmids or PCR on plasmids using primers containing a SP6 promoter sequence. mRNAs were transcribed using a mMESSAGE mMACHINE SP6 Transcription kit (Thermo Fisher Scientific, AM1340). Injection mixes contained 50 ng µl^{-1} mRNAs with 0.1% phenol red solution (Life Technologies, 15100-043). A total of 1 nl of the injection mix was injected in 1-cell-stage embryos. *tol2* mRNA was synthesized from a linearized *pCS2FA-transposase* plasmid[70].

Embryo dissociation and primary zebrafish cell culture. Glass-bottom dishes (MatTek, P35G-0-20-C) were coated with mouse laminin protein (Corning, 354232). In brief, 50 µg of mouse laminin was mixed with Leibovitz L15 medium without phenol red (Fisher, 21083027) and added to the glass-bottom dishes. The dishes were incubated for 1 h at room temperature and then washed with PBS (137 mM NaCl, 2.7 mM KCl, 10 mM Na_2HPO_4 and 1.8 mM KH_2PO_4). Embryos (33 h.p.f.) were manually dechorionated and the tails were dissected off in fish water (60 µg ml^{-1} of Instant Ocean Sea Salts(Instant Ocean, SS15-10)) supplemented with 0.4 mg ml^{-1} MS-222 anaesthetic (Sigma, A5040-25g). The tails were collected and transferred into a cell-dissociation medium (0.05% Trypsin-EDTA (Invitrogen, 25200-056)). The tails were then incubated in the dissociation medium at 28° C for 20–30 min, pipetted up and down with a P1000 pipette tip every 5 min until the tails were dissociated into single cells. This cell suspension was filtered through a 70-µm nylon mesh (Fisher, 22-363-548). After three to four washes with PBS, cells were resuspended in cell culture medium (Leibovitz L-15 medium without phenol red (Fisher, 21083027), 15% FBS (Fisher Scientific, A3160601) and 100 U ml^{-1} penicillin–streptomycin (Invitrogen, 15140-122)). The cell suspension was added to the laminin-coated dishes and incubated at 28° C overnight to allow the cells to settle.

Immunofluorescence staining of cultured cells. Dissociated embryonic zebrafish cells seeded on laminin-coated dishes were washed with PBS and fixed with 4% paraformaldehyde (PFA) in PBST at room temperature for 10 min. The cells were permeabilized with 0.5% Triton X-100 in PBS at room temperature for 10 min and blocked with 0.5% BSA (Millipore-Sigma, A4737-100G) in PBS at room temperature for 30 min, followed by incubation with the primary antibody overnight at room temperature. To detect Itgb1b–sfGFP and Tln1–YPet, we used a rabbit anti-GFP primary antibody (Torrey Pines Biolabs, TP401, lot no. 081211) at a dilution of 1:500 in 0.5% BSA/PBS. To detect F-tractin–mCherry, we used a sheep anti-mCherry primary antibody (custom-made antibody by Covance[53]) at a dilution of 1:1,000 in 0.5% BSA/PBS. The primary antibodies were detected with the following secondary antibodies at a 1:1,000 dilution at room temperature for 1 h: donkey anti-sheep-Cy3 (Jackson ImmunoResearch, 713-166-147, lot no. 106361) and donkey anti-rabbit-Alexa488 (Jackson ImmunoResearch, 711-546-152, lot no. 109010). The posterior lateral line cells were identified based on F-tractin–mCherry expression driven from the *cxcr4b* promoter. In the tails of 33 h.p.f. embryos, the *cxcr4b* promoter drives high expression only in the posterior lateral line[9,72]. Imaging was performed using a spinning disk confocal Nikon W1 equipped with an Apo ×60 NA 1.40 oil objective lens (Nikon, MRD01605). Images shown are maximum-projected *z*-stacks.

Antibody staining and quantification of paxillin and p-paxillin levels. To stain for F-actin, phospho-MLC, fibronectin, chondroitin sulfate, paxillin and p-paxillin (p-Y118) and the membrane of the primordium cells, we fixed 32 h.p.f. *TgBAC(cxcr4b:EGFP-CaaX)* embryos in 4% PFA/PBST for 2 h (F-actin, phospho-MLC, fibronectin, chondroitin sulfate, p-paxillin (p-Y118)) or overnight (paxillin) at room temperature. Embryos were dehydrated in 100% methanol (Millipore-Sigma, 322415-100ML) overnight at −20° C, rehydrated using a series of 50% and 30% methanol in PBST and blocked in 1% BSA/PBST for 1 h at room temperature. Embryos fixed overnight were permeabilized with proteinase K (10 µg ml^{-1} in PBST) (Sigma Aldrich, P6556) for 5 min at room temperature and re-fixed with 4% PFA/PBST for 20 min at room temperature before blocking. The embryos were incubated in rabbit anti-phospho-myosin light chain 2 (Ser19) (1:100, Cell Signaling Technology, 3671, lot no. 6), rabbit anti-fibronectin (1:100, Sigma, F3648, lot no. 0000090857), mouse anti-chondroitin sulfate (1:100, Sigma, MA1-83055, lot no. WI3245117), mouse anti-paxillin (1:100, BD Transductions, lot no. 1110894), or rabbit anti-paxillin(pTyr118) (1:500, Novusbio, NBP2-24459, lot no. 031327 42D(P)) together with goat anti-GFP (1:500, Covance, custom-made antibody[41]) overnight at 4° C. Embryos were washed four times with PBST and incubated with donkey anti-rabbit Cy3 (1:500, Jackson ImmunoResearch, 711-165-152, lot no. 102215) or goat anti-mouse Cy3 (1:500, Jackson ImmunoResearch, 115-165-003) together with donkey anti-goat Alexa488 (1:500, Jackson ImmunoResearch, 705-546-147, lot no. 110667) secondary antibodies in PBST. To stain for F-actin with phalloidin, embryos were fixed in 4% PFA overnight, permeabilized in 2% Triton X-100/PBS overnight at 4° C and blocked in 1% BSA/PBST for 1 h at room temperature. Subsequently, embryos were stained with AlexaFluor 594 phalloidin (1:100, Invitrogen, A12381, lot no. 2335606) in PBST overnight at 4° C. After four washes with PBST, embryos were imaged. Embryos were mounted in PBST. Images were taken on a Leica SP8 confocal microscope equipped with HyD detectors (Leica Microsystems) using a ×40 (NA 1.1) objective with a sequential scan setting.

Quantification of paxillin and p-paxillin intensities were performed in a semi-automated manner with a custom-written macro in Fiji. In brief, the primordium region was manually cropped. The macro generated a binary mask based on the EGFP–CaaX signal (autothresholding with the Iso-Data method). The mask was applied to the paxillin or p-paxillin channel, and the signal on the primordium membrane was extracted. Next, three consecutive optical *z*-slices without apical constrictions were manually selected and average-projected. A rectangular region of interest (ROI) 10-µm wide and 100-µm long was manually defined from the tip of the primordium, and the signal intensity profile was obtained along the front-to-rear axis of the primordium. We did not include the membrane at the leading edge of the primordium because the signal in this region could not be separated from the signal of the skin. Finally, the signal was normalized to the average intensity for each embryo and plotted.

Quantification of filamentous collagen IV by immunofluorescence staining. To stain for collagen IV and the membrane of the primordium cells in *lamC1* mutant and control embryos, we in-crossed *cldnB:lyn$_2$GFP; lamC1*$^{+/-}$ fish and sorted for *cldnB:lyn$_2$GFP; lamC1*$^{-/-}$ and *cldnB:lyn$_2$GFP; lamC1*$^{-/+}$ or *cldnB:lyn$_2$GFP; lamC1*$^{+/+}$ embryos at 30 h.p.f. One hour later, 31 h.p.f. embryos were fixed with 4% PFA/PBST for 2 h at room temperature then stored in 100% methanol (Millipore-Sigma, 322415-100ML) overnight at −20° C. Embryos were rehydrated using a series of 50% and 30% methanol in PBST and blocked in 1% BSA/PBST for 1 h at room temperature. The embryos were incubated in rabbit anti-collagen IV (1:200, ab6586, Abcam) and goat anti-GFP (1:500, Covance, custom-made antibody[41])

overnight at 4° C. Embryos were washed four times with PBST and incubated with donkey anti-rabbit Cy3 (1:500, Jackson ImmunoResearch, 711-165-152, lot no. 102215) and donkey anti-goat Alexa488 (1:500, Jackson ImmunoResearch, 705-546-147, lot no. 110667) secondary antibodies in PBST. Embryos were mounted in 0.5% low-melt agarose/Ringer's solution. Images were taken on a spinning disk confocal Nikon W1 microscope. The number of filament structures around the primordium was quantified using a custom-written macro in Fiji. In brief, a 150 × 150 µm ROI that contained the entire primordium was manually defined. The red fluorescent channel of the *z*-stack representing the collagen IV signal was sum-projected, and only the fluorescence values above 1.25 the mean fluorescence intensity of the image were kept. Filamentous structures were extracted using the Tubeness filter (https://www.longair.net/edinburgh/imagej/tubeness/) in Fiji with sigma set to 1.0. Then, the image was thresholded using "Otsu's" method and the number of filaments was counted with the Analyze Particles command in Fiji (settings: limiting size = 50–infinity, circularity = 0.0–0.3).

Whole-mount in situ hybridization. The procedures for RNA probe synthesis and zebrafish embryo whole-mount in situ hybridization were performed as previously described[74]. The RNA probe against *cxcl12a* has been previously described[72]. To synthesize the RNA probes against *tln1* and *tln2a*, parts of the transcripts were PCR-amplified from cDNA synthesized from zebrafish embryos using the primers indicated in Supplementary Table 1 and cloned into the *pCR2.1-TOPO* vector (Thermo Fisher Scientific, 451641). The plasmids were linearized using BamHI-HF (New England Biolabs, R3136L), column-purified (Qiagen, QIAquick PCR purification kit, 28106) and in vitro transcribed using a DIG RNA Labeling kit (Roche, 11277073910) together with a SP6/T7 Transcription kit (Roche, 10999644001). To synthesize the RNA probes against *tln2b*, *itgb1a*, *itgb1b*, *itgb1b.1*, *itgb1b.2*, *itgb2*, *itgb3a*, *itgb3b*, *itgb4*, *itgb5*, *itgb6* and *itgb7*, DNA templates were PCR-amplified from cDNA synthesized from maternal, 28 h.p.f. or 33 h.p.f. embryonic cDNA using the primers listed in Supplementary Table 1. The reverse primers harbour T7 promoter sequence at their a 5′ end so that the PCR products could directly be transcribed in vitro after column purification. The RNA probes were synthesized with Roche DIG labelling mix (Roche, 11277073910) and detected using an anti-DIG antibody coupled to alkaline phosphatase (1:5,000, Roche, 11093274910) and NBT/BCIP staining (Roche, 11681451001). Embryos were mounted on 3% methyl cellulose (Sigma Aldrich, M0512) and imaged on an Axioplan Microscope (Zeiss) equipped with an Axiocam (Zeiss) using a ×10 (NA 0.5) objective lens.

Dissection of embryos and collagenase treatment. The head and the yolk of 28 h.p.f. wild-type embryos were removed in fish water supplemented with 0.4 mg ml^{-1} MS-222 anaesthetic using forceps. Dissected embryos were transferred into deskin medium (Ca^{2+}-free Ringer's solution, 50 mM EDTA and 0.4 mg ml^{-1} MS-222 anaesthetic). The skin of the embryos was peeled off under a Leica dissection scope (Leica, Wild M420 with light stand) using forceps. The deskinned embryos were then transferred into Leibovitz L-15 medium (Fisher, 11415064) supplemented with 0.4 mg ml^{-1} MS-222 anaesthetic. The collagenase (collagenase, purified, 4 ku, Worthington, LS005275) stock was prepared in Leibovitz L-15 medium at a concentration of 1,000 U ml^{-1}. The deskinned embryos were soaked in the collagenase solution (909 U ml^{-1}) supplemented with 0.4 mg ml^{-1} MS-222 anaesthetic at room temperature for 30 min. After the treatment, the collagenase was washed out using Leibovitz L-15 medium supplemented with 0.4 mg ml^{-1} MS-222 anaesthetic, then the embryos were quickly mounted for AFM or confocal microscopy.

AFM measurements and data analysis. Deskinned embryos were glued to FluoroDish dishes (World Precision Instruments, FD5040-100) using CELL-TAK (Corning, 354240) and immersed in Leibovitz L-15 medium supplemented with 0.4 mg ml^{-1} of the anaesthetic MS-222 (Sigma Aldrich, A5040-25g). All AFM measurements were carried out within 90 min after skin removal. The AFM measurements were performed on an Asylum Research MFP-3D-BIO atomic force microscope using the Asylum Research software package v.IX (AR software) as previously described[75]. The AR software was used for cantilever calibration, force mapping, data export and data visualization (Extended Data Fig. 8j–n). We used a spherical borosilicate glass bead probe with a 2.5 µm radius, a spring constant of 0.07 N m^{-1}, a Young's modulus of 68.0 GPa and a Poisson ratio of 0.19 (Novascan, PT-GS). In contrast to pyramidal probes, which probe structures at the nanometre length scale such as extracellular filaments, spherical probes work at the micrometre length scale and assess the global properties of the BM[76]. We used a trigger point of 1 nN force and an indentation velocity of 5.0 µm s^{-1}. Such a slow indentation velocity minimizes viscous effects. Two to three two-dimensional 8 × 8 (20 × 20 µm) square grids were probed per deskinned embryo. The probed area was located above the muscles that overlie the notochord in the centre of the trunk of the deskinned embryo (Extended Data Fig. 8j).

The AFM measurements were analysed using the Rasylum package (https://github.com/nstone8/Rasylum), which runs on the R programming language software environment (https://www.r-project.org/). We modified the Rasylum package in three ways. First, we included a batch-mode option to analyse a set of force curves automatically. Second, we modified the extractStiffness function in the Rasylum package to specify the length of the force curve that will be fit to the Hertz model. The original extractStiffness function fits the entire force curve from the contact point to the maximum deformation point to the Hertz model. Our modification allows the user to only fit a select part of the curve to the Hertz model (from the contact point to a user-specified length of the deformation part of the force curve, in our case 200 nm and 500 nm). Third, we modified the extractStiffness function to report statistical parameters for the fit of the probe approach part of the force curve (beginning of force curve to contact point) to a linear model and the indentation part of the force curve to the Hertz model (contact point to end of force curve/point of maximum deformation or the end point defined by the user). These statistical parameters were used as quality control criteria to include or reject force curves. For the calculation of Young's modulus, the sample Poisson ratio was assumed to be 0.45. The reduced Young's modulus E^* was obtained by fitting the first 200 nm of the approach curve past the contact point to the Hertz model as follows:

$$F = \frac{4}{3} E^{\star} r^{\frac{1}{2}} \delta^{\frac{3}{2}},$$

where F is the loading force, E^* is the reduced Young's modulus, r is the radius of the spherical probe used and δ is the indentation. The sample Young's modulus E_s was calculated using

$$\frac{1}{E^{\star}} = \frac{1-\nu_i^2}{E_i} + \frac{1-\nu_s^2}{E_s},$$

where ν_i is the indenter's Poisson ratio, ν_s is the sample Poisson ratio and E_i is the indenter's Young's modulus.

Owing to debris after skin removal and the curvature of the BM above the muscle, some force curves were of low quality. To automatically select high-quality force curves, we applied three criteria. The first criterion was the slope of the fit of the baseline of the approach curve (start of approach curve to contact point) to a linear equation. The second criterion was the residuals between the measured and fitted curve of the baseline of the approach curve to a linear equation. The third criterion was the P value of the fit of the approach curve to the Hertz model from the contact point to 200 nm or 500 nm into the sample. Only force curves with a baseline slope between −10 and +10 pN µm^{-1}, baseline sum-of-squared-residuals smaller than 0.1 nN^2 and P values smaller than 1.0×10^{-14} were included to determine the overall stiffness of the BM. These criteria select for force curves that have a flat baseline approach curve and a clearly defined contact point. Extended Data Fig. 8n shows representative force curves that meet and do not meet these criteria.

Electron microscopy. *lamC1*$^{-/-}$ embryos were generated by in-crossing *lamC1*$^{-/+}$ fish. Embryos (30 h.p.f.) were fixed in electron microscopy fixative containing 2% PFA, 2% glutaraldehyde in 0.1 M sodium cacodylate buffer at room temperature for 2 h and then overnight at 4° C. Fixed embryos were rinsed with 0.1 M sodium cacodylate buffer and post-fixed with 1% OsO_4 in 0.1 M cacodylate buffer, followed by block-staining with 1% uranyl acetate aqueous solution overnight at 4° C. The samples were rinsed with water, dehydrated in a graded series of ethanol, infiltrated with propylene oxide/Epon mixtures and finally embedded in EMbed812 (Electron Microscopy Sciences). Sections (70 nm) were cut and mounted on 200 copper mesh grids and stained with uranyl acetate and lead citrate. Imaging was performed on a Talos120C transmission electron microscope (Thermo Fisher Scientific) with a Gatan (4k × 4k) OneView Camera (Gatan). The primordium cells were pseudo-coloured using Adobe Illustrator 2020 (Adobe).

Ectopic expression of Cxcl12a from the trunk muscle cells. A total of 1 nl of 10 ng µl^{-1} *pDEST-tol2-acta1a-cxcl12a-t2a-mCherry* plasmid DNA or *pDEST-tol2-acta1a-mCherry* plasmid DNA was injected together with 40 ng µl^{-1} *tol2* mRNA into 1-cell-stage embryos obtained from the following crosses: *lamC1*$^{+/-}$; *cxcl12a*$^{-/-}$; *cldnB:lyn$_2$GFP* in-cross, *lamC1*$^{+/+}$; *cxcl12a*$^{-/-}$; *cldnB:lyn$_2$GFP* in-cross, wild-type in-cross and *lamC1*$^{+/-}$; *cxcl12a*$^{-/-}$; *cxcr4b:cxcr4b-Kate2-IRES-GFP-CaaX* in-cross. *lamC1*$^{-/-}$ mutant embryos were identified by morphology.

Live imaging with a Leica SP8 confocal system and image analysis. The live imaging experiments detailed below were performed on a Leica SP8 confocal microscope system equipped with a ×40 (NA 1.1), a ×20 (NA 0.7) and a ×20 (NA 0.5) objectives. Samples were kept at 28 °C with a heated stage (Warner Instruments, Quick Exchange Heated Base, QE-1) for prolonged time-lapse imaging. The power of the laser lines was calibrated using a power meter (X-Cite Power Meter Model, Lumen Dynamics, XR2100). For quantifying the fluorescence intensity, image acquisition was carried out using the photon-counting mode. Embryos were mounted in 0.5% low-melt agarose (National Diagnostics, EC-205)/Ringer's solution supplemented with 0.4 mg ml^{-1} MS-222 anaesthetic on a coverslip or a plastic dish.

itgb1b mutant and control embryos were generated by crossing *itgb1b:itgb1b-sfGFP*$^{-/-}$; *prim:mem-mCherry* fish to *itgb1b:itgb1b-sfGFP*$^{-/-}$ fish. Such embryos were imaged for 10 h with the following settings: *z*-step size of 5.0 µm, time interval of 30 min and duration of 9.5 h. Mutants were identified by

the absence of Itgb1b–sfGFP expression. Note that *itgb1b* mutants produced by this cross showed a slightly stronger overall morphological defect than mutants generated by in-crossing *itgb1b*$^{-/+}$ fish, which indicated that maternal Itgb1b rescues the lack of zygotic Itgb1b slightly better than maternal Itgb1b–sfGFP mRNA and protein.

To image the localization of Itgb1b$^{\Delta NPxY}$–sfGFP in the primordium cells, 34 h.p.f. *itgb1b:itgb1b*$^{\Delta NPxY}$*-sfGFP*; *prim:mem-mCherry* and *itgb1b:itgb1b-sfGFP*; *prim:mem-mCherry* control embryos were mounted. The *z*-step size was 0.42 µm. The power of the 488-nm and 594-nm laser lines was calibrated to 95 µW and 29 µW, respectively. The GFP-to-mCherry fluorescence intensity ratio in the basal-to-apical axis was obtained by a custom-written macro in Fiji. In brief, the macro generated a cell-membrane mask based on the mCherry channel using the "Default" thresholding method in Fiji. This mask was applied to the GFP and the mCherry channels, and the signal intensities were obtained for each *z*-slice. To analyse the intensity profile of Itgb1b–sfGFP in the primordium cells along the front-to-back axis, we semi-automatically quantified the signal intensity of Itgb1b–sfGFP in the membrane of the primordium cells using custom-written macros in Fiji. In brief, we first manually aligned the primordium along the *x*, *y* and *z* axes such that the three central slices in the *z*-stack (= 1.2 µm) neither contained the apical constrictions nor the lateral line nerve but contained the tip and the rear of the primordium. Next, the macro generated a binary mask for the cell membrane using mem-mCherry fluorescence and the "Default" thresholding method in Fiji. The mask was applied to the GFP channel and the three central slices were average-projected. Next, the masked GFP channel was resliced from the tip of the primordium and the *z*-profile was obtained and plotted.

To image the localization of F-tractin–mCherry in the primordium cells with skin cells labelled with Cdh1–sfGFP, 33 h.p.f. *TgBAC(cxcr4b:F-tractin-mCherry)*; *TgBAC(cdh1:cdh1-sfGFP)* embryos were mounted. The *z*-step size was 0.42 µm. The power of the 488 nm and 594 nm laser lines were calibrated to 68 µW and 14 µW, respectively. The two channels were sequentially scanned.

To analyse the ratio of Itgb1b–tdTomato/Itgb1b–sfGFP and Itgb1b–tdTomato/ Itgb1b$^{\Delta NPxY}$–sfGFP fluorescence intensities, *itgb1b:itgb1b-sfGFP; itgb1b:itgb1b-tdTomato* and *itgb1b:itgb1b*$^{\Delta NPxY}$*-sfGFP; itgb1b:itgb1b-tdTomato* embryos were mounted at 32 h.p.f. The *z*-step size was 0.76 µm and the pinhole set to 2.0 Airy units. The power of the 488-nm and 546-nm laser lines was calibrated to 38 µW and 30 µW, respectively. Two channels were sequentially scanned. The ratio analysis was carried out in a semi-automated manner with a custom-written macro in Fiji. In brief, the red channel was divided by the green channel to generate the ratio image. The membrane mask was generated as follows. The red channel and the green channels were added to generate a single channel image, then this single channel image was thresholded with the "Moments" method in Fiji and was binarized to generate a mask image. The mask was then applied to the ratio image. The middle slice without the apical constrictions or lateral line nerve was manually defined. A line with a width of 30 pixels (= 8.52 µm) was drawn from the tip of the primordium to the rear, and the intensity profile along this line was obtained. To analyse the ratio in the myotendinous junctions and lateral sides of the muscle cells, we used the ratio image described above. The single slice at the bottom of the primordium in the *z*-stack was manually chosen. The mean ratio at myotendinous junctions was quantified by drawing a line with a width of 10 pixels (= 2.84 µm). The mean ratio at the lateral sides of the muscle cells was quantified by manually encircling the muscle cells between two myotendinous junctions.

To image the localization of Cdh2–mCherry in the primordium cells, 32 h.p.f. *TgBAC(cxcr4b:EGFP-CaaX)*; *TgBAC(cdh2:cdh2-mCherry)* embryos were mounted. The *z*-step size was set to 1.0 µm with a pinhole of 2.0 Airy units. The power of the 488-nm and 561-nm laser lines was calibrated to 27 µW and 1.52 mW, respectively. The two channels were sequentially scanned. The localization of Cdh2–mCherry in the primordium cells was obtained by extracting the fluorescence signal of Cdh2–mCherry only on the membrane of the primordium cells using a binary mask generated based on the EGFP–CaaX fluorescence signal and using the "Default" thresholding method in Fiji.

To assess the chemokine Cxcl12a signalling gradient across the primordium, *TgBAC(cxcr4b:cxcr4b-EGFP-IRES-Kate2-CaaX)p7* embryos were mounted. The *z*-step size was set to 0.7 µm with a pinhole of 2.0 Airy units. The power of the 488-nm and 594-nm laser lines was calibrated to 30 µW and 64 µW, respectively. The ratio of mem-Kate2 to Cxcr4b–EGFP was analysed with a previously published custom-written ImageJ macro[77].

To observe LamC1–sfGFP localization in the apical side of the primordium, *TgBAC(lamC1:lamC1-sfGFP);cdh1:cdh1-tdTomato*$^{/+}$ embryos at 32 h.p.f. were mounted. The *z*-step size was set to 0.42 µm with a pinhole of 1.0 Airy units. The power of the 488-nm and 546-nm laser lines was calibrated to 136 µW and 108 µW, respectively. The two channels were sequentially scanned.

To obtain embryos for long-term live imaging (7 h) of primordium migration in *tln1*$^{-/-}$; *tln2a*$^{+/+}$ or *tln2a*$^{+/-}$; *tln2b*$^{-/-}$; *TgBAC(cxcr4b:zGrad)*$^{/+}$; *prim:mem-mChery* embryos and control *prim:mem-mCherry*; *TgBAC(cxcr4b:zGrad)*$^{/+}$ embryos, we crossed *tln1*$^{-/-}$; *tln2a*$^{+/-}$; *tln2b*$^{+/-}$; *TgBAC(tln1:tln1-YPet)*$^{/+}$; *TgBAC(cxcr4b:zGrad)*$^{/+}$; *prim:mem-mCherry* male fish to *tln1*$^{-/-}$; *tln2a*$^{+/-}$; *tln2b*$^{-/-}$; *TgBAC(tln1:tln1-YPet)*$^{/+}$; *prim:mem-mCherry* female fish. The control embryos were obtained by crossing *prim:mem-mCherry* fish to *TgBAC(cxcr4b:zGrad)*$^{/+}$ fish. *tln1*$^{-/-}$ mutants were identified by the absence of Tln1–YPet expression at 28 h.p.f. Mutant embryos and control embryos were mounted in the same dish. The following settings were used: *z*-step size of 6.0 µm, time interval of 20 min and duration of 8 h. Imaged embryos were digested and genotyped for the *TgBAC(cxcr4b:zGrad)* transgene, *tln2a* and *tln2b*.

To quantify zGrad-mediated Tln1–YPet, Itgb1b–sfGFP and Ctnna1–Citrine degradation with zGrad expressed from the *cxcr4b* promoter, *TgBAC(tln1:tln1-YPet)*$^{/+}$; *prim:mem-mCherry* embryos and *TgBAC(tln1:tln1-YPet)*$^{/+}$; *prim:mem-mCherry; TgBAC(cxcr4b:zGrad)*$^{/+}$ embryos, *itgb1b:itgb1b-sfGFP*$^{/+}$; *prim:mem-mCherry* embryos and *itgb1b:itgb1b-sfGFP*$^{/+}$; *prim:mem-mCherry; TgBAC(cxcr4b:zGrad)*$^{/+}$ embryos, *ctnna1-citrine*$^{/+}$; *prim:mem-mCherry* embryos and *ctnna1-citrine*$^{/+}$; *prim:mem-mCherry; TgBAC(cxcr4b:zGrad)*$^{/+}$ embryos were sorted at 29 h.p.f. Five to six embryos of each genotype were mounted at 33–34 h.p.f. The laser power was calibrated to 45 µW (for Itgb1b–sfGFP) and 90 µW (Tln1–YPet and Ctnna1–Citrine) for the 488-nm laser line and 10 µW for the 594-nm laser line. The *z*-step size was set to 0.76 µm. To quantify the signal intensity of Tln1–YPet, Itgb1b–sfGFP and Ctnna1–Citrine in the primordium, we used a custom-written ImageJ macro. In brief, a binary mask for the primordium was generated using mem-mCherry fluorescence signal and the "Default" thresholding method followed by the "Filling holes" function. The binary mask was applied to the *z*-stack images and images were sum-projected. The fluorescence signal was obtained only in the masked area. To remove the contribution of autofluorescence from the embryo, we imaged three *prim:mem-mCherry* embryos with the same setting above and quantified the autofluorescence signal intensity with the same macro. The mean autofluorescence signal intensity from three embryos was subtracted from the experimental data.

To observe the localization of Myl12.1–mScarlet in the primordium cells, *TgBAC(cxcr4b:myl12.1-mScarlet); TgBAC(cxcr4b:EGFP-CaaX)* embryos were mounted at 32 h.p.f. The *z*-step size was 0.42 µm with a pinhole of 1.0 Airy units. The power of the 488-nm and 546-nm laser lines were calibrated to 105 µW and 112 µW, respectively. The two channels were sequentially scanned. Basally localized Myl12.1–mScarlet was analysed with a custom-written macro in Fiji. In brief, we first aligned the primordium with the *x*, *y* and *z* axes. The macro includes only the bottom half of the *z*-stack such that the stack did not contain the apical constrictions. Then, the stack was maximum-projected. The primordium area was masked by a binary mask generated as follows: the EGFP–CaaX channel was maximum-projected, thresholded using the "Huang" method in Fiji and the holes were filled. Then, 1.7 µm was eroded to eliminate the Myl12.1–mScarlet signal localized at the periphery of the primordium. The value (mean + s.d.) of Myl12.1–mScarlet was subtracted from the Myl12.1–mScarlet intensity to highlight only accumulated myosin II punctae. The total intensity of Myl12.1–mScarlet punctae in the front, middle and rear regions of the primordium was manually obtained. The total intensity of Myl12.1–mScarlet punctae was normalized by the area of the front, middle and rear of the primordium. Finally, these values were divided by the mean for normalization and plotted.

To quantify the migration speed of Ctnna1-depleted primordium cells, five *ctnna1:ctnna1-citrine*/*ctnna1:ctnna1-citrine*; *TgBAC(cxcr4b:zGrad)*$^{/+}$; *TgBAC(cxcr4b:H2A-mCherry)* embryos and five *ctnna1:ctnna1-citrine*/*ctnna1:ctnna1-citrine*; *TgBAC(cxcr4b:H2A-mCherry)* control embryos were mounted. Images were acquired every 2 min for a duration of 30–200 min. The pinhole was set to 1 Airy unit.

To track the cell nuclei in the primordium, we imported the time-lapse videos into the software Imaris v.8.0 (Bitplane, Oxford Instruments). As in the original recordings, the dimensions were set to $x = 0.378$ µm, $y = 0.378$ µm, $z = 1.00$ µm and $t = 120$ s. To track the cell nuclei, the "Spot" tool in the Imaris software was used with a specified cell diameter of 3.78 µm and the default background subtraction was activated. The histogram of the spot quality was adjusted such that about 70–80% of the cells were selected. The cell nuclei were tracked using the "Autoregressive motion" method with a maximum distance that an object can move between two consecutive time points set to 20 µm for the red channel (H2A–mCherry). The maximum gap size—the maximum number of consecutive time points that are allowed to be missing to join track fragments—was set to two. After running the tracking algorithm, the filter for the track length was set to select 75–85% of the longest tracks, and the tracks were manually curated to remove tracked nuclei that do not belong to the primordium or represent dying cells and to delete or correct track segments. For dividing cells, only one daughter cell was tracked. To correct for stage-drift, a muscle cell nucleus was tracked and chosen as a reference point. The *x*, *y*, *z* and *t* values and the track IDs were exported and the position of the reference cells was subtracted from all tracked cells at each time point. With the exported data, the speed of each cell in the indicated genotype was pooled.

To observe receptor internalization induced by ectopic Cxcl12a secreted from the muscle cells, 25–26 h.p.f. embryos were imaged. The power of the 488-nm and 561-nm laser lines was calibrated to 152 µW and 110 µW, respectively. The *z*-step size was set to 2.0 µm. We manually cropped the *z*-stack such that it only contained the primordium. We then generated a binary mask based on the GFP channel and applied it to the RFP and GFP channels. The GFP and RFP channels were then sum-projected, the mean intensity of each channel was measured and the RFP mean intensity was divided by the GFP mean intensity using a custom-written macro in Fiji.

The tagged protein expression patterns of *TgBAC(lamC1:lamC1-sfGFP)*, *TgBAC(tln1:tln1-YPet)*, *itgb1b:itgb1b-sfGFP* and *itgb1b:itgb1b*$^{\Delta NPxY}$*-sfGFP* were imaged in 28 h.p.f. embryos. The *z*-step size was set to 1.5 µm. The images were stitched together using the auto-tiling feature in the LAS X Life Science microscope software (Leica) and sum-projected.

Live imaging with a Nikon W1 spinning disk confocal system and image analysis. The live imaging experiments detailed below were performed using a Nikon W1 spinning disk confocal microscope that was equipped with an Apo LWD ×40 NA 1.15 objective lens (Nikon, MRD77410) and a SR HP Plan Apo ×100 NA 1.45 objective lens (Nikon, MRD01905). The ×100 objective was used only for the actin flow experiments. All other experiments were performed using the ×40 objective. The samples for live time-lapse imaging experiments were kept at 30° C using a Tokai Hit incubation system STXG-TIZWX-SET. The embryos were mounted in 0.5% low-melt agarose (National Diagnostics, EC-205)/Ringer's solution supplemented with 0.4 mg ml^{-1} MS-222 anaesthetic on a glass-bottom dish.

All FRAP experiments were performed using 32–34 h.p.f. embryos. For the analysis of Itgb1b–sfGFP at the myotendinous junction, embryos were treated with 50 µM Rockout (Rho kinase inhibitor III, MilliporeSigma, 555553-10MG) in 1% dimethylsulfoxide (DMSO) or control-treated with 1% DMSO for 3 h. A circular ROI with a 3-µm radius was selected and bleached with a 405-nm laser. Images with a fixed *z*-position were taken every 0.5 s for 30 s or 1 min. Two ROIs per embryo were recorded. For simultaneous FRAP of LamC1–sfGFP and sec–mCherry, 24 h.p.f. *lamC1:lamC1-sfGFP*; *hsp70l:sec-mCherry* embryos were heat-shocked at 39.5° C for 1 h to induce sec–mCherry expression from the heat shock promoter. To bleach LamC1–sfGFP and sec–mCherry, a circular ROI with a 6-µm radius was selected and bleached with a 405-nm laser. Images with a fixed *z*-position were taken every 100 ms for 30 s. For long-term LamC1–sfGFP FRAP, 3–6 circular ROIs with a 6-µm radius per embryo were selected and bleached with a 405-nm laser. *Z*-stack images were taken every 10 min for 50 min. All FRAP analyses were performed using the mean intensity values of the ROIs extracted by the time-measurement setting in NIS-Elements (Nikon) except for the long-term LamC1–sfGFP FRAP. For the long-term LamC1–sfGFP FRAP, we first sum-projected the *z*-stacks and corrected for photobleaching using the mean fluorescence intensity of the image for each time point. The circular ROIs with a 6-µm radius were manually selected and tracked over time. The mean intensity in the ROIs was then measured and plotted. For all other FRAP analyses, we first normalized the fluorescence intensity of the bleached region at each time point I_x to the difference between the fluorescence intensity before bleaching (I_{max}) and the minimal fluorescence intensity after bleaching (I_{min}) using the following relation

$$I = \frac{I_x - I_{min}}{I_{max} - I_{min}},$$

where I is the normalized fluorescence intensity. We then corrected for overall photobleaching by dividing the normalized fluorescence intensity I by the overall rate of photobleaching. To calculate the overall rate of photobleaching, we randomly picked a 30 × 30 µm region outside the bleached region and extracted the mean intensity over time from four movies for each experimental setting and averaged them. The overall photobleaching rate was calculated by dividing the average intensity of each time point by the average intensity of the first time point.

To locally photobleach LamC1–sfGFP, the ROIs for bleaching were defined by a custom-written macro in Fiji and saved as a binary tiff image with 1,024 × 1,024-pixel resolution. The tiff image was imported into the Nikon NIS-Elements AR software as a ROI for the photobleaching experiments. The Fiji macro creates a hexagonal pattern with 20 × 20 dots (= 120 × 120 µm), each of which is separated from its neighbouring dots by 6 µm. A single dot was 2 pixels wide (= 0.65 µm). Bleaching was performed with a 473-nm laser in a single plane.

Short-term live imaging (1 h) of the migration of the primordium in *itgb1b*$^{-/-}$*; cldnB:lyn*$_2$*GFP* embryos and control embryos was performed using 32 h.p.f. embryos. *itgb1b*$^{-/-}$ embryos and control (sibling) embryos were sorted according to their body length before mounting. Images with a 40-µm *z*-stack with a step size of 0.8 µm were taken every 5 min for 1 h with a multi-position setting. Imaged embryos were digested and genotyped for *itgb1b* as described above.

To image the deformation of the BM by skin basal cells, 32 h.p.f. *TgBAC(lamC1:lamC1-sfGFP)* embryos injected with *lyn*$_2$*-mCherry* mRNA at the 1-cell stage were mounted at 32 h.p.f. First, the LamC1–sfGFP-labelled BM was photobleached to generate a hexagonal dot pattern. Second, the location of the bleach pattern was imaged with the following parameters: *z*-step size of 0.4 µm, time interval of 1 min and duration of 10 min.

To image the deformation of the BM by the primordium, 32 h.p.f. *TgBAC(lamC1:lamC1-sfGFP); prim:mem-mCherry* embryos, *TgBAC(lamC1:lamC1-sfGFP); prim:mem-mCherry; hsp70l:cxcl12a* control embryos and *TgBAC(lamC1:lamC1-sfGFP); prim:mem-mCherry; itgb1b*$^{-/-}$ were mounted. First, the LamC1–sfGFP-labelled BM was photobleached to generate a hexagonal dot pattern. Second, the location of the bleach pattern was imaged with the following parameters: *z*-step size of 0.4 µm, time interval of 5 min and duration of 120 min. The multi-position setting was used to image multiple embryos at the same time and in the same dish. The *TgBAC(lamC1:lamC1-sfGFP); prim:mem-mCherry; hsp70l:cxcl12a* control embryos were heat-shocked at 39.5° C for 1 h at 28 h.p.f. to induce Cxcl12a expression and to block primordium migration before imaging. The genotype of *itgb1b*$^{-/-}$ embryos was confirmed by PCR after live imaging.

To image the accumulation of LamC1–sfGFP under the primordium, 32 h.p.f. *TgBAC(lamC1:lamC1-sfGFP); TgBAC(cxcr4b:F-tractin-mCherry)* embryos were mounted. The green and the red channels were sequentially imaged to prevent fluorescence bleed-through. To quantify the LamC1–sfGFP intensity around the edge of the primordium and beyond the primordium, we used a semi-automated custom-written macro in Fiji. *Z*-stacks were maximum-projected. The outer circumference of the primordium was manually traced using the primordium-specific mCherry signal as a guide. The encircled area was filled and thresholded. The thresholded image was duplicated. The first duplicate was 5 times eroded from its outline inward (= 1.625 µm). The second duplicate was dilated five times from its outline outward. Then the two images were subtracted from each other. This generated a 10 pixel-wide (3.25 µm) annulus-like area that we used as a binary mask. Next, the bright LamC1–sfGFP signal at the myotendinous junctions was thresholded using the LamC1–sfGFP signal and converted to a binary mask. This mask was dilated two times to remove the myotendinous junction signal from the analysis. These two masks were applied to the LamC1–sfGFP channel of the original image to extract the signal intensity of the LamC1–sfGFP around the primordium. To obtain the LamC1–sfGFP signal beyond the edge of the primordium (control measurement), the thresholded image of the outer circumference of the primordium was duplicated two times. The first and second duplicate was dilated 30 and 20 times, respectively, and subtracted from each other to generate a 10-pixel-wide (3.25 µm) annulus-like area 6.5 µm away from the outer circumference of the primordium as a binary mask. We plotted the mean intensity of the LamC1–sfGFP signal in each region from individual embryos.

Analysis of actin flow. To image actin flow in single primordium superficial and basal cells, we co-injected BAC DNA coding for *cxcr4b:F-tractin-mNG* with 1 nl of 40 ng µl^{-1} *tol2* mRNA into 1-cell-stage wild-type and *itgb1b*$^{-/-}$ embryos that were also transgenic for *prim:mem-mCherry*. The *itgb1b*$^{-/-}$ embryos were generated by crossing *itgb1b:itgb1b-sfGFP*$^{-/-}$*; prim:mem-mCherry* to *itgb1b:itgb1b-sfGFP*$^{-/-}$ and sorting for embryos lacking Itgb1b–sfGFP expression at 24 h.p.f. The embryos were mounted at 32–34 h.p.f. Clones in the primordium were identified based on mCherry and mNG expression and imaged on their basal side, collecting single planes every 2 s for 3 min.

Actin flow analysis was performed by generating kymographs using Fiji. In brief, a 1 pixel-wide 20 µm ROI line was drawn manually from the centre of the cell outwards across the protrusion on the basal side. The kymograph was generated using the KymoResliceWide plugin provided by E. Katrukha and L. Young (https://imagej.net/KymoResliceWide). In singly labelled cells, the front of the actin flow and the front of the protrusion were visually identified, manually traced and the actin flow rate and protrusion rate were extracted from the slopes of the trace lines. The actin polymerization rate was calculated by subtracting the actin flow rate from the protrusion rate. To image and analyse actin flow in single primordium basal cells across the front-to-rear axis of the primordium, we prepared injected embryos as described above. To identify the location of F-tractin–mNG expressing cells, we first imaged a *z*-stack of the whole primordium. Then switched to the ×100 objective to image the actin flow. The location of F-tractin–mNG expressing cells was later identified based on the entire primordium *z*-stack image. To image F-actin retrograde flow in the tip cells, we used *TgBAC(cxcr4b:F-tractin-mCherry)*; *TgBAC(cxcr4b:EGFP-CaaX)* embryos. The imaging conditions and analysis were identical.

Blastomere transplantation and imaging of primordia with clones expressing Itgb1b–sfGFP and Tln1–YPet. We transplanted 20–50 cells from donor embryos at the 1,000–8,000 cell stage into host embryos of the same stage. All host embryos were wild type. Donor embryos were transgenic for *TgBAC(tln1:tln1-Ypet)* or *itgb1b:itgb1b-sfGFP* and *Tg(prim:mem-mCherry)* or *TgBAC(cxcr4b:F-tractin-mCherry)*. At 28 h.p.f., we isolated embryos that contained donor cells in the primordium based on the expression of the *Tg(prim:mem-mCherry)* or *TgBAC(cxcr4b:F-tractin-mCherry)* transgenes. To observe clones in the superficial cells of the primordium, we used *itgb1b:itgb1b-sfGFP; TgBAC(cxcr4b:F-tractin-mCherry)* as donor embryos. Chimeric embryos were mounted at 32–34 h.p.f. Images were collected every 30 s for 10 min as *z*-stacks with a *z*-step size of 1.0 µm. The green and red fluorescent channels were sequentially scanned to prevent fluorescent bleed-through.

Blastomere transplantation and imaging of primordia with clones depleted in talin activity. We transplanted 20–50 cells from donor embryos at the 1,000–8,000 cell stage into host embryos of the same stage. All host embryos carried *Tg(cldnB:lyn*$_2$*GFP)*. Control donor embryos were transgenic for *Tg(prim:mem-mCherry)*. Talin-depleted donor embryos were obtained from an in-cross of *tln1*$^{-/-}$*; tln2a*$^{+/-}$*; tln2b*$^{-/-}$*; TgBAC(tln1:tln1-YPet)*$^{/+}$*; Tg(prim:mem-mCherry)* fish. Wild-type and talin-depleted donor embryos were injected with 50 ng µl^{-1} *zGrad* mRNA at the 1-cell stage. Embryos (32–34 h.p.f.)

with chimeric primordia were mounted. Images were collected every 5 min for 2 h as *z*-stacks with a *z*-step size of 1.0 µm. The green and red fluorescent channels were sequentially scanned to prevent fluorescent bleed-through. Cumulative migration distance was quantified by manually tracking the tip of the primordia using the "Manual tracking" plugin in Fiji. Kymographs were drawn using the "KymoResliceWide" plugin in Fiji.

Analysis of rear contraction and migration. To analyse rear contractions in the primordium, *TgBAC(cxcr4b:EGFP-CaaX)* embryos were mounted at 33 h.p.f. Images were collected every 30 s for 30 min as *z*-stacks with a *z*-step size of 1.0 µm. As a proxy for the rear cells, we tracked the apical constriction site located in the rear of the primordium (>65 µm from the tip) using the sum-projected EGFP–CaaX signal and the "TrackMate" plugin in Fiji. The contraction of the rear cells was analysed as follows. First, we duplicated the middle nine slices (=8.0 µm) of the *z*-stack and sum-projected them. Next, we subtracted the background from the projected image using 5 pixels in Fiji to enhance the membrane signal. Third, we applied the "Huang" thresholding method to this image and binarized it. Finally, we manually identified two vertices, which were located three cells apart from each other, located at the periphery of the rear region of the primordium, and manually tracked their locations over time.

Live imaging with a Leica 165M FC fluorescence stereo microscope. The experiments detailed below were performed using a Leica 165M FC fluorescence stereo microscope equipped with a Leica DFC345 FX camera.

To assess the migration distance of the primordium in embryos in different genetic scenarios (*cldnB:lyn$_2$GFP; lamC1$^{-/-}$* and *cldnB:lyn$_2$GFP* embryos with clones in the muscle expressing mCherry from the *acta1a* promoter, *TgBAC(lamC1:lamC1-sfGFP)*), 26 h.p.f. (initial distance), 32 h.p.f. (assessment of migration) and 48 h.p.f. embryos, respectively, were imaged. The *TgBAC(lamC1:lamC1-sfGFP)* copy number was determined based on the intensity of the sfGFP fluorescence. Distance measurements were performed using Fiji.

To measure the migration distance of the primordium in *itgb1b$^{-/-}$* embryos, 54 h.p.f. embryos were generated by crossing *itgb1b:itgb1b-sfGFP$^{+/-}$; prim:mem-mCherry* fish with *itgb1b:itgb1b-sfGFP$^{+/-}$* fish. *itgb1b$^{-/-}$* embryos were identified by the absence of Itgb1b–sfGFP expression. The primordium migration distance was measured using Fiji. Note that the primordium reaches the tip of the tail by 42 h.p.f. in wild-type embryos[50].

To analyse the distance that the primordium migrated in various mutant backgrounds at 48 h.p.f., the following crosses were set up to obtain embryos of the indicated genotypes. After imaging, the embryos were digested and genotyped if required.

(Z) tln1$^{-/-}$ embryos: in-cross of *tln1$^{-/-}$; TgBAC(tln1:tln1-YPet)$^{/+}$; prim:mem-mCherry* fish. Embryos were sorted against Tln1–YPet and for mem-mCherry.

(Z) tln2a$^{-/-}$ embryos: in-cross of *tln2a$^{+/-}$; cldnB:lyn$_2$GFP* fish. After the experiment, embryos were genotyped for *tln2a*.

(MZ) tln2b$^{-/-}$ embryos: in-cross of *tln2b$^{-/-}$; cldnB:lyn$_2$GFP* fish.

(Z) tln1$^{-/-}$; (Z) tln2a$^{-/-}$ embryos: in-cross of *tln1$^{-/-}$; TgBAC(tln1:tln1-YPet)$^{/+}$; tln2a$^{+/-}$; prim:mem-mCherry*. Embryos were sorted against Tln1–YPet and for mem-mCherry. After the experiment embryos were genotyped for *tln2a*.

(Z) tln1$^{-/-}$; (MZ) tln2b$^{-/-}$ embryos: in-cross of *tln1$^{-/-}$; TgBAC(tln1:tln1-YPet)$^{/+}$; tln2b$^{-/-}$; prim:mem-mCherry* fish. Embryos were sorted against Tln1–YPet and for mem-mCherry.

(Z) tln2a$^{-/-}$; (MZ) tln2b$^{-/-}$ embryos: in-cross of *tln2a$^{+/-}$; tln2b$^{-/-}$; cldnB:lyn$_2$GFP* fish. After the experiment, embryos were genotyped for *tln2a*.

(Z) tln1$^{-/-}$; (Z) tln2a$^{-/-}$; (MZ) tln2b$^{-/-}$ embryos: in-cross of *tln1$^{-/-}$; TgBAC(tln1:tln1-YPet)$^{/+}$; tln2a$^{+/-}$; tln2b$^{-/-}$; prim:mem-mCherry* fish. Embryos were sorted against Tln1–YPet and for mem-mCherry. After the experiment, embryos were genotyped for *tln2a*.

(MZ) itgb1a$^{-/-}$ embryos: in-cross of *itgb1a$^{-/-}$; cldnB:lyn$_2$GFP* fish.

(Z) itgb1b$^{-/-}$ embryos: in-cross of *itgb1b$^{-/+}$; cldnB:lyn$_2$GFP* fish. After the experiment, the embryos were genotyped for *itgb1b*.

(MZ) itgb1a$^{-/-}$; (Z) itgb1b$^{-/+}$ embryos: cross of *itgb1a$^{-/-}$* female fish to *itgb1a$^{-/+}$; itgb1b$^{+/-}$; cldnB:lyn$_2$GFP* male fish. After the experiment, the embryos were genotyped for *itgb1a* and *itgb1b*.

(Z) itgb1a$^{-/+}$; (Z) itgb1b$^{-/-}$ and *(Z) itgb1a$^{-/-}$; (Z) itgb1b$^{-/-}$* embryos: cross of *itgb1a$^{-/+}$; itgb1b:itgb1b-sfGFP$^{-/-}$; prim:mem-mCherry* fish to *itgb1a$^{-/+}$; itgb1b:itgb1b-sfGFP$^{+/-}$* fish. Embryos were sorted against Itgb1b–sfGFP and for mem-mCherry. After the experiment, the embryos were genotyped for *itgb1a*.

ctnna1-citrine/ctnna1-citrine and *ctnna1-citrine/ctnna1-citrine; TgBAC(cxcr4b:zGrad)$^{/+}$* embryos: in-cross of *ctnna1-citrine$^{/+}$; TgBAC(cxcr4b:zGrad)$^{/+}$; prim:mem-mCherry* fish. Embryos were sorted against homozygous Ctnna1–Citrine by fluorescence intensity and for mem-mCherry. Embryos with zGrad expression were identified by mScarlet expression in the heart.

To assess the degradation of sfGFP by zGrad, we injected an mRNA injection mix containing 50 ng µl^{-1} of *sfGFP-ZF1* mRNA, 50 ng µl^{-1} of *mCherry-ZF1* mRNA with or without 50 ng µl^{-1} of *zGrad* mRNA into 1-cell-stage embryos. To assess the degradation of YPet by zGrad, we injected an mRNA injection mix containing 50 ng µl^{-1} of *YPet-ZF1* mRNA, 50 ng µl^{-1} of *mCherry-ZF1* mRNA with or without 50 ng µl^{-1} of *zGrad* mRNA into 1-cell-stage embryos. As a control, we injected an mRNA injection mix containing 50 ng µl^{-1} of *mNG-ZF1* mRNA, 50 ng µl^{-1} of *mCherry-ZF1* mRNA with or without 50 ng µl^{-1} of *zGrad* mRNA into 1-cell-stage embryos. Injected embryos at 8 h.p.f. were dechorionated and imaged under the microscope. Preparation of mRNAs was performed as previously described[9].

Live imaging with an Axioplan microscope. The experiments detailed below were performed using an Axioplan Microscope (Zeiss) equipped with an Axiocam (Zeiss) and a ×5 (NA 0.25) objective.

Documentation of the phenotype of *lamC1$^{-/-}$; TgBAC(lamC1:lamC1-sfGFP)* embryos. The *TgBAC(lamC1:lamC1-sfGFP)* was identified based on sfGFP fluorescence. The *lamC1* mutant embryos were identified and scored based on the morphological defects at 48 h.p.f.

Documentation of the phenotype of *itgb1b$^{-/-}$* embryos. *itgb1b$^{-/-}$* embryos were generated by crossing *itgb1b:itgb1b-sfGFP$^{+/-}$; prim:mem-mCherry* fish to *itgb1b:itgb1b-sfGFP$^{+/-}$* fish. *itgb1b$^{-/-}$* embryos were identified by the absence of Itgb1b–sfGFP fluorescence.

Primordium migration distance quantification. To quantify the cumulative migration distance of the primordium, time-lapse image sequences were maximum- or sum-projected, and the tip of the primordium was tracked using the "Manual tracking" plugin provided by Fabrice Cordelieres in Fiji (https://imagej.nih.gov/ij/plugins/manual-tracking.html).

Circularity analysis of the primordium. To quantify the circularity of the primordium, we limited the length of the primordium to the first 100 µm from the tip of the primordium. *Z*-stacks were sum-projected. Using Fiji, the primordium region was manually cropped based on the intensity of Lyn$_2$–GFP fluorescence. Then, a median filter with a radius of 6 pixels was applied and the background was subtracted using a rolling ball radius of 100 pixels. Images were rendered binary using the "Huang" thresholding algorithm to obtain a clear outline of the primordium. Finally, we quantified the circularity of the primordium for each time point using the "Analyze particles" macro in Fiji. The circularity *C* is defined as

$$C = 4\pi \frac{A}{P^2},$$

where *A* is the area of the primordium and *P* is the perimeter.

Analysis of Itgb1b–sfGFP and Tln1–YPet localization in primordium cells. We analysed the spatial distribution of Itgb1b–sfGFP and Tln1–YPet with respect to F-tractin–mCherry and mem-mCherry at the basal side of small clones of labelled primordium cells in two ways. First, we chose a single slice at the basal side of the cells in a clone. The clone contour was manually selected based on the F-tractin–mCherry or mem-mCherry fluorescence using a 5 pixel-wide (=1.625 µm) segmented line to obtain the fluorescence intensity profile at each time point for the green and red channels in Fiji. Second, we assessed the colocalization of the fluorescently tagged proteins using the "coloc2" plugin in Fiji. Before applying the coloc2 plugin, we processed the images as follows: due to photobleaching, only the first ten time points were included for analysis. Images were rotated such that the direction of migration aligned with the *x* axis. Then the images were re-sliced to obtain transverse sections in the *xz* plane. This resulted in images with the basal sides of the cells pointing upwards (*z* axis of imaging) and the direction of migration pointing to the right. Next, a median filter with 1 pixel width was applied and the images were rotated again such that the basal sides of the cells were horizontally aligned. An ROI with a width of 3.25 µm from the basal membrane inward was manually defined as the basal region of cells and used for the coloc2 analysis in Fiji with a custom-written macro. The macro compiles the individual ROIs of the basal region from each time point, creates a mask based on the sum intensities of the green and red channels using the "Default" method in Fiji. The individual ROIs were also compiled into a single image for each channel as a montage as shown in (Extended Data Fig. 4d). The macro then calculates the degree of colocalization, the Li's ICQ value, using the coloc2 function in Fiji. Li's ICQ is calculated as follows[78]. For each pixel in the ROI, the product of the difference of intensity and the mean intensity for each channel is calculated ((Ch1 – mean(Ch1)) × (Ch2 – mean(Ch2)). Then, the number of pixels with a positive product are normalized to the total pixel number and 0.5 is subtracted. Therefore, Li's ICQ ranges from −0.5 (signals perfectly segregated) to 0.5 (signals perfectly overlap). We performed this analysis for three consecutive *xz* slices per clone and pooled the data for display in the panel.

Generation of embryos lacking most talin activity. Control wild-type embryos and embryos from an in-cross of *tln1$^{-/-}$; tln2a$^{+/-}$; tln2b$^{-/-}$; TgBAC(tln1:tln1-YPet)$^{/+}$; Tg(prim:mem-mCherry)* fish were injected with 50 ng µl^{-1} *zGrad* mRNA at the 1-cell stage. At 28 h.p.f., embryos were fixed with 4% PFA in PBST. After imaging, individual embryos were genotyped for *tln2a*.

Analysis of skin-generated BM wrinkles and traction. A 30 × 30 µm ROI centred on a transient increase in LamC1–sfGFP fluorescence intensity at the third time

point in a four-dimensional stack spanning five time points with a 1 min interval was manually defined. The third point was set to 0 min. To visualize the LamC1–sfGFP increase as a graph, the stack was maximum-projected along the *z* axis. The fluorescence intensity profile was extracted along a 10-µm line ROI across the LamC1–sfGFP increase at the 0 min time point. The same fluorescence intensity profiles along the same line ROI were obtained for the −1 min and +1 min time points. The fluorescence intensity was normalized to the mean of the −1 min time point. Traction was analysed using Embryogram and calculated and visualized with ParaView (ParaView-5.8.1, Kitware). For the traction stress calculation, a Young's modulus of 566.7 Pa was used for the BM based on the AFM measurements (Fig. 6c) and a Poisson ratio of 0.45. Traction was obtained using the −2 min time point as a reference for the undeformed BM. To quantify the temporal change of traction stresses around the local increases in LamC1–sfGFP, we averaged the traction stresses measured at the three marks closest to the LamC1–sfGFP increase. Particle image velocimetry (PIV) analysis of the basal skin cells was performed for detecting the displacement of the membrane from −1 min to 0 min using the "PIVlab" plugin (v.2.38 by W. Thielicke) in Matlab (v.9.9, MathWorks). Every second vector was visualized on the cell membrane image at the −1 min time point. The displacement of the BM was obtained by Embryogram. The three-dimensional quiver plots of the displacement of the BM from −2 min (reference) to 0 min with the scale factor 3 were drawn using ParaView (ParaView-5.8.1, Kitware).

Analysis of primordium-generated traction stresses and angles of BM deformation. Four-dimensional confocal *z*-stacks were denoised by applying a median filer (width of 2 pixels) and analysed in Embryogram. In Embryogram, an area containing a well-defined bleach pattern that was in front of the primordium at the first time point of the time lapse was manually selected. Bleached cylinders with radii between 2 and 8 pixels (= 0.65–2.6 µm) were identified and tracked over time in the time lapse and manually curated in Embryogram. To subtract rigid motions, we manually selected cylinders to calculate the global displacement. If the bleach pattern spanned the horizontal myoseptum and extended past the primordium on either side, we used the two rows of bleached cylinders furthest from the horizontal myoseptum on both sides of the bleach pattern. If the bleach pattern did not span the horizontal myoseptum, we used the two rows of bleached cylinders furthest from the horizontal myoseptum on one side of the embryo only. To perform the "Finite Element" analysis, we constructed volumetric meshes on both sides of the BM to represent the skin and the muscle above and below the primordium, used up-sampling of 2, discretization order of 2, a Young's modulus of 566.7 Pa and a Poisson ratio of 0.45. We excluded the cylinders on the edge of the bleach pattern from the analysis because these cylinders were often incorrectly tracked.

To analyse the angles between the displacement vectors and the direction of migration, and the traction stresses under the primordium, we exported data files containing (1) the *x*, *y* and *z* coordinates, (2) the displacement vector and (3) the traction stress vector for each extrapolated vertex from ParaView (ParaView-5.8.1, Kitware). Then, we semi-manually selected vertices in the front, the middle and the rear part of the primordia defined as the 0–15 µm, 15–65 µm and >65 µm from the tip of the primordium, respectively. For this analysis, we used the 40, 60 and 80 min time points of the time lapse videos. We also included cylinders with a distance of <10 µm to the primordium in the analysis. For controls, we used cylinders that are at a distance of <20 µm from the horizontal myoseptum on the dorsal and ventral sides along the migratory route of the primordium. This corresponds to the maximal width of the primordium. In Fiji, we maximum-projected the primordium channel, manually traced the primordium edge, converted it to a binary mask and dilated the mask 10 µm. Then, we applied this binary mask to the maximum-projected BM channel at the first time point. The approximate coordinates of the cylinders within the mask were manually recorded in Fiji. Using a custom-written R script, we compared these approximate cylinder-coordinates to the actual cylinder-coordinates obtained from the tracking in Embryogram by minimizing the distance between these two, and extracted information of actual cylinders only in the front, the middle and the rear of the primordium. BM displacement angles were analysed based on the displacement of the bleached cylinder in the *xy* plane in relation to the direction of primordium migration or the horizontal myoseptum in the case of the controls. The direction of primordium migration/horizontal myoseptum was manually obtained in Fiji. Half-circle polar diagrams were drawn using Matlab. The cosines of these angles are shown in Fig. 6i. The magnitude of traction stress in the *x* and *y* directions and in the *z* direction were extracted from cylinder located as described above.

Three-dimensional and two-dimensional displacement vectors, the magnitude of the traction stresses, the components of the stress tensors and the magnitude of the stresses in the direction of primordium migration/horizontal myoseptum were visualized using ParaView (ParaView-5.8.1, Kitware). To calculate the stresses in the direction of primordium migration, we first obtained the vector for the direction of primordium migration in three-dimensions using Fiji. We next calculated the cross-products (cross-products 1) between this directional vector and the normal vectors to the surface of the BM. To obtain the vectors normal to the primordium direction, we calculated the cross-products (cross-products 2) between cross-products 1 and the normal vectors to the surface of the BM. Finally, we generated stress vectors by multiplying cross-products 2 with the stress tensor obtained by the Embryogram simulation. This calculation was done in Paraview. The confocal stack of the primordium channel was binarized using the Li's thresholding method in Fiji and superimposed. The data were visualized in ParaView.

Nuclear tracking of the primordium cells. To analyse the direction of primordium cells, we used previously published cell tracking data[11]. The imaging condition and tracking method using Imaris v.8.0 (Bitplane, Oxford Instruments) were the same as described above. Tracking data for three primordia were exported and analysed using the R environment. In brief, the cosine between the directions of two given cells at a given time frame was obtained. We performed this analysis for all the combinations of two cells for all the time frames and pooled data. The trajectories of the primordium cells were also drawn using R.

Statistical tests. All the statistical tests were performed using Prism 9 (GraphPad software). We first tested the normality of distribution in each group with a Kolmogorov–Smirnov (KS) test. When $P > 0.05$ in the KS test was obtained for a multiple comparison, we performed an ordinary one-way analysis of variance (ANOVA) test followed by a multiple comparison test specified in the figure legend; for a comparison of two groups, we performed an *F*-test to compare variances. When $P > 0.05$ in the *F*-test was obtained in the two-group comparison, we performed a two-tailed *t*-test. Otherwise, we performed a two-tailed *t*-test with Welch's correction (Welch's *t*-test). When we obtained $P < 0.05$ in the initial KS test for either the multiple comparison or two-group comparison, we subsequently performed a two-tailed Mann–Whitney test between two groups. For the qualitative TEM experiments (Figs. 1a and 2d and Extended Data Fig. 1b), one embryo was analysed. For Figs. 2g,h, 4a–d and 8a, all embryos originate from a single experiment. All other experiments were performed two or more times.

Reporting Summary. Further information on research design is available in the Nature Research Reporting Summary linked to this article.

Data availability

Previously published genome assemblies as either GRCz10 or GRCz11 that were used here for the design of gRNA constructs are available for *tln1*, *tln2a*, *tln2b*, *itgb1a* and *itgb1b* under accession codes ENSDARG00000100729, ENSDARG00000017901, ENSDARG00000110973, ENSDARG00000071863 and ENSDARG00000104484, respectively. All other data supporting the findings of this study are available from the corresponding authors on reasonable request. Source data are provided with this paper.

Code availability

The code for Embryogram software has been deposited at Zenodo (https://zenodo.org/record/5762146#.Ya5X0y-B1QJ)[29]. The codes for image analysis using ImageJ and R are provided as a zip file.

References

50. Kimmel, C. B., Ballard, W. W., Kimmel, S. R., Ullmann, B. & Schilling, T. F. Stages of embryonic development of the zebrafish. *Dev. Dyn.* **203**, 253–310 (1995).
51. Valentin, G., Haas, P. & Gilmour, D. The chemokine SDF1a coordinates tissue migration through the spatially restricted activation of Cxcr7 and Cxcr4b. *Curr. Biol.* **17**, 1026–1031 (2007).
52. Kettleborough, R. N. et al. A systematic genome-wide analysis of zebrafish protein-coding gene function. *Nature* **496**, 494–497 (2013).
53. Wang, J. et al. Anosmin1 shuttles Fgf to facilitate its diffusion, increase its local concentration, and induce sensory organs. *Dev. Cell* **46**, 751–766.e12 (2018).
54. Knaut, H., Blader, P., Strahle, U. & Schier, A. F. Assembly of trigeminal sensory ganglia by chemokine signaling. *Neuron* **47**, 653–666 (2005).
55. Trinh le, A. et al. A versatile gene trap to visualize and interrogate the function of the vertebrate proteome. *Genes Dev.* **25**, 2306–2320 (2011).
56. Zigman, M., Trinh le, A., Fraser, S. E. & Moens, C. B. Zebrafish neural tube morphogenesis requires Scribble-dependent oriented cell divisions. *Curr. Biol.* **21**, 79–86 (2011).
57. Cronan, M. R. & Tobin, D. M. Endogenous tagging at the *cdh1* locus for live visualization of E-cadherin dynamics. *Zebrafish* **16**, 324–325 (2019).
58. Levic, D. S., Yamaguchi, N., Wang, S., Knaut, H. & Bagnat, M. Knock-in tagging in zebrafish facilitated by insertion into non-coding regions. *Development* https://doi.org/10.1242/dev.199994 (2021).
59. Gagnon, J. A. et al. Efficient mutagenesis by Cas9 protein-mediated oligonucleotide insertion and large-scale assessment of single-guide RNAs. *PLoS ONE* **9**, e98186 (2014).
60. Shen, B. et al. Generation of gene-modified mice via Cas9/RNA-mediated gene targeting. *Cell Res.* **23**, 720–723 (2013).
61. Wu, Q. et al. Talin1 is required for cardiac Z-disk stabilization and endothelial integrity in zebrafish. *FASEB J.* **29**, 4989–5005 (2015).

62. Iida, A., Wang, Z., Hirata, H. & Sehara-Fujisawa, A. Integrin β_1 activity is required for cardiovascular formation in zebrafish. *Genes Cells* **23**, 938–951 (2018).
63. Fuentes, F., Reynolds, E., Lewellis, S. W., Venkiteswaran, G. & Knaut, H. A plasmid set for efficient bacterial artificial chromosome (BAC) transgenesis in zebrafish. *G3 (Bethesda)* **6**, 829–834 (2016).
64. Warming, S., Costantino, N., Court, D. L., Jenkins, N. A. & Copeland, N. G. Simple and highly efficient BAC recombineering using galK selection. *Nucleic Acids Res.* **33**, e36 (2005).
65. Sztal, T., Berger, S., Currie, P. D. & Hall, T. E. Characterization of the laminin gene family and evolution in zebrafish. *Dev. Dyn.* **240**, 422–431 (2011).
66. Austen, K. et al. Extracellular rigidity sensing by talin isoform-specific mechanical linkages. *Nat. Cell Biol.* **17**, 1597–1606 (2015).
67. Johnson, H. W. & Schell, M. J. Neuronal IP3 3-kinase is an F-actin-bundling protein: role in dendritic targeting and regulation of spine morphology. *Mol. Biol. Cell* **20**, 5166–5180 (2009).
68. Mastop, M. et al. Characterization of a spectrally diverse set of fluorescent proteins as FRET acceptors for mTurquoise2. *Sci. Rep.* **7**, 11999 (2017).
69. Gibson, D. G. et al. Enzymatic assembly of DNA molecules up to several hundred kilobases. *Nat. Methods* **6**, 343–345 (2009).
70. Kwan, K. M. et al. The Tol2kit: a multisite gateway-based construction kit for Tol2 transposon transgenesis constructs. *Dev. Dyn.* **236**, 3088–3099 (2007).
71. Higashijima, S., Okamoto, H., Ueno, N., Hotta, Y. & Eguchi, G. High-frequency generation of transgenic zebrafish which reliably express GFP in whole muscles or the whole body by using promoters of zebrafish origin. *Dev. Biol.* **192**, 289–299 (1997).
72. Knaut, H., Werz, C., Geisler, R., Nusslein-Volhard, C. & Tubingen Screen, C. A zebrafish homologue of the chemokine receptor Cxcr4 is a germ-cell guidance receptor. *Nature* **421**, 279–282 (2003).
73. Koster, R. W. & Fraser, S. E. Tracing transgene expression in living zebrafish embryos. *Dev. Biol.* **233**, 329–346 (2001).
74. Thisse, C. & Thisse, B. High-resolution in situ hybridization to whole-mount zebrafish embryos. *Nat. Protoc.* **3**, 59–69 (2008).
75. Zoellner, H., Paknejad, N., Manova, K. & Moore, M. A. A novel cell-stiffness-fingerprinting analysis by scanning atomic force microscopy: comparison of fibroblasts and diverse cancer cell lines. *Histochem. Cell Biol* **144**, 533–542 (2015).
76. Loparic, M. et al. Micro- and nanomechanical analysis of articular cartilage by indentation-type atomic force microscopy: validation with a gel-microfiber composite. *Biophys. J.* **98**, 2731–2740 (2010).
77. Lau, S. et al. A negative-feedback loop maintains optimal chemokine concentrations for directional cell migration. *Nat. Cell Biol.* **22**, 266–273 (2020).
78. Li, Q. et al. A syntaxin 1, $G\alpha_o$, and N-type calcium channel complex at a presynaptic nerve terminal: analysis by quantitative immunocolocalization. *J. Neurosci.* **24**, 4070–4081 (2004).

Acknowledgements

We thank R. Lehmann, L. Christiaen, D. Rifkin, M. Schober, J. Torres-Vázquez, W. Qian, P. Vagni, S. Lau and T. Colak-Champollion for critical comments; T. Gerson, T. Colak-Champollion and A. Feitzinger for reagents; T. Gerson, J. Proietti and S. Pirani for excellent fish care; N. Paknejad for advice on AFM; M. Cammer and Y. Deng for advice on microscopy; A. Liang, C. Petzold and K. Dancel-Manning for consultation and assistance with TEM work; and A. Ferrari and N. Chala for AFM consultation. The use of the NYULH DART Microscopy Laboratory (P30CA016087) and the Memorial Sloan Kettering Molecular Cytology Core Facility (P30 CA008748) is gratefully acknowledged. For providing the zebrafish knockout allele *lamC1*^{sq9866}, we thank the Zebrafish International Resource Center. For providing the *cdh1:cdh1-tdTomato* line, we thank M. Cronan and D. Tobin. This work was supported by NIH grant NS102322 (H.K.), by an NYSTEM fellowship C322560GG (N.Y.), by an American Heart Association fellowship 20PRE35180164 (N.Y.), in part through the NYU IT High Performance Computing resources, services, and staff expertise, the NSF CAREER award 1652515 (D.N.), the NSF grants IIS-1320635 (D.N.), OAC-1835712 (D.N.), OIA-1937043 (D.N.), CHS-1908767 (D.N.), CHS-1901091 (D.N.), a gift from Adobe Research (D.N.), a gift from nTopology (D.N.), and a gift from Advanced Micro Devices (D.N.).

Author contributions

N.Y., D.P. and H.K. conceptualized the study and designed the experiments. N.Y. performed all the zebrafish experiments with support from H.K., except for the AFM measurements, which were performed by B.W. with samples prepared by N.Y. The Embryogram software was developed by Z.Z., T.S. and D.P. (with inputs from N.Y. and H.K.). N.Y. analysed most of the data with help from Z.Z. and T.S. for the traction stress analysis and from Z.Z. and B.W. for the AFM data analysis. N.Y. and H.K. wrote the main manuscript (with input from Z.Z., T.S. and D.P.). Z.Z., T.S. and D.P. wrote Supplementary Note 1 (with input from N.Y. and H.K.). All authors approved of and contributed to the final version of the manuscript.

Competing interests

The authors declare no competing interests.

Additional information

Extended data is available for this paper at https://doi.org/10.1038/s41556-022-00844-9.

Supplementary information The online version contains supplementary material available at https://doi.org/10.1038/s41556-022-00844-9.

Correspondence and requests for materials should be addressed to Daniele Panozzo or Holger Knaut.

Peer review information *Nature Cell Biology* thanks Anna Huttenlocher, and the other, anonymous, reviewer(s) for their contribution to the peer review of this work. Peer reviewer reports are available.

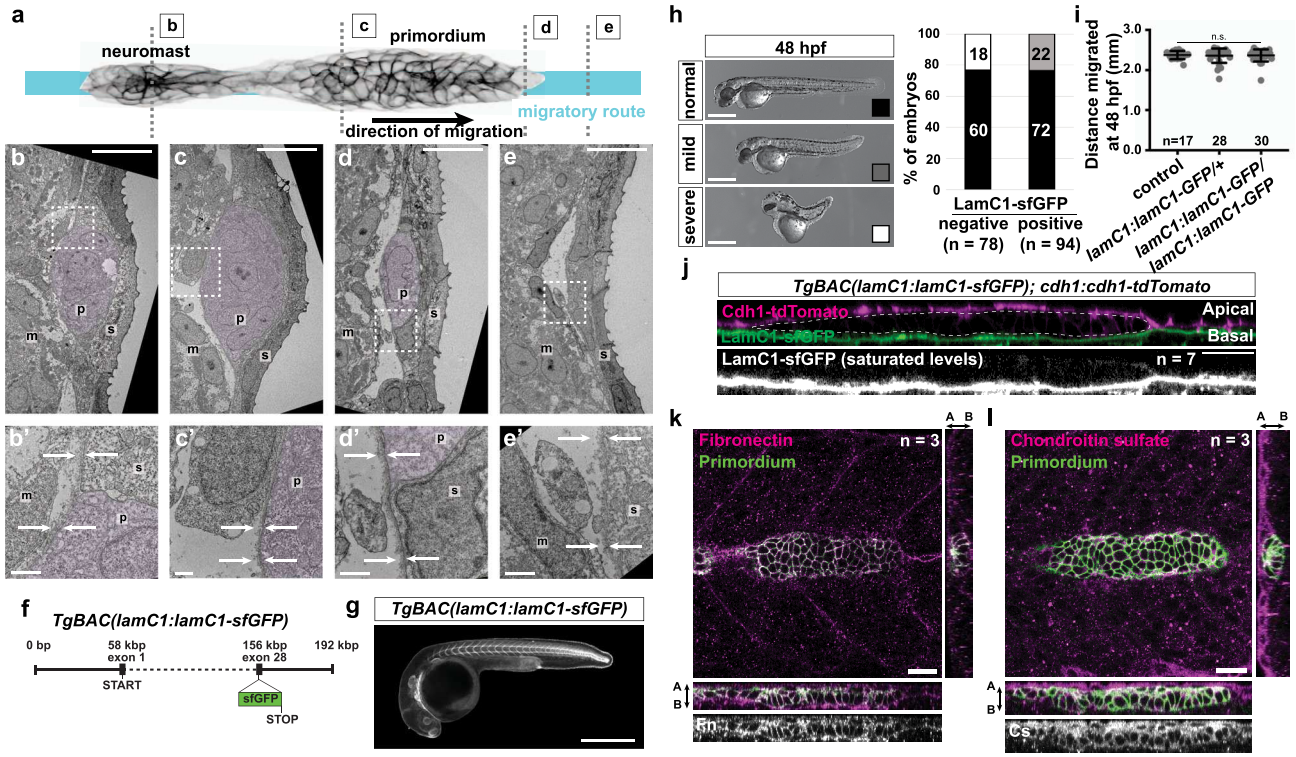

Extended Data Fig. 1 | Ultrastructure of the basement membrane along the migratory route of the primordium and the characterization of the *TgBAC(lamC1:lamC1-sfGFP)* line. a, Overview of the primordium. Dotted lines indicate the location of the cross-sections shown in (**b**-**e**). **b**-**e**, TEM images of cross-sections at the level of the most recently deposited neuromast (**b**), at the level of the primordium's rear (**c**), at the level of the primordium's front (**d**), and in front of the primordium (**e**). Scale bars = 10 μm. **b'**-**e'**, Magnification of area outlined by a dotted line in (**b**-**e**). Scale bars = 1 μm. The skin (s), primordium (p, purple hue), the muscle (m), and the BM (arrows) are indicated. n = 1 embryo. **f**, Schematic of the *TgBAC(lamC1:lamC1-sfGFP)* transgene. **g**, Image of the expression of LamC1-sfGFP from *TgBAC(lamC1:lamC1-sfGFP)* transgene in a 28 hpf embryo. The image is a sum-projected z-stack. Scale bar = 0.5 mm. **h**, The *TgBAC(lamC1:lamC1-sfGFP)* transgene partly rescues the *lamC1* mutant phenotype. Crosses from *lamC1-/+*; *lamC1:lamC1-sfGFP* to *lamC1-/+* fish resulted in embryos with three different phenotypes shown on the left. Quantification of the phenotypic categories from these crosses for non-transgenic embryos and embryos expressing LamC1-sfGFP are shown on the right. Note that the mild phenotype correlates with the presence of LamC1-sfGFP and the severe phenotype represents the *lamC1* mutant phenotype. Scale bars = 0.5 mm. **i**, Quantification of the primordium migration in the presence of different copy numbers of the *TgBAC(lamC1:lamC1-sfGFP)* transgene. Data points, means, and SD are indicated. n.s.: p = 0.6514 (non-transgenic vs. *lamC1:lamC1-sfGFP/+*), p = 0.7842 (non-transgenic vs. *lamC1:lamC1-sfGFP/lamC1:lamC1-sfGFP*) (two-tailed Mann-Whitney test). **j**, Cross-section along apical-basal axis of a primordium (dotted line in top panel) of embryos expressing LamC1-sfGFP (BM) and the Cdh1-tdTomato (skin). The LamC1-sfGFP signal is enhanced to saturated levels (bottom panel). Scale bars = 25 μm. **k**, Images of slices from a z-stack of 32 hpf *TgBAC(cxcr4b:EGFP-CaaX)* embryos stained for Fibronectin and GFP. Orthogonal views are shown. **l**, Images of slices from a z-stack of 32 hpf *TgBAC(cxcr4b:EGFP-CaaX)* embryos stained for Chondroitin sulfate and GFP. Orthogonal views are shown. For **h**, **i**, n= number of embryos.

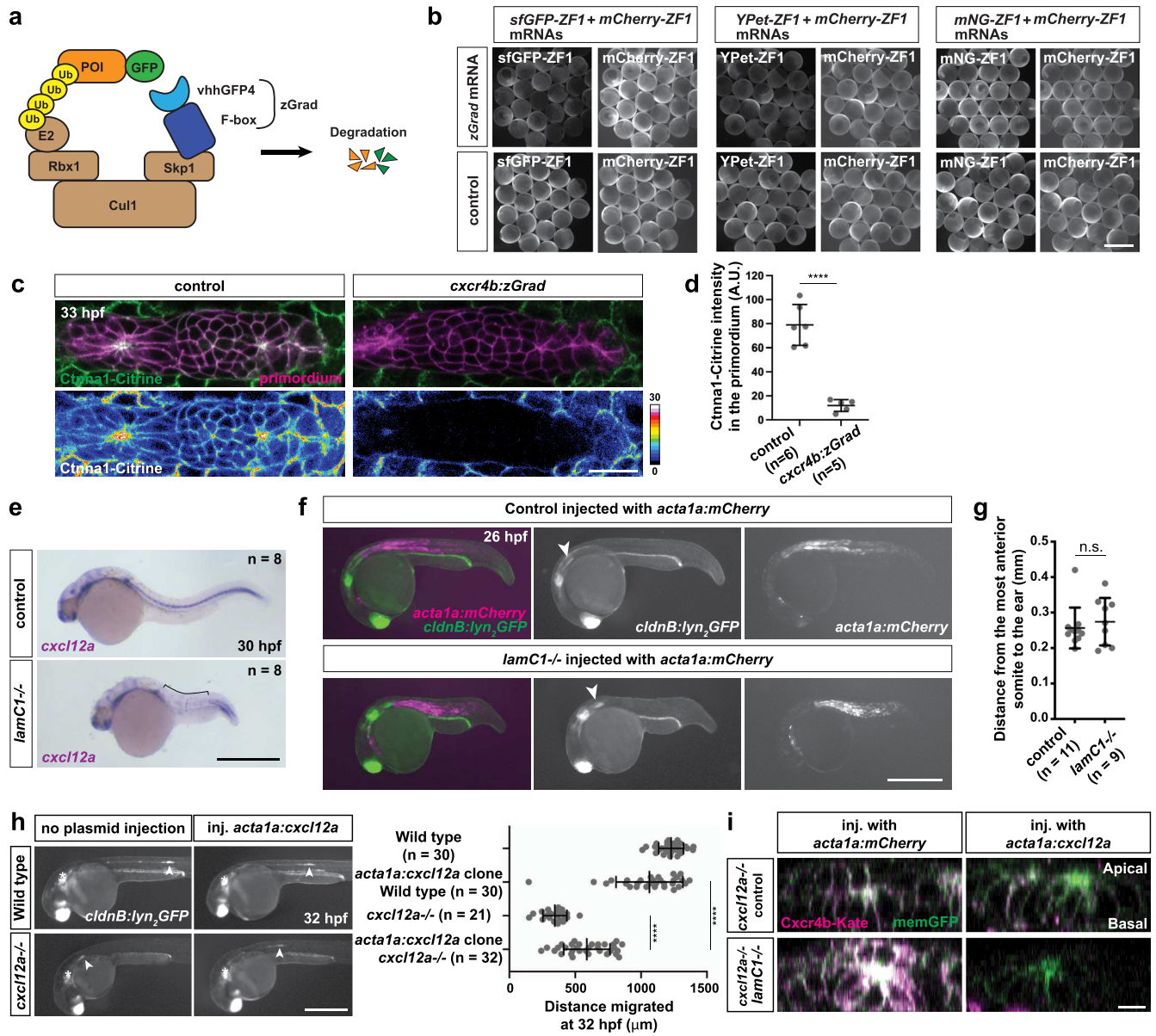

Extended Data Fig. 2 | Depletion of Ctnna1-Citrine by zGrad and characterization of the *lamC1* mutants. a, Principle of zGrad-mediated protein degradation. **b**, Left: 8 hpf embryos injected with *sfGFP-ZF1* mRNA and *mCherry-ZF1* mRNA with or without co-injected *zGrad* mRNA. Middle: 8 hpf embryos injected with *YPet-ZF1* mRNA and *mCherry-ZF1* mRNA with or without co-injected *zGrad* mRNA. Right: 8 hpf embryos injected with *mNeonGreen-ZF1* mRNA and *mCherry-ZF1* mRNA with or without co-injected *zGrad* mRNA. n ≥ 20 embryos. Scale bar: 1 mm. **c**, Single confocal slices of primordia in *prim:mem-mCherry*; *ctnna1:ctnna1-citrine* control (left) and *prim:mem-mCherry*; *ctnna1:ctnna1-citrine*; *cxcr4b:zGrad* 32 hpf embryos (right). Lower panels show the Ctnna1-Citrine fluorescence as a heat map. Scale bar = 20 µm. **d**, Quantification of the Ctnna1-Citrine fluorescence intensity in control and zGrad-expressing embryos at 32 hpf. Data points, means, and SD are indicated. ****: p<0.0001 (two-tailed Welch's t-test). **e**, Expression of *cxcl12a* in control (wild-type or *lamc1-/+*) and *lamC1* mutant 30 hpf embryos. Bracket indicates the location of interrupted *cxcl12a* expression domain. Scale bar = 0.5 mm. **f**, mCherry-expressing clones in muscle of 26 hpf control (wild-type or *lamC1-/+*) and *lamC1* mutant embryos also transgenic for *cldnB:lyn$_2$GFP*. Arrowheads indicate the position of primordium. Scale bar = 0.5 mm. **g**, Quantification of the distance from the ear to the first somite in the indicated genotypes at 26 hpf. Data points, means, and SD are indicated. n.s.: p=0.5516 (two-tailed Mann-Whitney test). **h**, Images of the primordium in wild-type and *cxcl12a-/-* 32 hpf embryos with clones in the trunk muscle that express Cxcl12a together with mCherry (not shown) (Left). Asterisks indicate the ear and arrowheads the primordium. Scale bar = 0.5 mm. Quantification of the distance migrated by the primordium in the indicated experimental conditions at 32 hpf (Right). Data points, means, and SD are indicated. ****: p<0.0001 (One-way ANOVA followed by Tukey's multiple comparison test). **i**, Cross-sectional images of the Cxcl12a sensor in primordia of *cxcl12a-/-* and *cxcl12a-/-*; *lamC1-/-* embryos with clones in the muscle of the trunk that express mCherry or Cxcl12a. Quantification shown in Fig. 2k. Scale bar = 20 µm. For **d**, **e**, **g**, **h**, n = number of embryos.

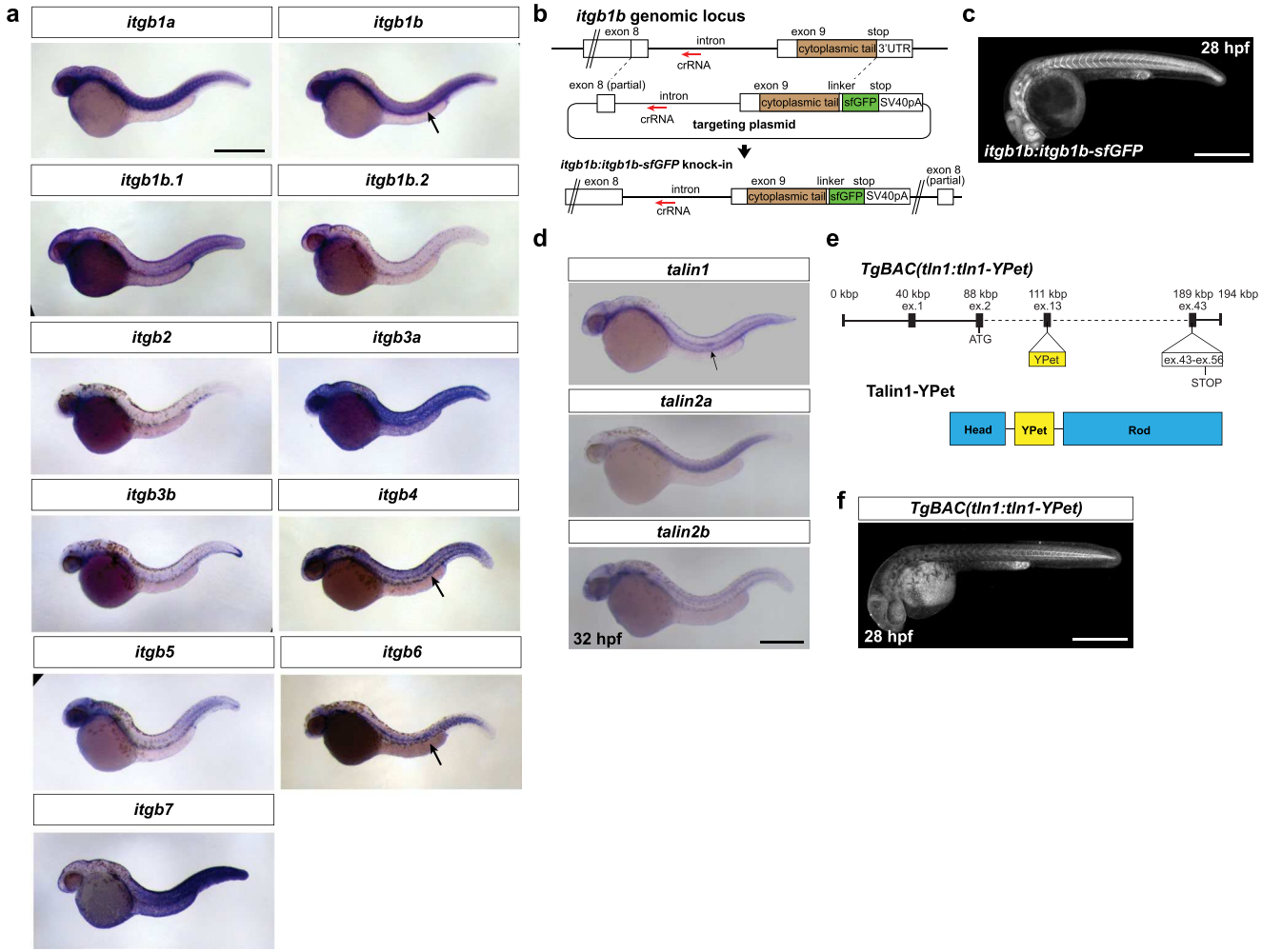

Extended Data Fig. 3 | *β-integrin* and *talin* expression analysis. a, Expression analysis of *β-integrins* in the migrating primordium by *in situ* hybridization on 32 hpf embryos. Note that *itgb8* could not be amplified from embryonic cDNA. Arrows indicate expression in the primordium. Scale bar = 0.5 mm. **b**, Schematics of the *itgb1b* locus, the *itgb1b* targeting cassette, and the modified *itgb1b* locus. **c**, Itgb1b-sfGFP expression in a 28 hpf *itgb1b:itgb1b-sfGFP* embryo. The image is a sum-projected z-stack. Scale bar = 0.5 mm. **d**, *in situ* hybridization against the three zebrafish *talin* genes on 32 hpf embryos. Arrow indicates enriched *talin* expression in the primordium. Scale bar = 0.5 mm. **e**, Schematic of the *TgBAC(tln1:tln1-YPet)* transgene and its protein product. **f**, Tln1-YPet expression in a 28 hpf *tln1:tln1-YPet* embryo. The image is a sum-projected z-stack. Scale bar = 0.5 mm.

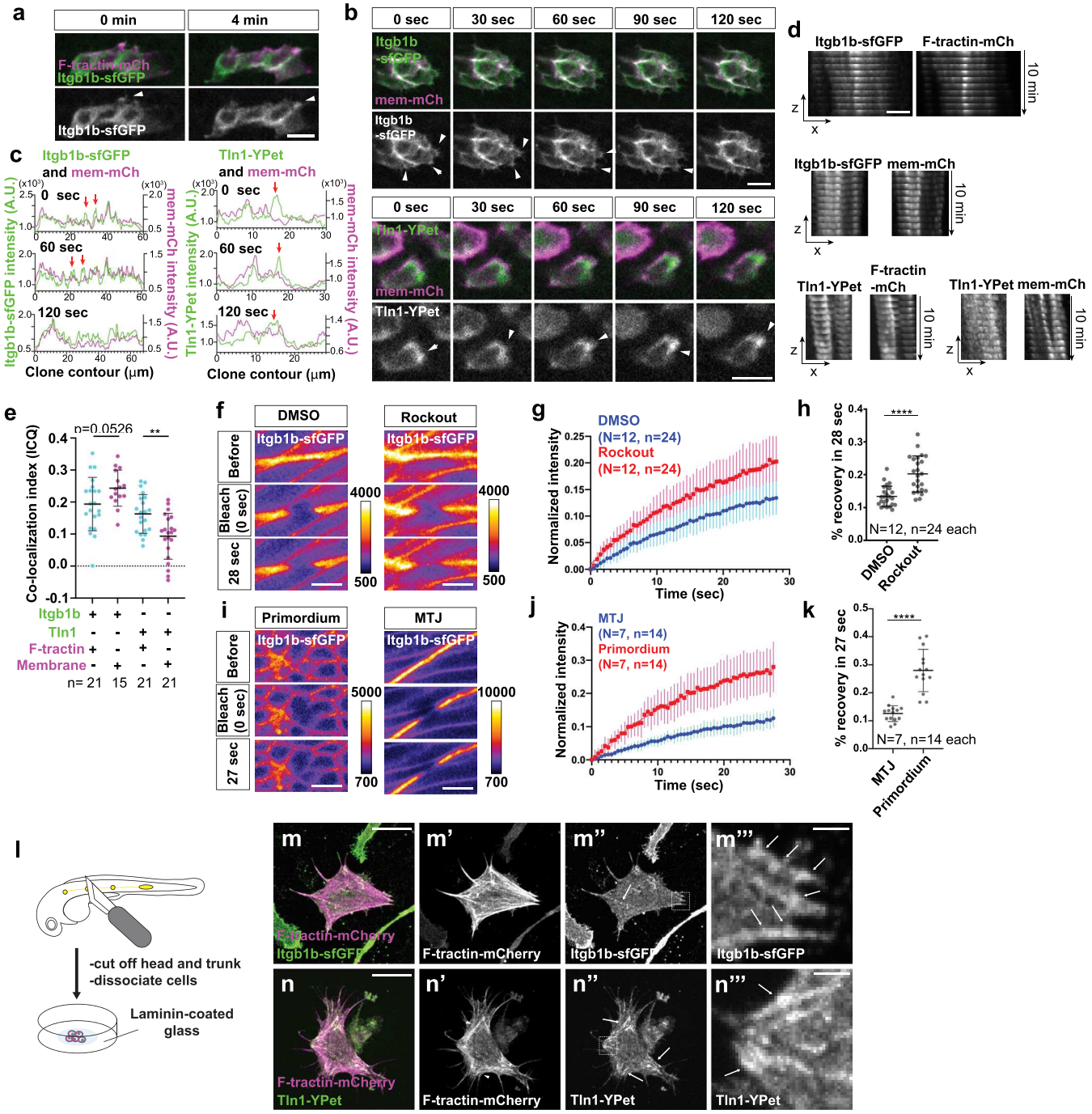

Extended Data Fig. 4 | See next page for caption.

Extended Data Fig. 4 | Integrin-β1b and Talin1 dynamics in cells of the primordium. a, Localization of Itgb1b-sfGFP and F-tractin-mCherry at the apical side of superficial cells in the primordium. The images are single optical slices. Arrowheads indicate Itgb1b-sfGFP clustering. Scale bar = 10 μm. **b**, Localization of Itgb1b-sfGFP (top) and Tln1-YPet (bottom) with membrane-mCherry at the basal sides of cells in clones in the primordium imaged over time taken from Supplementary Video 3. The images are single optical slices. Arrowheads indicate Itgb1b-sfGFP and Tln1-YPet clustering. Scale bar = 10 μm. **c**, Intensity profiles of Itgb1b-sfGFP (left) and Tln1-YPet (right) together with membrane-tethered mCherry along the contours of clones at indicated times taken from Supplementary Video 3. Arrows indicate Itgb1b-sfGFP and Tln1-YPet clusters that do not coincide with membrane-tethered mCherry clustering. Representative profile of 5 or more imaged cells. **d**, Montage of 10 consecutive images of the basal sides of the clones. The images are single transverse sections from a time lapse video. Scale bar = 10 μm. **e**, Quantification of co-localization of Itgb1b-sfGFP and Tln1-YPet with F-tractin-mCherry and membrane tethered mCherry. Li's ICQ co-localization indices of 0.5 and −0.5 indicate perfectly co-localized and perfectly anti-co-localized signals, respectively. n = number of cells. Data points, means, and SD are indicated. Three data points were analyzed from the same embryo. **: p=0.0015 (two-tailed t-test). **f**, Images from time-lapse video after photo-bleaching of Itgb1b-sfGFP at the myotendinous junction of embryos treated with DMSO or 50 μM Rockout. GFP intensities are pseudo-colored as a heat map. Scale bars = 10 μm. **g**, Graph of Itgb1b-sfGFP fluorescence intensity over time before and after photo-bleaching in embryos treated with DMSO or 50 μM Rockout. The fluorescence intensities are normalized to the minimal intensities after photo-bleaching. Dots indicate mean intensities and error bars are SD. n = number of experiments, N = number of embryos. **h**, Plot of the percent recovery of Itgb1b-sfGFP fluorescence intensity at 28 sec after photo-bleaching in embryos treated with DMSO or 50 μM Rockout. Data points, means, and SD are indicated. ****: p<0.0001 (two-tailed Welch's t-test). n = number of experiments (used for statistical test), N = number of embryos. **i**, Images from time-lapse video after photo-bleaching of Itgb1b-sfGFP in the primordium (left) and at the myotendinous junction (right). Fluorescence intensities are pseudo-colored as a heat map. Scale bars = 10 μm. **j**, Graph of Itgb1b-sfGFP fluorescence intensity over time before and after photo-bleaching in the primordium and at the myotendinous junction. The fluorescence intensities are normalized to the minimal intensities after photo-bleaching. Dots indicate mean intensities and error bars are SD. n = number of experiments, N = number of embryos. **k**, Plot of the percent recovery of Itgb1b-sfGFP fluorescence intensity at 27 sec after photo-bleaching in the primordium and at the myotendinous junction. n = number of experiments (used for statistical test), N = number of embryos. Data points, means, and SD are indicated. ****: p<0.0001 (two-tailed Welch's t-test). **l**, Experimental design to culture primordium cells. **m**, Antibody staining against Itgb1b-GFP and F-tractin-mCherry on cultured primordium cells. Arrowheads indicate actin stress fibers (**m'**) with Itgb1b-GFP clusters (arrows in **m''**) in the cell center and in protrusions (**m'''**). Scale bars = 20 μm (**m**-**m''**) and 1 μm (**m'''**). **n**, Antibody staining against Tln1-YPet and F-tractin-mCherry on cultured primordium cells. Arrowheads indicate actin stress fibers (**n'**) with Tln1-YPet clusters (arrows in **n''**) in the cell center and in protrusions (**n'''**). Scale bars = 20 μm (**n**-**n''**) and 1 μm (**n'''**). Images are max-projected z-stacks. Close-ups (right panels) are magnifications of the regions indicated by dotted squares in the middle panels.

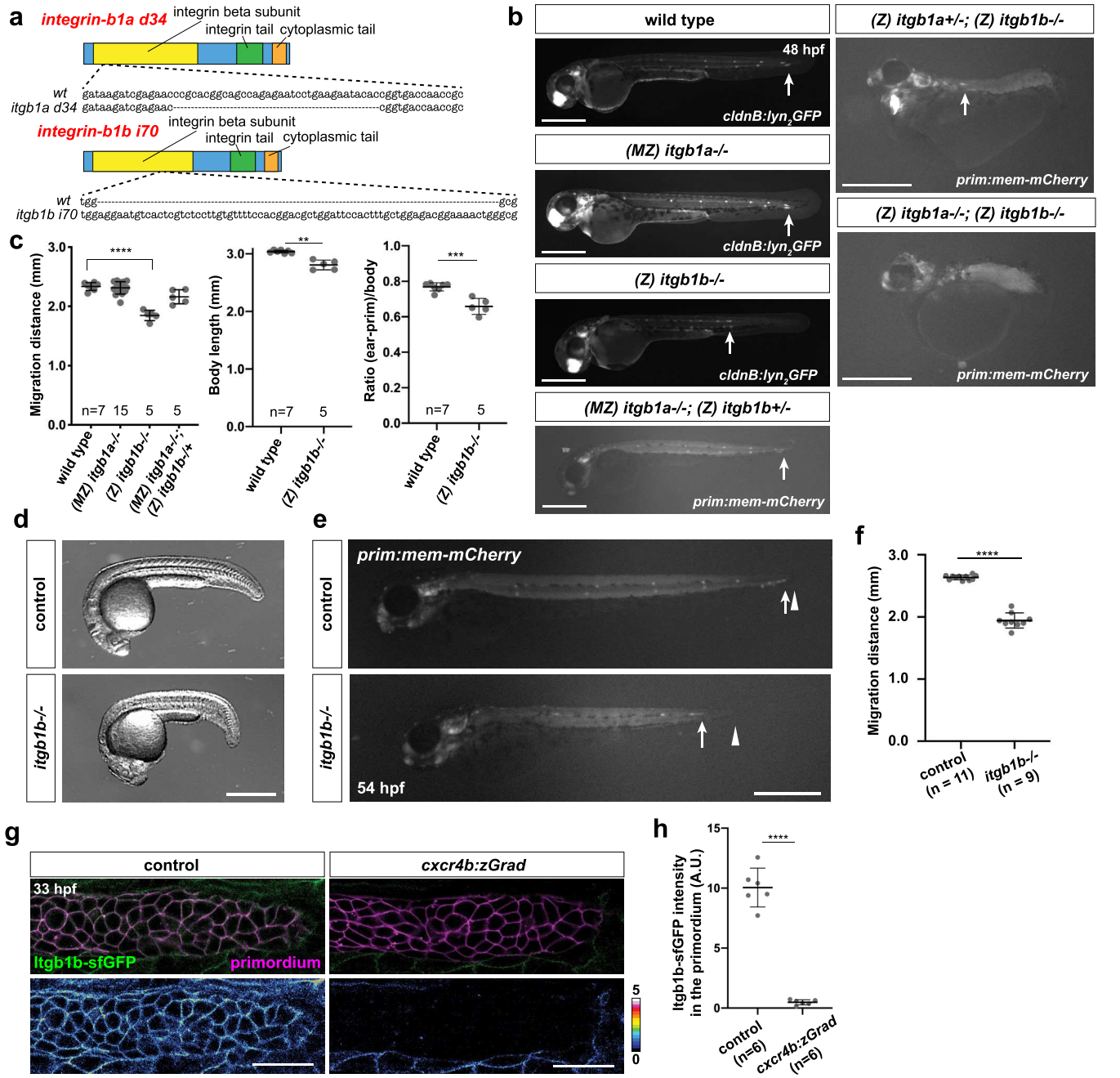

Extended Data Fig. 5 | *β1-integrin* mutational analysis. a, Schematic of the *itgb1a* and *itgb1b* alleles. d and i denote deletion and insertion, respectively. **b**, Primordium migration and morphology defects in embryos with different levels of *integrin-β1* activity at 48 hpf. M and Z denote maternal and zygotic mutants, respectively. Arrows indicate the position of the primordium. Scale bar = 0.5 mm. **c**, Quantification of the primordium migration distance (left), the body length (middle), and primordium migration distance normalized to body length (right) in 48 hpf *itgb1* mutant embryos. n = number of embryos. Data points, means, and SD are indicated. ****: p<0.0001 (one-way ANOVA followed by Tukey's multiple comparison test, left plot), **: p=0.0026 (two-tailed Welch's t-test, middle plot), and ***: p=0.0002 (two-tailed t-test, right plot). **d**, Overall morphology of control (wild-type or *itgb1b-/+*) and *itgb1b* mutant embryos at 24 hpf. Scale bar = 0.5 mm. **e**, Primordium migration in control (wild-type or *itgb1b-/+*) and *itgb1b* mutant embryos at 54 hpf. Scale bar = 0.5 mm. The arrows indicate the position of the primordium and the arrowheads indicate the position of the tip of the tail. **f**, Quantification of primordium migration in control (wild-type or *itgb1b-/+*) and *itgb1b* mutant embryos at 54 hpf. Data points, means, and SD are indicated. n = number of embryos. ****: p<0.0001 (two-tailed Welch's t-test). **g**, *prim:mem-mCherry*; *itgb1b:itgb1b-sfGFP* control (left) and *prim:mem-mCherry*; *itgb1b:itgb1b-sfGFP*; *cxcr4b:zGrad* 33 hpf embryos (right). Lower panels show the Itgb1b-sfGFP fluorescence as a heat map. Scale bar = 25 μm. Images are single confocal slices from a z-stack. **h**, Quantification of the Itgb1b-sfGFP fluorescence intensity in control and zGrad-expressing embryos at 33 hpf. Data points, means, and SD are indicated. ****: p<0.0001 (two-tailed Welch's t-test). n = number of embryos.

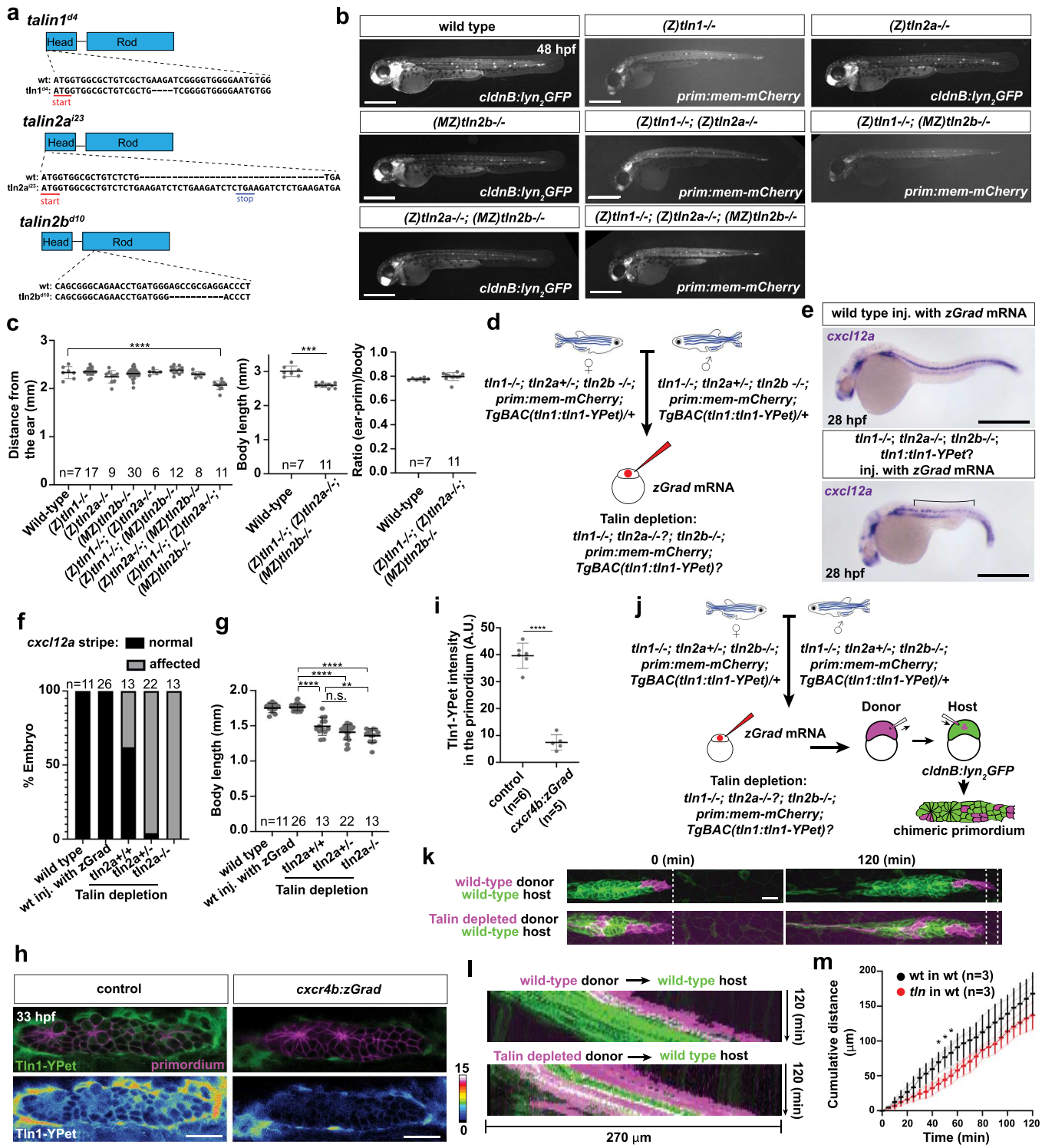

Extended Data Fig. 6 | See next page for caption.

Extended Data Fig. 6 | Generation and characterization of *talin* mutant and analysis of primordium migration in embryos or primordia with depleted Talin activity. a, Schematic of the *tln1*, *tln2a* and *tln2b* mutant alleles. The sequence around the deletions (d) and insertions (i) are shown. The start codons are indicated for $tln1^{d4}$ and $tln2a^{i23}$, and the premature stop codon for $tln2a^{i23}$. **b**, Primordium migration distance in 48 hpf embryos with different levels of *talin* activity. Scale bar = 0.5 mm. **c**, Quantification of the primordium migration distance (left), the body length (middle), and primordium migration distance normalized to body length (right) in *tln* mutants at 48 hpf. Data points, means, and SD are indicated. ****: p<0.0001 (one-way ANOVA with Tukey's multiple comparisons test, left plot), ***: p=0.0002 (two-tailed Welch's t-test, middle plot). n = number of embryos. **d**, Crosses to generate embryos with depleted Talin activity. **e**, *in situ* hybridization against *cxcl12a* mRNA on 28 hpf wild-type (top) and Talin-depleted (bottom) embryos injected with *zGrad* mRNA. Scale bar = 0.5 mm. **f**, Quantification of the percentage of control and Talin-depleted embryos with perturbed *cxcl12a* expression along the horizontal myoseptum in 28 hpf embryos. n = number of embryos. **g**, Quantification of the body length in control and Talin-depleted 28 hpf embryos. n = number of embryos. Data points, means, and SD are indicated. **: p=0.0063, ****: p<0.0001, n.s.:p=0.1610 (two-tailed Mann-Whitney test). **h**, *prim:mem-mCherry*; *tln1:tln1-YPet* control (left) and *prim:mem-mCherry*; *tln1:tln1-YPet*; *cxcr4b:zGrad* 33 hpf embryos (right). Lower panels show the Tln1-YPet fluorescence as a heat map. Scale bar = 25 μm. Images are single confocal slices from a z-stack. **i**, Quantification of the Tln1-YPet fluorescence intensity in control and zGrad-expressing embryos at 33 hpf. Data points, means, and SD are indicated. ****: p<0.0001 (two-tailed t-test). n = number of embryos. **j**, Experimental strategy to generate embryos with Talin-depleted clones in the primordium. **k**, Migration of wild-type primordia with clones of control cells (top) and Talin-depleted cells (bottom). Images are maximum-projected z-stacks from Supplementary Video 5. The dotted lines indicate the location of primordium tip. Scale bar = 20 μm. **l**, Kymographs of migrating chimeric primordia shown in (**k**) and Supplementary Video 5. **m**, Quantification of the cumulative migration distance of primordia with clones of control cells and Talin-depleted cells. Dots are means, error bars are SD. *: p=0.03131, p=0.03046 and p=0.04856 (45, 50 and 55 min in the graph) (two-tailed t-test). n = number of embryos.

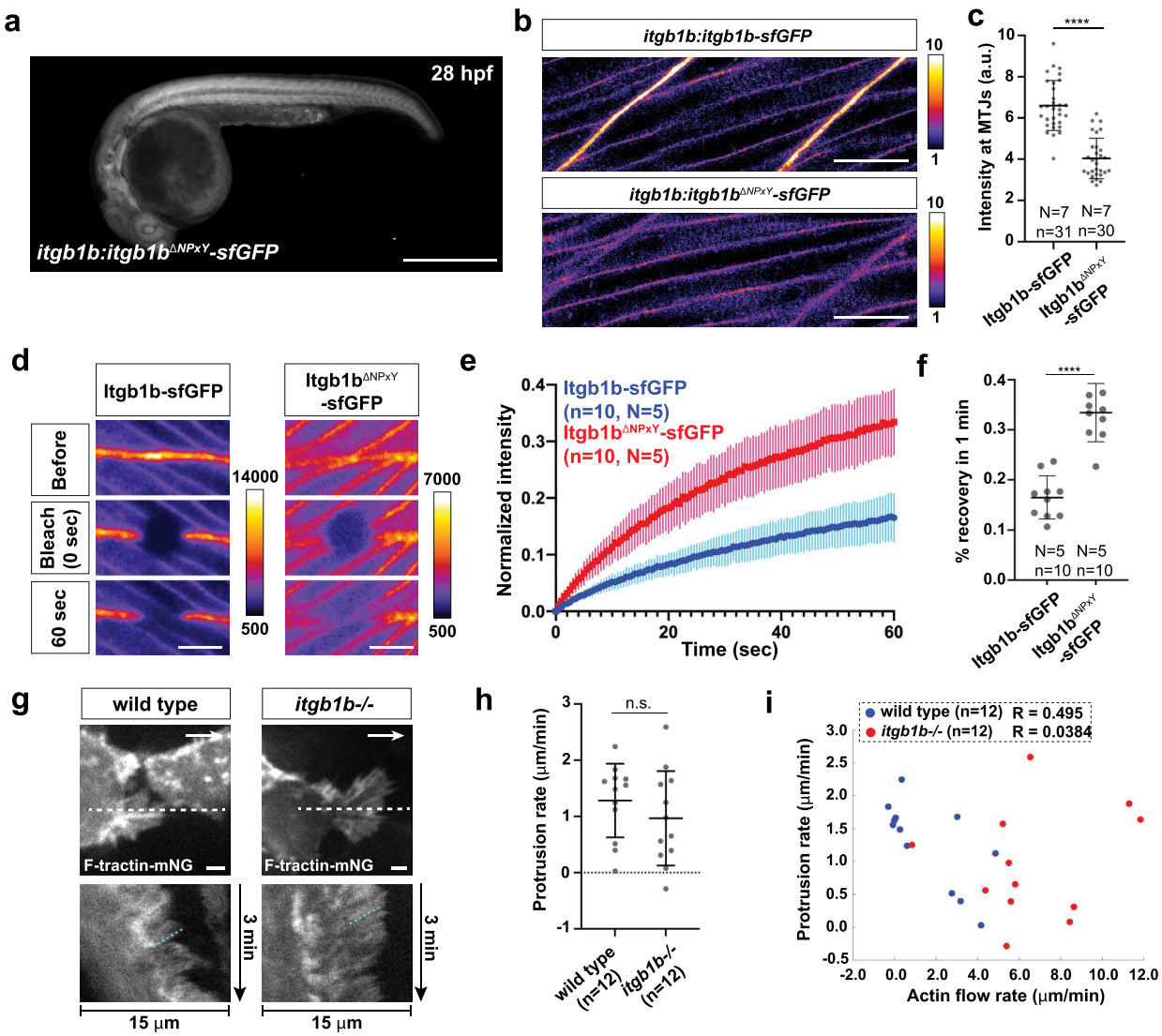

Extended Data Fig. 7 | Generation and characterization of *itgb1b:Itgb1b$^{\Delta NPxY}$-sfGFP* mutant knock-in line and F-actin retrograde flow analysis. **a**, Itgb1b$^{\Delta NPxY}$-sfGFP expression in a 28 hpf *itgb1b$^{\Delta NPxY}$-sfGFP* embryo. Image is sum-projected z-stacks. Scale bars = 0.5 mm. **b**, Distribution of Itgb1b-sfGFP and Itgb1b$^{\Delta NPxY}$-sfGFP in muscle of 33 hpf embryos. Images are single z-slices through muscle at the myotendinous junction imaged and scaled identically. The GFP intensity is pseudo-colored as a heat map. Scale bars = 20 μm. **c**, Quantification of the Itgb1b-sfGFP and Itgb1b$^{\Delta NPxY}$-sfGFP fluorescence intensities at the myotendinous junction (MTJ). Data points, means, and SD are indicated. ****: p<0.0001 (two-tailed Mann-Whitney test). n = number of experiments (used for statistical analysis), N = number of embryos. **d**, Images from time-lapse video after photo-bleaching of Itgb1b-sfGFP and Itgb1b$^{\Delta NPxY}$-sfGFP at the myotendinous junction. GFP intensities are pseudo-colored as heat maps. Scale bars = 10 μm. **e**, Graph of Itgb1b-sfGFP and Itgb1b$^{\Delta NPxY}$-sfGFP fluorescence intensities over time before and after photo-bleaching. The GFP fluorescence intensities are normalized to the minimal intensities after photo-bleaching. Dots indicate mean intensities and error bars are SD. n = number of experiments, N = number of embryos. **f**, Plot of the percent recovery of Itgb1b-sfGFP and Itgb1b$^{\Delta NPxY}$-sfGFP fluorescence intensities at 1 min after photo-bleaching shown in **e**. n = number of experiments (used for statistical analysis), N = number of embryos. Data points, means, and SD are indicated. ****: p<0.0001 (two-tailed t-test). **g**, Images of F-tractin-mNeonGreen localization at the apical sides of wild-type and *itgb1b-/-* primordium superficial cells (top). White arrows indicate the direction of migration. Scale bar = 2 μm. Images are single optical sections from Supplementary Video 6. Kymographs of Supplementary Video 6 along the dotted line indicated in top images (bottom). The dotted cyan line indicates the rate of actin flow. **h**, Protrusion rates in wild-type and *itgb1b* mutant primordium basal cells. Data points, means, and SD are indicated. n.s.: p=0.3167 (two-tailed t-test). n = number of cells. **i**, Plot of the protrusion rate versus the actin flow rate in individual primordium basal cells. n = number of cells.

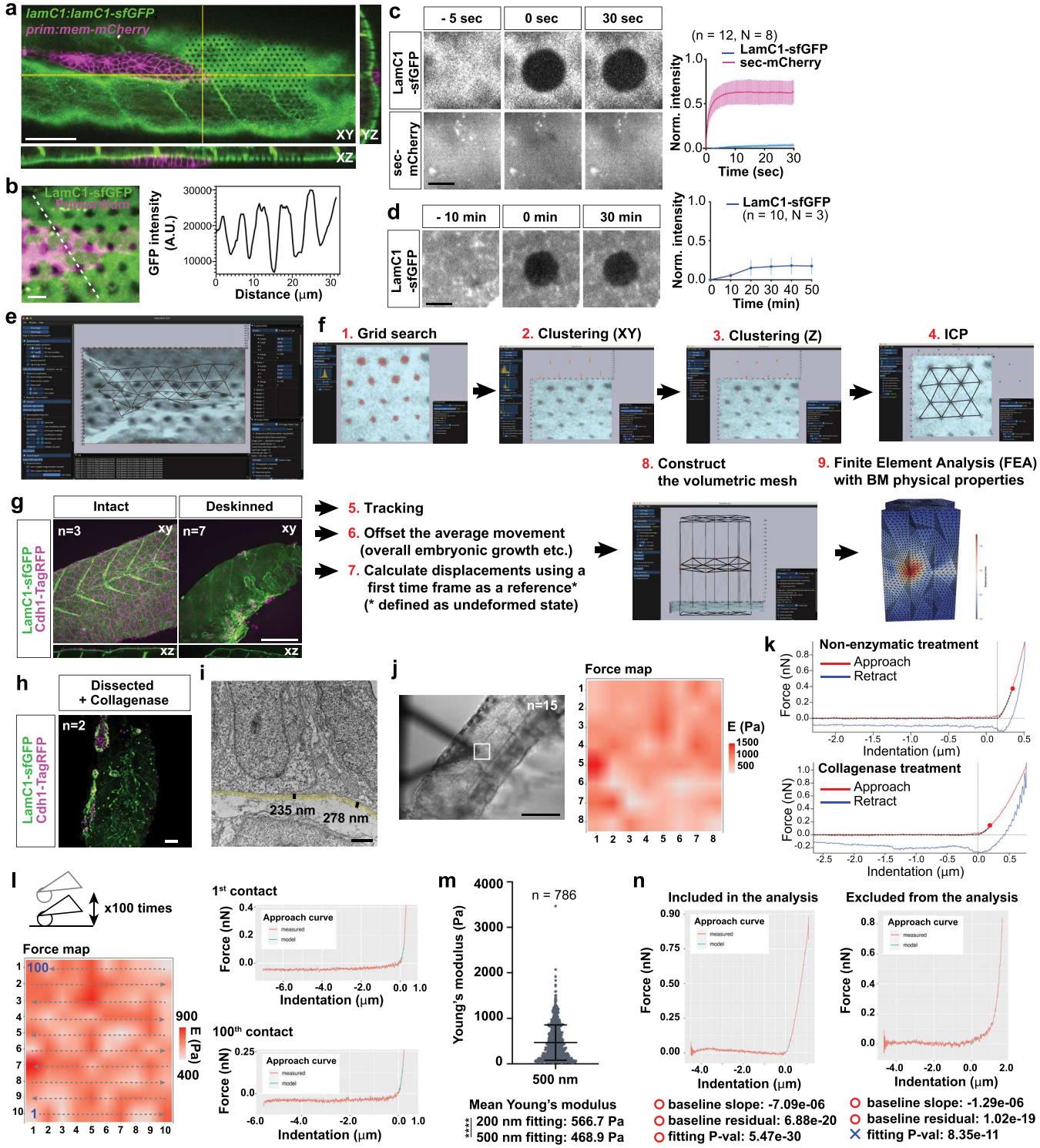

Extended Data Fig. 8 | See next page for caption.

Extended Data Fig. 8 | LamC1-sfGFP mobility, Embryogram workflow, and basement membrane stiffness measurements. a, Optical sections along the indicated planes of a z-stack of the primordium and the BM labeled with LamC1-sfGFP from Supplementary Video 7. LamC1-sfGFP was bleached in front of the primordium in a hexagonal pattern. Scale bar = 50 μm. **b**, Hexagonal bleach pattern on LamC1-sfGFP-labeled BM underneath the migrating primordium (left). Dotted line indicates location of intensity profile shown on right. Scale bar = 5 μm. The image is a maximum-projected z-stack. **c**, FRAP analysis of LamC1-sfGFP and extracellular mCherry in heat-shocked *hsp70l:sec-mCherry*; *lamC1:lamC1-sfGFP* embryos. Images from the time course are shown on the left and quantification of fluorescence recovery is shown on the right. Scale bar = 10 μm, error bars = SD, n = measurements from N embryos, dots = means, n was used for statistical analysis. **d**, Extended FRAP analysis of LamC1-sfGFP over 50 min in *lamC1:lamC1-sfGFP* embryos. Images from time course are shown on the left and quantification of fluorescence recovery is shown on the right. Scale bar = 10 μm, error bars = SD, dots = means, n = measurements from N embryos. n was used for statistical analysis. **e**, Image of Embryogram application user interface. **f**, In Embryogram, candidate locations for the bleached markers are identified by a grid search (1), clustered in the *XY*-plane (2), and then along the *Z*-axis (3). We match these candidates with a regular hexagonal grid using the iterative closest point algorithm (4). Markers are tracked in subsequent frames using optical flow and numerical optimization. The user can manually offset rigid body motions caused by the movement of the microscope, sample movement or sample growth (6). The displacement of each dot is calculated using the mesh for the first time frame as the relaxed reference (7). To perform finite element analysis (FEA), the user constructs a volumetric tetrahedral mesh above, below or both (8) and inputs the Young's modulus and the Poisson ratio of the material. The results of the FEA can be exported and visualized in other software packages such as ParaView (9). For detail see Supplementary Note 1. **g**, 28 hpf embryos with labeled skin and BM before and after surgical skin removal. Images are maximum-projected z-stacks. Scale bar = 100 μm. **h**, Deskinned and collagenase-treated *lamC1:lamC1-sfGFP*; *cdh1:cdh1-TagRFP* embryo. Image is a maximum-projected z-stack. Scale bar = 50 μm. **i**, TEM-image of the BM underneath the primordium. The semi-transparent yellow line traces the BM and the black lines indicate the thickness of the BM. Scale bar = 1 μm. **j**, Bright-field image of a deskinned embryo tail with the cantilever during an AFM measurement (left). A grid of 8×8 squares (20 μm by x 20 μm) on the BM was probed for its stiffness (square in left image) and the resultant stiffness map is shown on the right. Scale bar = 1 mm. **k**, Representative force curves showing the approach (red) and retraction (blue) curves for a deskinned embryo (top) and a collagenase-treated deskinned embryo (bottom). Cross-hairs indicate contact point position and force. Red dots on the approach curves indicate the first 200 nm from the contact point. The fit to the baseline and the Hertz model is indicated by a dotted black line. **l**, Analysis of the effect of repeated probing of the same area by AFM. The left image is a montage of the stiffness values obtained for the same location after measurements 1 to 100. The order of the measurements is indicated by the arrows. The force curves for the first and 100th measurements are shown on the right. The fit to the Hertz model is indicated in cyan. **m**, Quantification of the stiffness of the BM of deskinned embryos when fitting the first 500 nm after the contract point to the Hertz model. Data points, mean and SD are shown. Values for the fit of the first 200 nm to the Hertz model are shown for comparison. ****: $p<0.0001$ (two-tailed Mann-Whitney test). **n**, Representative force curves that meet (left) and do not meet (right) the indicated quality criteria.

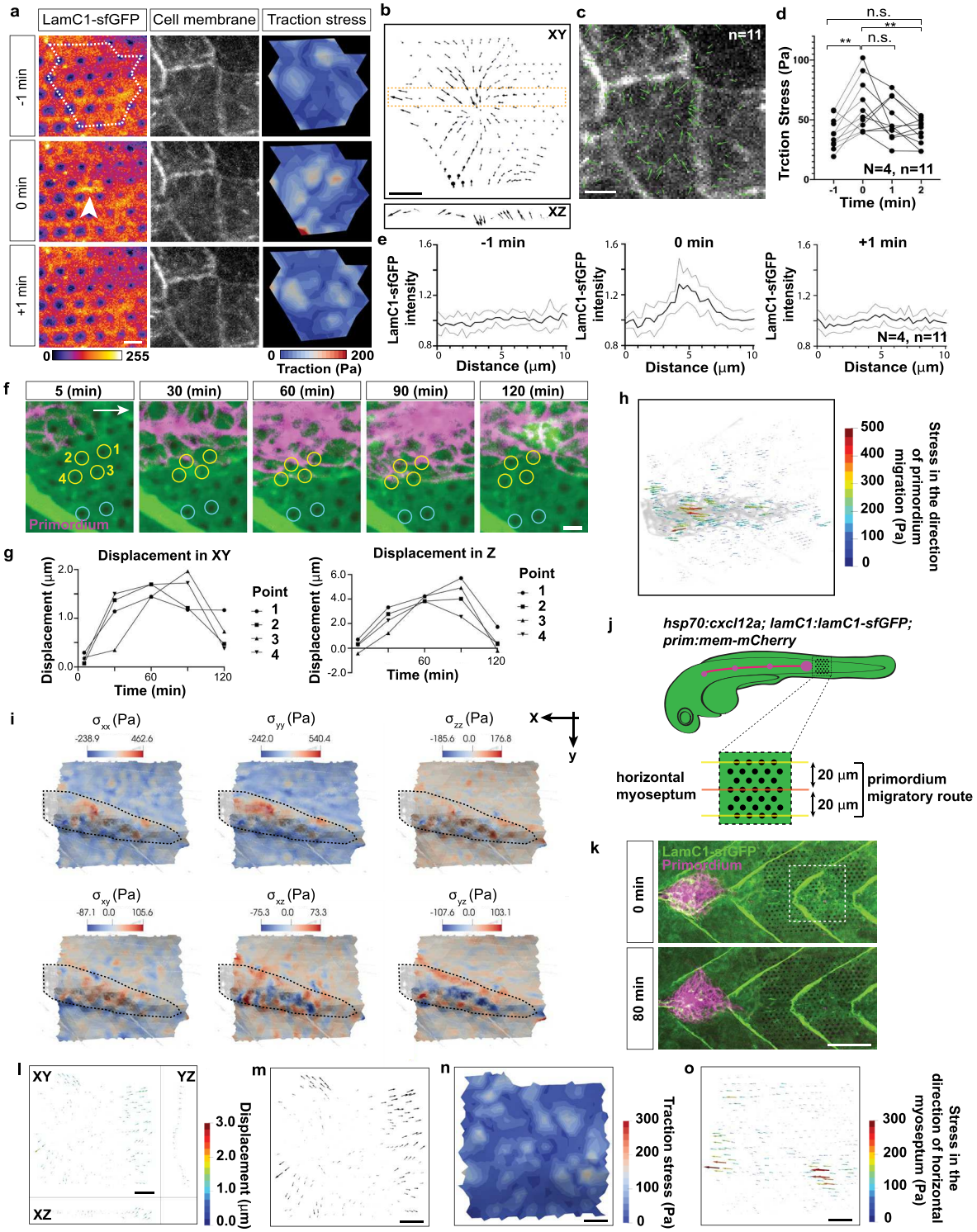

Extended Data Fig. 9 | See next page for caption.

Extended Data Fig. 9 | Distribution of stresses under the skin, under the primordium, and in the absence of the primordium. a, Images of LamC1-sfGFP (left) and basal skin cell membranes (middle) from Supplementary Video 9. The LamC1-sfGFP intensity is pseudo-colored as a heat map. The area outlined by a dotted line was analyzed using Embryogram to calculate the traction stresses (right) pseudo-colored as temperature map (right). The arrowhead indicates a spot of transient accumulation of LamC1-sfGFP. Images are maximum-projected z-stacks. Scale bar = 5 μm. **b**, Quiver plots of the BM displacement at 0 min in the XY- and XZ-planes. The XZ-plane quiver plot shows a subset of the vector field outlined by the orange rectangle. The magnitude of the vectors was increased by a factor of 3 for visualization purposes. Scale bar = 5 μm. **c**, Image of cell membrane at −1 min with arrows indicating the direction of movement from time point −1 min to 0 min as determined by PIV. Vector magnitudes are magnified three-times. Scale bar = 5 μm. **d**, Quantification of traction stresses. Traction stresses at the three vertices closest to a given wrinkle were averaged. Individual data points are shown. Individiual data points are indicated. **: p=0.0027 (−1 min vs. 0 min), p=0.0043 (0 min vs. 2 min) and n.s.: p=0.1479 (0 min vs. 1 min), p=0.7341 (−1 min vs. 2 min) (two-tailed paired t-test). n = number of measured cells, N = number of embryos, n was used for statistical analysis. **e**, Quantification of LamC1-sfGFP accumulation during BM wrinkling. Intensity profiles were obtained from a line plot across the BM wrinkle at 0 min indicated by the arrowhead in **a**, and from line plots at the same location of the images at the time points −1 min and 1 min. Intensities were normalized to the mean intensities at time point −1 min. Mean and SD are shown. n = number of measurements, N = number of embryos. **f**, Deformation of the BM before, during, and after primordium (magenta) migration. Images are from Supplementary Video 8. The white arrow indicates the direction of migration. Scale bar = 5 μm. **g**, Quantification of the displacement of bleached marks (yellow circles 1–4 in **f**) relative to control bleached marks (cyan circles in **f**). **h**, Quiver plot of the stresses in the direction of primordium migration. The magnitude of the stress vectors is color-coded. **i**, Distribution of the tensile and shear stresses around the migrating primordium outlined by a dotted line. The value of each unique component of the stress tensor is colored as a temperature map. The X and Y direction are indicated. The Z direction is orthogonal to the image plane. **j**, Experimental design of the stress analysis with blocked primordium migration. **k**, Images of a heat-shocked control embryo at 0 min and 80 min of Supplementary Video 8. The dotted line indicates the region used for the analysis. Images are maximum-projected z-stacks. Scale bar = 50 μm. **l**, Quiver plot of the displacement vectors shown along the Z, Y and X axes. The magnitude of the displacement vectors is color coded. Scale bar = 10 μm. **m**, Quiver plot of the displacement vectors projected in the XY-plane. The magnitude of the vectors was increased twofold. Scale bar = 10 μm. **n**, Distribution of the traction stress magnitudes color-coded using a temperature map. Scale bar = 10 μm. **o**, Quiver plot of the stresses in the direction of horizontal myoseptum. The magnitude of the stress vectors is color-coded. Scale bar = 10 μm. (**l**–**o**) Data correspond to the at the 80 min time point of Supplementary Video 10.

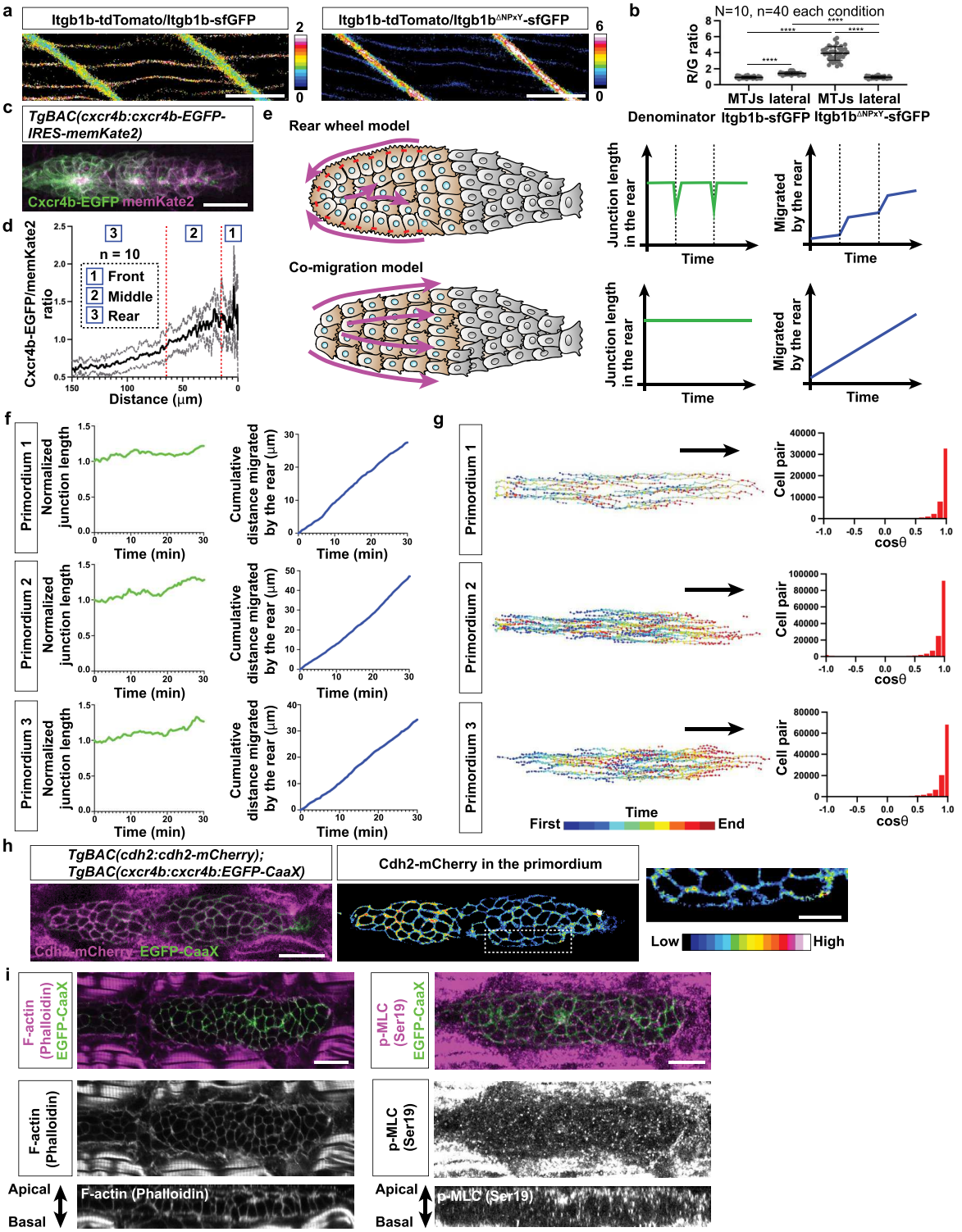

Extended Data Fig. 10 | See next page for caption.

Extended Data Fig. 10 | The primordium is a continuously migrating tissue. a, Itgb1b-tdTomato-to-Itgb1b-sfGFP (left) and Itgb1b-tdTomato-to-Itgb1b$^{\Delta NPxY}$-sfGFP (right) ratio images in trunk muscle cells. Images are single optical slices from z-stacks. Ratios are color-coded as indicated. Scale bar = 25 μm. **b**, Quantification of ratios Itgb1b-tdTomato to Itgb1b-sfGFP and Itgb1b-tdTomato to Itgb1b$^{\Delta NPxY}$-sfGFP at the myotendinous junction and lateral sides of muscle cells. Data points, means, and SD are indicated. ****: p<0.0001 (two-tailed Mann-Whitney test). n = number of measurements at indicated locations, N = number of embryos, n was used for statistical analysis. **c**, Image of Cxcr4b-EGFP and membrane-tethered Kate2 expressed from the Cxcl12a sensor in the primordium. Image is a maximum-projection of a z-stack. Scale bar = 25 μm. **d**, Quantification of the Cxcr4b-EGFP/Kate2 ratio across the primordium. Mean (black line) and SD (gray lines) are shown. n = number of embryos. **e**, Illustrations and predictions for two models of tissue migration. **f**, Quantification of junction length (left) and the cumulative migration distance over time for three primordia. **g**, Trajectories of individual primordium cells (left) and frequency plots for angles between any two given cell velocity vectors (right). **h**, Localization of Cadherin-2-mCherry and membrane-tethered EGFP in the primordium (left). Cdh2-mCherry fluorescence intensity pseudo-colored as a temperature map (middle) and on the primordium's rear at higher magnification (right). Images are single confocal slice from the z-stack. Scale bars = 25 μm (left) and 10 μm (right). **i**, Images of slices from a z-stack of 32 hpf *TgBAC(cxcr4b:EGFP-CaaX)* embryos stained for F-actin (left) or phospho-MLC (right) and GFP. Orthogonal views are shown.

nature research

Corresponding author(s): Daniele Panozzo and Holger Knaut

Last updated by author(s): Dec 19, 2021

Reporting Summary

Nature Research wishes to improve the reproducibility of the work that we publish. This form provides structure for consistency and transparency in reporting. For further information on Nature Research policies, see our Editorial Policies and the Editorial Policy Checklist.

Statistics

For all statistical analyses, confirm that the following items are present in the figure legend, table legend, main text, or Methods section.

n/a	Confirmed	
☐	☒	The exact sample size (*n*) for each experimental group/condition, given as a discrete number and unit of measurement
☐	☒	A statement on whether measurements were taken from distinct samples or whether the same sample was measured repeatedly
☐	☒	The statistical test(s) used AND whether they are one- or two-sided *Only common tests should be described solely by name; describe more complex techniques in the Methods section.*
☒	☐	A description of all covariates tested
☐	☒	A description of any assumptions or corrections, such as tests of normality and adjustment for multiple comparisons
☐	☒	A full description of the statistical parameters including central tendency (e.g. means) or other basic estimates (e.g. regression coefficient) AND variation (e.g. standard deviation) or associated estimates of uncertainty (e.g. confidence intervals)
☐	☒	For null hypothesis testing, the test statistic (e.g. *F*, *t*, *r*) with confidence intervals, effect sizes, degrees of freedom and *P* value noted *Give P values as exact values whenever suitable.*
☒	☐	For Bayesian analysis, information on the choice of priors and Markov chain Monte Carlo settings
☒	☐	For hierarchical and complex designs, identification of the appropriate level for tests and full reporting of outcomes
☒	☐	Estimates of effect sizes (e.g. Cohen's *d*, Pearson's *r*), indicating how they were calculated

Our web collection on statistics for biologists contains articles on many of the points above.

Software and code

Policy information about availability of computer code

Data collection	No software was used for data collection.
Data analysis	All images were analyzed using FIJI (Image J v1.0 and v2.0). Custom codes were written and included in this article. All statistical analyses were performed using GraphPad Prism 9. The atomic force microscopy measurements were analyzed with a custom written macro (attached on the manuscript) based on Rasylum version 0.4.0. (https://github.com/nstone8/Rasylum and https://rdrr.io/github/nstone8/Rasylum/) .Stresses were analyzed using the software embryogram which is included in the submission (https://zenodo.org/record/5762146#.Ya5X0y-B1QJ). The atomic force microscope was controlled using the Asylum Research software package Version IX (AR Software). Cell tracking was partly done using Imaris Version 8.0 (Bitplane, Oxford Instruments). Confocal image collection and tiled images were stitched using the LAS X Life Science Microscope Software (Leica). Stresses were visualized using ParaView (ParaView-5.8.1, Kitware). Polar diagrams were drawn using MATLAB (MathWorks). Spinning disk confocal microscopy images were collected using NIS-Elements (Nikon).

For manuscripts utilizing custom algorithms or software that are central to the research but not yet described in published literature, software must be made available to editors and reviewers. We strongly encourage code deposition in a community repository (e.g. GitHub). See the Nature Research guidelines for submitting code & software for further information.

Data

Policy information about availability of data

All manuscripts must include a data availability statement. This statement should provide the following information, where applicable:

- Accession codes, unique identifiers, or web links for publicly available datasets
- A list of figures that have associated raw data
- A description of any restrictions on data availability

The source data for Figs. 1–8 and Extended Data Figs. 1–10 are provided as separate excel files. The code for the software embryogram is deposited with Zenodo (https://zenodo.org/record/5762146#.Ya5X0y-B1QJ). The codes for image analysis are provided as a zip file. The Emsembl accession numbers for the genes modified in this study are:
Itgb1b: ENSDARG00000104484 (ZFIN;Acc:ZDB-GENE-030909-10)
Itgb1a: ENSDARG00000071863 (ZFIN;Acc:ZDB-GENE-060803-2)
Tln1: ENSDARG00000100729 (ZFIN;Acc:ZDB-GENE-031002-48)
Tln2a: ENSDARG00000017901 (ZFIN;Acc:ZDB-GENE-040724-263)
Tln2b: ENSDARG00000110973 (ZFIN;Acc:ZDB-GENE-130325-1)

All other data supporting the findings of this study are available from the corresponding authors on reasonable request.

Field-specific reporting

Please select the one below that is the best fit for your research. If you are not sure, read the appropriate sections before making your selection.

☒ Life sciences ☐ Behavioural & social sciences ☐ Ecological, evolutionary & environmental sciences

For a reference copy of the document with all sections, see nature.com/documents/nr-reporting-summary-flat.pdf

Life sciences study design

All studies must disclose on these points even when the disclosure is negative.

Sample size	No sample size calculation was performed. The sample size is chosen based on work of other groups using zebrafish embryos as a model system.
Data exclusions	No data were excluded from the analysis.
Replication	All attempts at replication were successful. Special cases are clearly stated in the manuscript.
Randomization	No randomization methods were used to allocate samples into experimental groups.
Blinding	Blinding is not relevant to this study. The experiments require the investigators to group the data between control and testing condition to quantify differences. However, embryos of different genotypes were imaged and grouped based on genotype after image collection for data analysis. Thus, at the time of data collection the genotype was unknown.

Reporting for specific materials, systems and methods

We require information from authors about some types of materials, experimental systems and methods used in many studies. Here, indicate whether each material, system or method listed is relevant to your study. If you are not sure if a list item applies to your research, read the appropriate section before selecting a response.

Materials & experimental systems

n/a	Involved in the study
☐	☒ Antibodies
☒	☐ Eukaryotic cell lines
☒	☐ Palaeontology and archaeology
☐	☒ Animals and other organisms
☒	☐ Human research participants
☒	☐ Clinical data
☒	☐ Dual use research of concern

Methods

n/a	Involved in the study
☒	☐ ChIP-seq
☒	☐ Flow cytometry
☒	☐ MRI-based neuroimaging

Antibodies

Antibodies used	rabbit anti-collagen IV (Abcam, Cambridge UK, cat no. ab6586) rabbit anti-Phospho-Myosin Light Chain 2 (Ser19) (Cell Signaling Technology, cat no. 3671, lot no. 6)

rabbit anti-Fibronectin (Sigma, cat no. F3648, lot no. 0000090857)
mouse anti-Chondroitin sulfate (Sigma, cat no. MA1-83055, lot no. WI3245117)
mouse anti-Paxillin (BD Transductions, cat no. 610051, lot no. 1110894)
rabbit anti-Paxillin(pTyr118) (Novusbio, cat no. NBP2-24459, lot no. 031327 42D(P))
rabbit anti-GFP primary antibody (Torrey Pines Biolabs, cat no. TP401, lot no. 081211)
goat anti-GFP (custom made antibody by Covance)
sheep anti-mCherry primary antibody (custom made antibody by Covance)
donkey anti-rabbit Cy3 (Jackson ImmunoResearch, cat no. 711-165-152, lot no. 102215)
goat anti-mouse Cy3 (1:500, Jackson ImmunoResearch, cat no. 115-165-003)
donkey anti-goat Alexa488 (Jackson ImmunoResearch, cat no. 705-546-147, lot no. 110667)
anti-DIG antibody coupled to alkaline phosphatase (Roche, cat no. 11093274910)
AlexaFluore594 Phalloidin (Invitrogen, cat no. A12381, lot no. 2335606)

Validation

Collagen IV: https://www.abcam.com/collagen-iv-antibody-ab6586.html and Maaike C.W. van den Berg et al., 2019, Cell Report
pMLC2(Ser19): https://www.cellsignal.com/products/primary-antibodies/phospho-myosin-light-chain-2-ser19-antibody/3671 and Sandra Ernst et al., 2012, Development, Jaydeep Sidhaye and Caren Norden, 2017, eLife
Fibronectin: https://www.sigmaaldrich.com/GB/en/product/sigma/f3648 and Jaydeep Sidhaye and Caren Norden, 2017, eLife
Chondroitin sulfate: https://www.thermofisher.com/antibody/product/Chondroitin-Sulfate-Antibody-clone-CS-56-Monoclonal/MA1-83055
Same clone from the different manufacture was used in Jaydeep Sidhaye and Caren Norden, 2017, eLife
Paxillin: https://www.bdbiosciences.com/en-us/products/reagents/microscopy-imaging-reagents/immunofluorescence-reagents/purified-mouse-anti-paxillin.610051
Sofia Hirth et al., 2016, PlosOne
pPaxillin(pTyr118): https://www.novusbio.com/products/paxillin-antibody_nbp2-24459
Hannah M. Olson and Alex V. Nechiporuk, 2021, Developmental Biology
GFP (Torrey Pines Biolab): https://www.labome.com/product/Torrey-Pines-Biolabs/TP401.html
GFP (Covance): Gayatri Venkiteswaran et al., 2013, Cell (https://doi.org/10.1016/j.cell.2013.09.046)
mCherry (Covance): John Wang et al., 2018, Developmental Cell (https://doi.org/10.1016/j.devcel.2018.07.015)
anti-rabbit Cy3: https://www.jacksonimmuno.com/catalog/products/711-165-152
anti-mouse Cy3: https://www.jacksonimmuno.com/catalog/products/115-165-003
anti-goat Alexa488: https://www.jacksonimmuno.com/catalog/products/705-546-147
anti-DIG antibody coupled to alkaline phosphatase: https://www.sigmaaldrich.com/GB/en/product/roche/11093274910
AlexaFluore594 Phalloidin: https://www.thermofisher.com/order/catalog/product/A12381

Animals and other organisms

Policy information about studies involving animals; ARRIVE guidelines recommended for reporting animal research

Laboratory animals: zebrafish

Wild animals: *Provide details on animals observed in or captured in the field; report species, sex and age where possible. Describe how animals were caught and transported and what happened to captive animals after the study (if killed, explain why and describe method; if released, say where and when) OR state that the study did not involve wild animals.*

Field-collected samples: *For laboratory work with field-collected samples, describe all relevant parameters such as housing, maintenance, temperature, photoperiod and end-of-experiment protocol OR state that the study did not involve samples collected from the field.*

Ethics oversight: This study was performed in strict accordance with the recommendations in the Guide for the Care and Use of Laboratory Animals of the National Institutes of Health. All of the animals were handled according to approved institutional animal care and use committee (IACUC) protocols (IA16-00788_AMEND202100320) of the NYU School of Medicine.

Note that full information on the approval of the study protocol must also be provided in the manuscript.